

Diplomarbeit

Data-error quantification in time-domain induced polarization imaging based on the analysis of the decay curve

ausgeführt am

Department für Geodäsie und Geoinformation
Forschungsgruppe Geophysik
der Technischen Universität Wien

unter der Anleitung von

Dr. Adrian Flores-Orozco

durch

Jakob Gallistl, BSc
Laaher Straße 17
4052 Ansfelden

Wien, 12.01. 2017

Unterschrift Verfasser

Abstract

Recent studies have demonstrated the advantages of a careful processing of induced polarization (IP) imaging data sets. In particular, inversion results based on a detailed quantification of data-error have shown the possibility to solve for electrical images with enhanced contrasts and a reliable correlation with subsurface structures and processes, as required for quantitative applications of IP imaging. The analysis of the discrepancy between normal and reciprocal measurements has been established as a suitable method to assess data quality in electrical imaging and the parametrization of error models. However, for exploration surveys at extensive areas or monitoring applications, the requirement of reduced acquisition times hinder the collection of reciprocal measurements. Therefore, this thesis presents an alternative methodology to quantify data error in time-domain IP (TDIP) imaging measurements based on the analysis of the recorded IP decay curve. The "Decay Curve Analysis" (DCA) described here does not require the collection of reciprocal measurements, yet provides information about data-error required for the identification of outliers, as well as the quantification of error parameters for the inversion of TDIP imaging datasets. Comparison of the error parameters and imaging results following the DCA analysis and conventional normal-reciprocal analysis revealed consistent results, demonstrating the accuracy of the approach.

Kurzfassung

Kürzlich erschienene Studien betonen die gewissenhafte Prozessierung von Daten der Induzierten Polarisation (IP) Bildgebungsmethode. Insbesondere Bildgebungsergebnisse, die auf einer detaillierten Beschreibung des Datenfehlers basieren, zeigen einen stärkeren Kontrast in den elektrischen Eigenschaften und erlauben eine verlässliche Korrelation mit den Strukturen im Untergrund. Eine weit verbreitete Methode zur Beschreibung von systematischen und zufälligen Datenfehlern ist die Analyse der Abweichung zwischen Messungen, die in Normal- und Reziprokkonfiguration gemessen wurden. Für große Messkampagnen (eine große Anzahl an Messprofilen), sowie Monitoringanwendungen ist die Methode jedoch nur eingeschränkt anzuwenden, da die Messungen in Reziprokkonfiguration einen zusätzlich Zeitaufwand bedeuten, der nicht immer vertretbar ist. Diese Masterarbeit beschreibt daher eine neue Datenprozessierungsmethode, die auf einer Analyse, der im Zeitbereich gemessenen Abklingkurve des Spannungssignals basiert und keine zusätzliche Messung in Reziprokkonfiguration voraussetzt. Die Methode erlaubt eine zuverlässige Identifikation von systematischen Messfehlern und die Beschreibung von zufälligen Datenfehlern. Ein Vergleich von Bildgebungsergebnissen, auf Basis der Normal-Reziprok und der hier vorgestellten Methode, zeigt konsistente Ergebnisse und demonstriert die Anwendbarkeit und Genauigkeit der hier präsentierten Methode.

Contents

Table of Contents	i
List of Tables	iii
List of Figures	v
1 Introduction	1
2 Theory	3
2.1 Time-Domain-Induced-Polarization	3
2.2 Frequency-Domain-Induced-Polarization	5
2.3 Electrode configuration	6
2.4 Inversion	8
2.4.1 Complex resistivity inversion	8
2.4.2 Parameterization of resistance error	9
2.4.3 Parameterization of phase error	9
2.5 Site description and TDIP survey	10
2.6 Pseudosections	11
2.7 Normal-reciprocal approach	14
3 Fitting and Sampling of the Decay Curve	17
3.1 Evaluation of the sampling of the voltage decay on the derivation of the decay curve	17
3.2 Evaluation of appropriate fitting models	23
3.3 Fitting of the time-domain Cole-Cole model	30
3.4 Evaluation of the sampling on the model fitting	33
4 Histogram Analysis	39
5 Analysis of the Spatial Consistency	45
5.1 Computation of reference curves	47
5.2 Partitioning of data sets	49
5.3 Analysis of the spatial consistency - the reference curve approach	56

Contents

5.4	Characterization of outliers	58
5.4.1	Single reference curve	59
5.4.2	Current dipole partitioning	60
5.4.3	Depth level partitioning	60
5.4.4	Uniform partitioning	61
5.4.5	Focused partitioning	63
5.4.6	Other parameters	63
5.4.6.1	Goodness of fit	63
5.4.6.2	Deviation between model curves fitted to all gates and gates with even/uneven numbers – 3-model deviations	64
5.5	Definition of parameter thresholds	65
5.5.1	Stepwise selection of threshold values	65
5.5.2	Thresholds defined by a histogram analysis of k	68
5.5.3	Fixed thresholds with additional conditions	68
6	Error Modelling	71
6.1	Finding parameters describing the random error	71
6.2	Consistency between Δm_i of MG and DD data sets	77
6.3	Determination of error parameters and the application in an inversion scheme	78
7	Decay Curve Analysis	85
7.1	Power law fit and first filter	85
7.2	Computation of the reference curve and second filter	86
7.3	Standard deviation estimate and bin analysis	87
7.4	Error model for resistance measurements	87
7.5	Results	87
8	Discussion & Conclusion	91
	Bibliography	95

List of Tables

2.1	Gaussian noise characteristics for the simulation of random error	12
3.1	Gaussian noise characteristics for the voltage decay	18
3.2	Gate widths, number and distribution for the sampling of the voltage signal - 1 .	18
3.3	Selected models for further fitting test	25
3.4	Goodness of fit values for the Cole-Cole and <i>pow2</i> model	33
3.5	Gate widths, number and distribution for the sampling of the voltage signal - 2 .	34
4.1	Rules for the calculation of n_b	43
5.1	Evaluation of the smoothness of reference curves	49
5.2	Boundary definition for the uniform partitioning	51
5.3	Boundary definition for the focused partitioning (i)	52
5.4	Boundary definition for the focused partitioning (ii)	52
5.5	Exemplary subsets for the current dipole partitioning	54
5.6	Adjustment rules for the standard deviations of k_u and k_d	70

List of Figures

2.1	Principles of Time-Domain-Induced-Polarization	4
2.2	Sampling of the voltage decay for the construction of the decay curve	4
2.3	Principles of Frequency-Domain-Induced-Polarization	6
2.4	Illustration of the Dipole-dipole and Multiple-gradient electrode configuration	7
2.5	Schematic cross section of the lithology at the Shiprock Site	10
2.6	Map of the Shiprock Site and location of the TDIP profiles	11
2.7	Pseudosections of forward modelled electrical properties	13
2.8	Three layer models used for the forward modelling	13
2.9	Distribution of the resistance misfit	15
3.1	Sampling of the voltage decay - numerical example	19
3.2	Measured voltage decay for 2s pulse length	21
3.3	Sampling of the voltage decay - field data example	22
3.4	Comparison of fitting results for models of the exponential and power law family	25
3.5	Evaluation of fitting models 1	27
3.6	Evaluation of fitting models 2	28
3.7	Evaluation of fitting models 3	29
3.8	Comparison of fitting results for the Cole-Cole and the <i>pow2</i> model	32
3.9	The effects of the sampling type on the model fitting	35
3.10	Distribution of ΔM_{int} and RMSD against M_{int}	37
4.1	Example of threshold based filtering and it's challenges	40
4.2	Illustration of continuous histogram/histogram with gaps	41
4.3	Block chart of the histogram analysis	42
4.4	Filter results for different parameterizations of the number of bins for in the histogram analysis	44
5.1	Illustration of spatial consistency before and after filtering	45
5.2	Computation of reference curves - different realizations	48
5.3	Importance of choosing the right number of reference curves	50
5.4	Transfer from bin minima to chargeability values	52
5.5	Data partitioning based on the integral chargeability	53
5.6	Data partitioning based on the common current dipole	54

List of Figures

5.7	Illustration of clustering of measurements of the same depth level	55
5.8	Data partitioning based on the depth level of the pseudosection	56
5.9	Illustration of the reference curve approach	57
5.10	Characterization of outliers - 1	59
5.11	Characterization of outliers - 2	61
5.12	Characterization of outliers - 3	62
5.13	Characterization of outliers - 4	64
5.14	Filtered pseudosections obtained with stepwise selection of thresholds - MG . . .	66
5.15	Filtered pseudosections obtained with stepwise selection of thresholds - DD . . .	67
5.16	Raw pseudosection and filter results obtained with the NRA	67
5.17	Filtered pseudosections for different multiplication factors of the standard deviation	69
6.1	Normal-reciprocal misfit for chargeability measurements	72
6.2	k vs. the NRA misfit both as a function of R	74
6.3	Δm_i vs. the NRA misfit both as a function of $R - 1$	74
6.4	Δm_i vs. the NRA misfit both as a function of $R - 1$	76
6.5	Δm_i combined for all gates vs. the NRA misfit both as a function of $R - 1$. . .	76
6.6	Consistency of Δm_i for a MG and DD data sets	78
6.7	Comparison adjusted error models NRA - DCA	79
6.8	IP imaging results for different error parameterizations	81
6.9	DCA error model adjusted to NRA model	81
6.10	IP imaging results for MG and DD data set of the same profile	82
6.11	Comparison of Δm_i plotted against R and ΔR against $1/R$	83
6.12	Resistivity imaging results based on different resistance error parameterizations .	83
7.1	MG pseudosection after first filter	86
7.2	MG pseudosection after second filter	87
7.3	DD pseudosection after removal of outliers following the DCA and NRA	88
7.4	Imaging results as obtained for the DCA and NRA	89

Chapter 1

Introduction

Initially developed for the prospection of metallic ores (Pelton et al., 1978), the induced polarization (IP) method has emerged in recent years as a suitable technique for environmental and hydrogeological studies. As an extension of the standard DC-resistivity method, IP measurements provide information about the electrical resistivity (i.e. energy loss) and polarization (i.e. energy storage) properties of the subsurface, permitting an improved lithological characterization (Kemna et al., 2012). An increasing number of studies report the meaningful application of the IP method, such as the assessment of permafrost degradation (Doetsch et al., 2015b), the evaluation of processes associated with CO₂ injections in shallow aquifers (Dafflon et al., 2012; Doetsch et al., 2015a), the monitoring of zero-valent nano-particles injections (Flores Orozco et al., 2015), the mapping and delineation of landfills and contaminants (Sogade et al., 2006; Ustra et al., 2012; Flores Orozco et al., 2012a; Gazoty et al., 2012a; Gazoty et al., 2012b) and the monitoring of bioremediation processes (Flores Orozco et al., 2011; Flores Orozco et al., 2013). The IP method has also been used for slope instability studies (Marescot et al., 2008) and the characterization of cracks in clay-rocks (Okay et al., 2013) and a recent study further proposed the application of the IP method for the detection of coal seam fires (Shao et al., 2017). Furthermore, changes in the electrical signatures have been correlated to reversible chemical transformation of bio-minerals (Slater et al., 2007; Flores Orozco et al., 2013) and a recent study explored the applicability of the IP imaging method for the prospection of naturally reduced zones (NRZ) at the floodplain scale (Wainwright et al., 2015). As pointed out by (Wainwright et al., 2015) the modest polarization response associated to NRZ places high demands on the resolution of the IP imaging results.

An adequate characterization of the data error is critical to enhance the resolution of electrical images, considering that an underestimation of data error is typically associated to the creation of artifacts in the images, whereas data-error overestimation generally leads to the loss of resolution (LaBrecque et al., 1996). Furthermore, during the processing of the data, quantitative information on the characteristics of data error is required to i) assess the reliability of the data, ii) identify and remove outliers associated with systematic errors, and iii) adjust error

models describing the characteristics of inherent random errors. Additionally, the characterization of large areas by means of IP imaging demands an on-site evaluation of data quality in order to: (1) eventually indicate the need to increase the signal-to-noise ratio (SNR), e.g. by modifying the measuring protocol and (2) determine areas of interest for the collection of denser datasets (e.g. higher resolution). Furthermore, particularly for extensive data sets automatic processing schemes are needed which fulfill the mentioned requirements. To date, a widely accepted method to evaluate IP data quality is based on the analysis of the misfit between normal and reciprocal measurements, where reciprocal measurements refer to the recollection of the data with interchanged current and potential electrodes (LaBrecque et al., 1996; Slater et al., 2000; Slater and Binley, 2006; Flores Orozco et al., 2011; Flores Orozco et al., 2012b). Nevertheless, the necessity to reduce the acquisition time for large-scale surveys compromises the collection of reciprocals. Furthermore, measuring configurations characterized by high SNR, such as the multiple-gradient array (Dahlin and Zhou, 2006), are not suited for the collection of reciprocals with multi-channel instruments without severely increasing the acquisition time. Accordingly, IP surveys at the large scale urge for the development of new techniques to quickly and reliably quantify data error without the need of reciprocal readings.

This Master's thesis investigates the possibility to characterize the data error in time-domain IP measurements based on an analysis of the voltage decay curve and aims at the development of a novel data processing methodology providing both an adequate identification of outliers and the quantification of the random error. As the numerical modelling of typical noise characteristics is practically impossible due to its complexity and the various possible sources (Flores Orozco et al., 2012b), the conducted analysis are based on field data sets collected for the delineation of NRZ and characterized by a modest polarization response. In order to evaluate the obtained results, a comparison with the results following the normal-reciprocal methodology is performed.

The first chapter provides a short introduction to the IP imaging method, the description of the field data and the normal-reciprocal methodology. In the second chapter the effects of random noise on the sampling of voltage decay and the fitting of different model curves are investigated. The third and fourth chapter describe approaches to identify systematic errors in TDIP data based on i) an analysis of the spatial consistency of measurements and ii) an analysis of the distribution of measurements in a histogram. Chapter five investigates the possibility to quantify the random error of measurements. The main finding of this thesis - a novel data processing methodology called "Decay Curve Analysis" (DCA) is presented in chapter six, followed by discussion and conclusion.

Chapter 2

Theory

2.1 Time-Domain-Induced-Polarization

The Induced-Polarization (IP) method is based on measurements with a set of four electrodes, whereas two electrodes act as a current sink (subsequently referred to as the current dipole) and two electrodes are used for the measurement of the potential difference, i.e. the voltage (subsequently referred to as the potential dipole). The basic principle is illustrated in figure 2.1. The dashed line denotes the current signal whereas the solid line denotes the measured voltage signal. Typically a switched square wave is used for current injection in order to compensate for possible drifts in the self potential V_{sp} (see figure 2.1). The length of the current injection is commonly referred to as pulse length and varies for modern instruments between hundreds of milliseconds (ms) to several seconds (s). After the start of current injection and a short charge-up phase the voltage measurement should reach a stable level, here denoted to as the primary voltage V_p . V_p is utilized for the computation of the apparent resistivity ρ_a (in equation 2.1), using the fundamental Ohm's law and a geometrical factor k which takes into account the position of the current and potential electrodes along the profile respectively the electrode array.

$$\rho_a = Rk \quad \text{with} \quad R = \frac{V_p}{I} \quad R \dots \text{transfer resistance} \quad I \dots \text{injected current} \quad (2.1)$$

Similarly to the charge-up phase during current injection, does the voltage signal after current shut-off not directly resume to zero but follows a smooth decay. The shape of the decay is defined by both data acquisition parameters such as the pulse length, but more important, by a variety of parameters controlling different polarization mechanisms (Ward, 1990) therefore representing the main target of TDIP measurements as it provides the information about the polarizability respectively chargeability of the subsurface. Note here, that the actual voltage decay not only contains the information on the magnitude but also on time dependent parameters of the polarization effect (Ward, 1990; Kemna, 2000) therefore representing a superior parametrization over magnitude-only formulations. The voltage decay is typically being sampled using a discrete

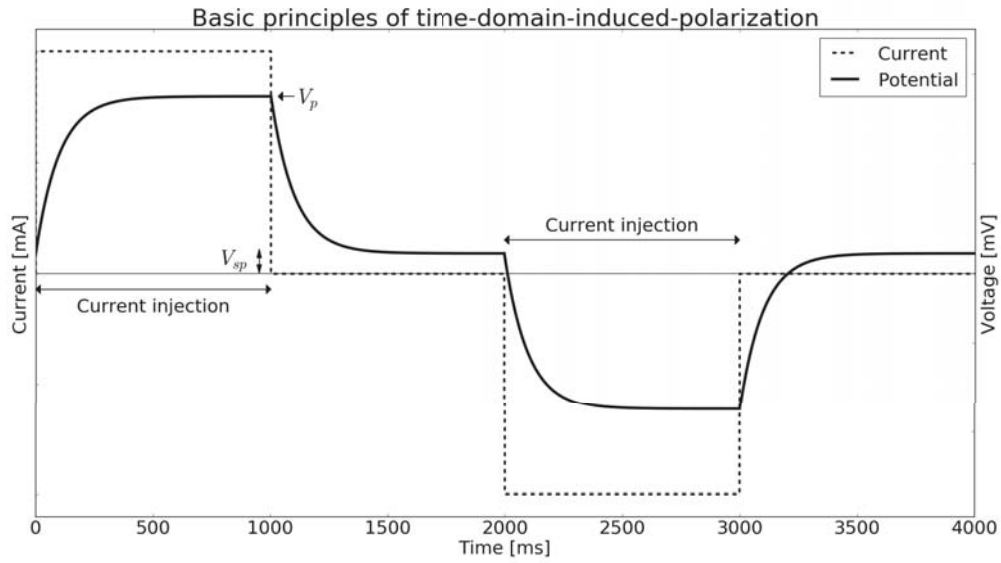


Figure 2.1: Signals and measurement principle of time-domain-induced-polarization.

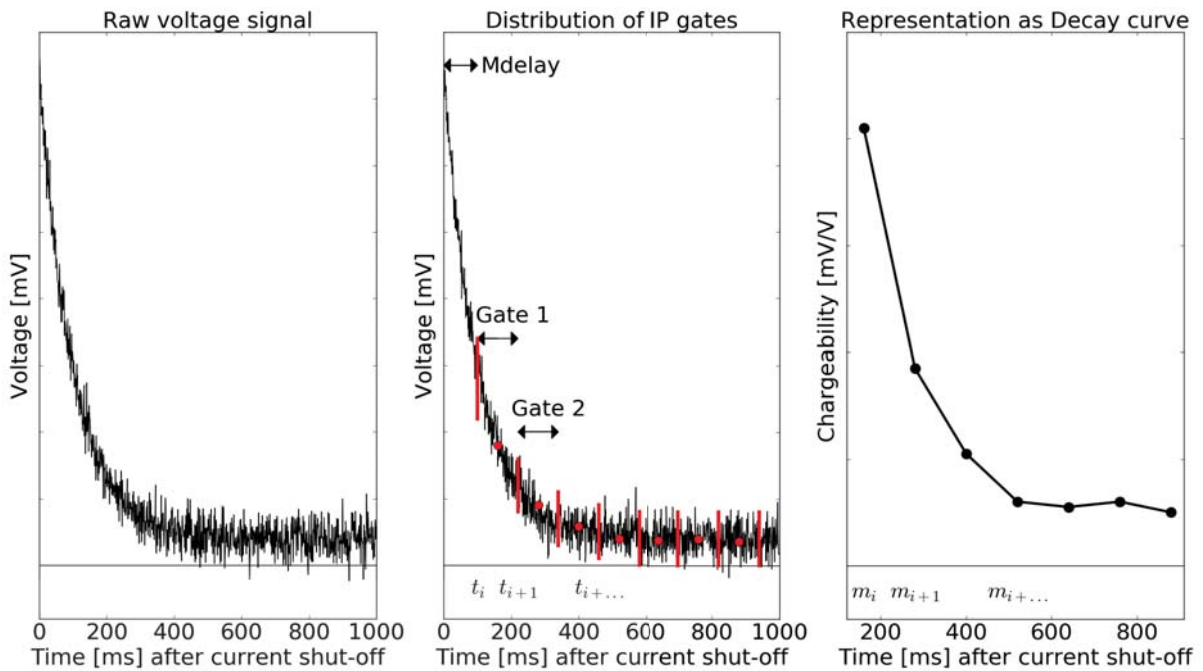


Figure 2.2: The raw voltage signal is being integrated in different time gates for the construction of the decay curve. The integrated and normalized values in each gate are the partial chargeability values.

number of gates or IP windows depending on the capability of the instrument (see figure 2.2). In every gate the voltage signal V_{ip} is integrated over a specified open t_i and close time t_{i+1} in ms which typically can be freely chosen. The integrated value is subsequently normalized by

the primary voltage (see equation 2.2).

$$m_i = \frac{1}{V_p (t_{i+1} - t_i)} \int_{t_i}^{t_{i+1}} V_{ip} dt \quad (2.2)$$

Values computed using equation 2.2 are typically referred to as apparent partial chargeability m_i in [mV/V] whereas i is the individual gate number. The early times of the voltage decay can be affected by a sum of phenomenons generalized as electro-magnetic coupling. In order to avoid a sampling of voltage signals with uncertain origin, the first gate commonly starts after a delay of a few milliseconds after current shut-off. This delay is referred to as *Mdelay*. Assuming 20 gates resulting in 20 apparent partial chargeability values an alternative representation of the voltage decay can be provided referred in this thesis to as the so-called *decay curve*. The decay curve is the standard representation of the IP signal in TDIP and consists of plotting the partial chargeability of every gate to the gate's midpoint (see figure 2.2). The sampling of the voltage decay, i.e. the number, distribution and width of the individual gates needs to be chosen on the requirements of the survey as well as the expected noise level. Commonly used are samplings consisting of equally sized gates or gates with increasing width over time. A standard sampling of the Syscal Pro equipment (by IRIS Instruments) for a 2 s pulse length is composed of 20 gates, each with 80 ms duration, starting after an initial Mdelay of 240 ms.

Another parametrization of the IP signal in TDIP is the so-called *integral chargeability* M_{int} , which can be computed based on equation 2.3 and represents an average value of the partial chargeability values with the individual gate lengths acting as a weighting factor.

$$M_{int} = \sum_{i=1}^N m_i (t_{i+1} - t_i) / \sum_{i=1}^N (t_{i+1} - t_i) \quad N \dots \text{number of gates} \quad (2.3)$$

The integral chargeability however, does not explain the shape of the decay curve and can therefore be only seen as a very robust representation of the magnitude of the polarization effect (due to the averaging of the partial chargeability values).

2.2 Frequency-Domain-Induced-Polarization

Analogous to TDIP measurements the minimal measurement configuration consists of a set of four electrodes with the same differentiation between the current and potential dipole. For frequency-domain-induced-polarization (FDIP) measurements an alternating current, realized as a harmonic sine wave with a specified frequency f (typically ranging from 0.01 Hz up to a few kHz) is injected. At the potential dipole the voltage signal is being recorded. The measurement principle is illustrated in figure 2.3. The FDIP method is based on the measurement of the transfer impedance $Z = \ln R + i\varphi$ comprised of the amplitude ratio R and the phase-shift

(also referred to as phase) φ between the peak current I and peak voltage V . φ represents the measurement of the IP effect and in contrast to measurements in the time domain, φ is collected during current injection. The collection of frequency domain data at different frequencies can provide additional information about a possible frequency dependence of the IP effect. Such measurements are referred to as spectral-induced-polarization (SIP) measurements. For a more detailed review on the method please refer to Sumner (1976), Ward (1990) and Telford et al. (1990).

Assuming a constant-phase response, time domain chargeability values can be linearly converted to frequency domain phase-shift values (at the fundamental frequency of 0.125 Hz). For a detailed description of the approach please refer to Kemna (2000).

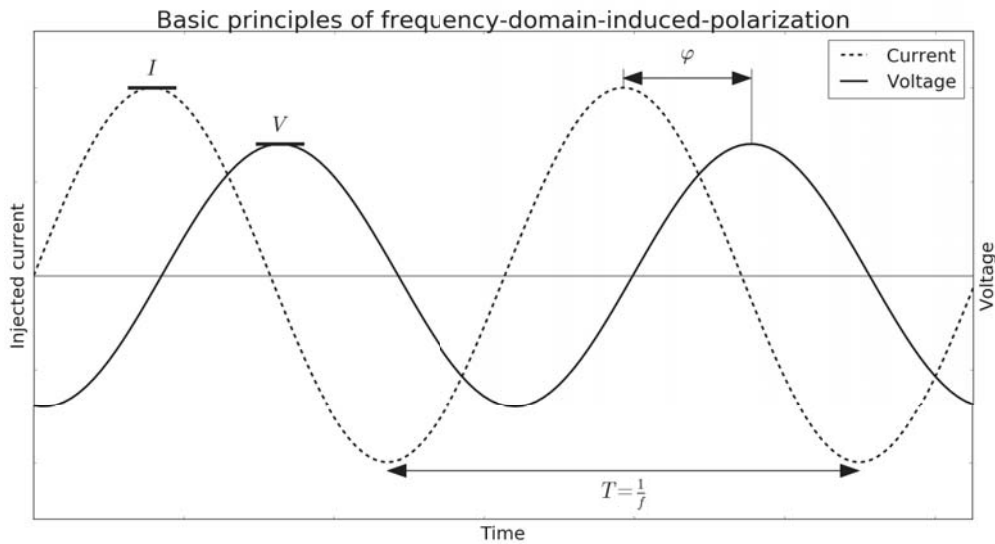


Figure 2.3: Signals and measurement principle of frequency-domain-induced-polarization.

2.3 Electrode configuration

The electrode configuration describes the geometry of the electrodes of the four electrode array used for current injection (referred to as A and B) and voltage measurement (referred to as M and N) and defines the resolution of a survey. Widely deployed is the Dipole-dipole (DD) configuration where the quadrupole of electrodes consists of a separated current and potential dipole. Measurements with interchanged dipoles (i.e. the electrodes M and N for the current injection and A and B for the potential measurement) from the "normal" configuration are being referred to as reciprocal readings. The general principle of the DD configuration is illustrated in the left panel of figure 2.4. The separation a between the electrodes of the current and potential

2.3 Electrode configuration

dipole commonly stay fixed and are equal. Depending on the skipped electrodes in between, the particular DD configurations are being referred to skip-0 to skip- x (where x is the number of skipped electrodes between A, B respectively M, N). Configurations with a larger separation between the current and potential dipole, as illustrated in the second row on the left panel of figure 2.4, are typically associated with "deeper" measurements. However, with increasing distance between the dipoles as well as higher skip values, the signal strength decreases. Configurations composed of several different skip values are being in this thesis referred to as mixed-skip DD configurations.

The Multiple-gradient (MG) array (Dahlin and Zhou, 2006) is another commonly used configuration which can provide similar resolution to the DD configuration. Moreover, the authors found that the signal strength is significantly higher making it an attractive alternative especially for conditions where only low signals are being expected. The right panel of figure 2.4 illustrates the principle. The configuration consists of a large current dipole and a potential dipole nested within which is being moved from one side to the other (A to B). Increasing the size a and b of the potential and current dipole leads to "deeper" measurements. Multiple-gradient configurations typically consists of current dipoles with different sizes and potential dipoles with multiple skip values. In contrast, Gradient arrays commonly only apply one skip value for the potential dipole.

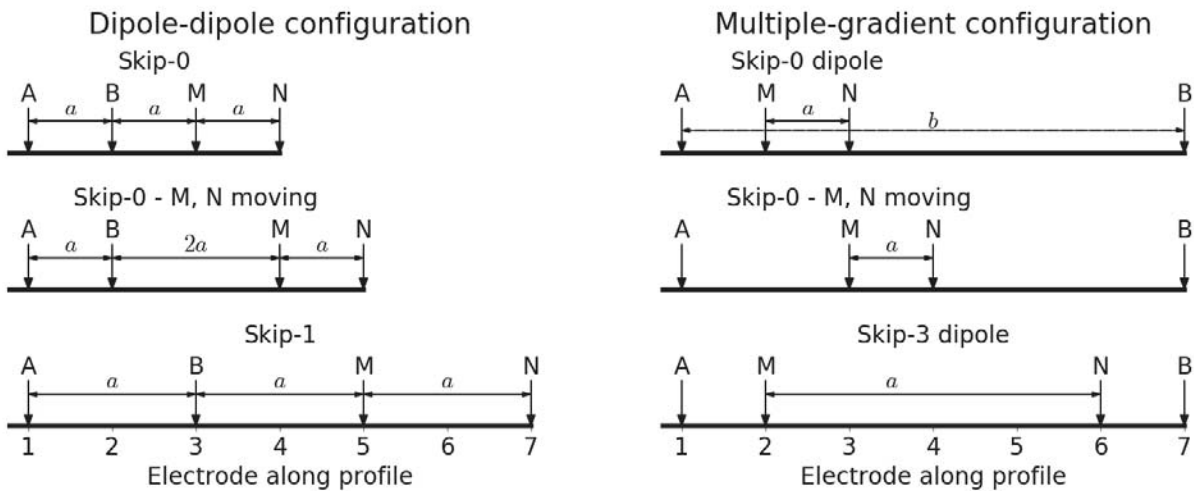


Figure 2.4: Geometry of the electrodes for the Dipole-dipole (left panel) and Multiple-gradient (right panel) configuration. A, B are the electrodes of the current dipole - M, N of the potential dipole. Depending on the requirements of the survey, the separations a and b need to be adapted accordingly.

2.4 Inversion

2.4.1 Complex resistivity inversion

Inversion of the IP data was performed using CRTomo, a smoothness-constraint inversion code by Kemna (2000). For a complete description of the algorithm please refer to Kemna (2000). The forward modelling, which consist of computing the distribution of complex resistivity values $\rho = |\rho|e^{i\varphi}$ with $|\rho|$ = magnitude respectively resistivity and φ = phase of the complex resistivity and $i = \sqrt{-1}$ = imaginary unit, is based on a finite element discretization of the model space and the solution of a complex-valued 2.5D Helmholtz equation for a given number of transfer impedances Z . The transfer impedances are a complex representation of the measured data values and are given by equation 2.4

$$Z = \ln R + i\varphi \quad (2.4)$$

with R being the transfer resistance (see equation 2.1). The inversion algorithm iteratively minimizes the L_2 norm of the objective function following the Tikhonov approach (Tikhonov and Arsenin, 1977) where the data misfit and first order model roughness are being balanced by means of a regularization parameter. The iterative process is stopped when the *rms* data-misfit value, as formulated in equation 2.5, reaches the value of one for the smoothest possible model.

$$rms = \sqrt{\frac{1}{n} \sum_{j=1}^n \frac{|d_j - f_j(m)|^2}{|\varepsilon_j|^2}} \quad (2.5)$$

The parameters in equation 2.5 are the model vector m (here the log-transformed complex resistivity), $f_j(m)$ the forward model operator, the data point d_j (as the log-transformed complex impedance $d_j = \ln Z_j$) and the error ε_j for which is being assumed that it is uncorrelated and normally distributed. The error ε_j can also be considered as a confidence region ellipse around the corresponding data point d_j , following the formulation

$$\varepsilon_j = s(\ln |Z_j|) + i s(\varphi_j). \quad (2.6)$$

In equation 2.6, $s(\ln |Z_j|)$ and $s(\varphi_j)$ represent the standard deviations of the log-transformed magnitude $\ln |Z_j|$ and φ_j of the complex impedance Z_j . i is again the imaginary unit. Note here, that $s(\ln |Z_j|)$ typically dominates $s(\varphi_j)$ in the complex error and thus controls the inversion behavior, in particular the stopping criterion. To account for that, additional real valued inversions can be computed for the phase data separately, once the complex inversion has reached an rms of one. The formulation of the rms data misfit value which is sought to be minimized is

then

$$rms_{phase} = \sqrt{\frac{1}{n} \sum_{j=1}^n \frac{\text{Im}(d_j) - \text{Im}(f_j(m))^2}{s(\varphi_j)}} \quad (2.7)$$

This additional inversion step is referred to as *final-phase improvement* (FPI).

2.4.2 Parameterization of resistance error

As can be easily seen in equation 2.5 the inversion results are strongly dependent on a proper parameterization of the data error. The overestimation of data error typically leads to under-fitted electrical images, lacking the contrast needed for a quantitative interpretation whereas an underestimation of data error typically results in images with a lot of artifacts, also threatening to be pitfalls during the interpretation (LaBrecque et al., 1996).

LaBrecque et al. (1996) proposed a linear relationship between the measured resistances (with $R = |Z|$) and their associated error $s(R)$. The model (Slater et al., 2000) writes as

$$s(R) = a + bR \quad (2.8)$$

with a being the absolute resistance error for small resistance values and b being defined as the relative resistance error for larger resistance values. The authors however observed that noise estimates from simple repeating measurements often greatly underestimate the true data error (which is also true for phase measurements) and proposed the parameterization of a and b based on the standard deviations of the differences between resistance values in a normal and reciprocal configuration. For further details on the normal-reciprocal methodology please refer to section 2.7, LaBrecque et al. (1996) and Flores Orozco et al. (2012b).

2.4.3 Parameterization of phase error

To date, well-established data error quantification methodologies are based on the normal and reciprocal misfit of the phase values. In the first reported work of Ramirez et al. (1999), the authors defined a constant value to describe the error of the phase data, based on the misfit between the normal and reciprocal phase measurements and their corresponding average value. In 2006, Slater and Binley showed that the estimation of a constant phase error as the standard deviation of the entire normal-reciprocal phase misfit distribution could improve the computed images. Recent work, by Flores Orozco et al. (2012b), proposed an inverse power law relationship between the error in phase $s(\varphi)$ and the associated resistance R

$$s(\varphi) = aR^b \quad (2.9)$$

with $b < 0$. Such model considers that resistances may be used as a first proxy to assess the signal strength. The adaptation of the proposed error model to an appropriate inversion scheme (Kemna, 2000) also yielded improved images with negligible artifacts.

2.5 Site description and TDIP survey

The TDIP measurements used within this thesis were collected on the Shiprock Site (New Mexico, USA) on the grounds of a former uranium-processing facility. The site has been remediated but measurable concentrations of uranium are still present in water samples. The site's lithology consists of three main units: an impermeable clay-rich layer extending from the surface to ~ 2 m depth, followed by a sandy-gravel aquifer (~ 3 m thickness) that rests on top of a low-permeable shale known as Mancos formation. Figure 2.5 presents a schematic cross section of the site's lithology. The groundwater level was located at a depth ~ 2 m during the field surveys.

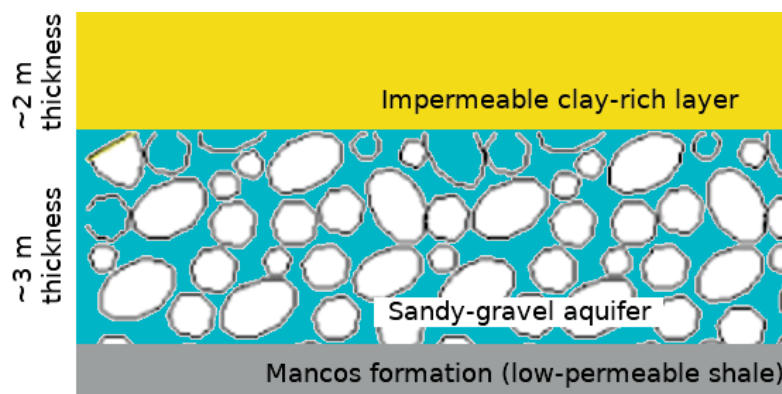


Figure 2.5: Schematic cross section of the lithology at the Shiprock Site consisting of an impermeable clay-rich top layer, a sandy-gravel aquifer and a low-permeable shale referred to as Mancos formation.

Studies on similar sites (Wainwright et al., 2015) revealed that fluviably deposited organic material within aquifer sediments naturally stimulates the activity of subsurface microorganisms leading to both the natural immobilization of uranium and the accumulation of reduced end products (minerals and pore fluids). In order to map these possible hot spots, which are expected to generate measurable IP anomalies, a total of 22 TDIP profiles were collected. Six long profiles (up to 350 m) were laid out to fairly characterize large-scale changes in the electrical properties across the floodplain and 16 shorter profiles helped to improve the resolution of particular areas of interest (see figure 2.6). Separation between electrodes was 2 m for all measurements using the Syscal Pro Switch 72 equipment (from IRIS Instruments) with a square-wave current injection and a pulse length of 2 s. The voltage decay was measured along 20 gates - of 80 ms duration each, starting after an initial delay of 240 ms after current shut-off. The measurements were

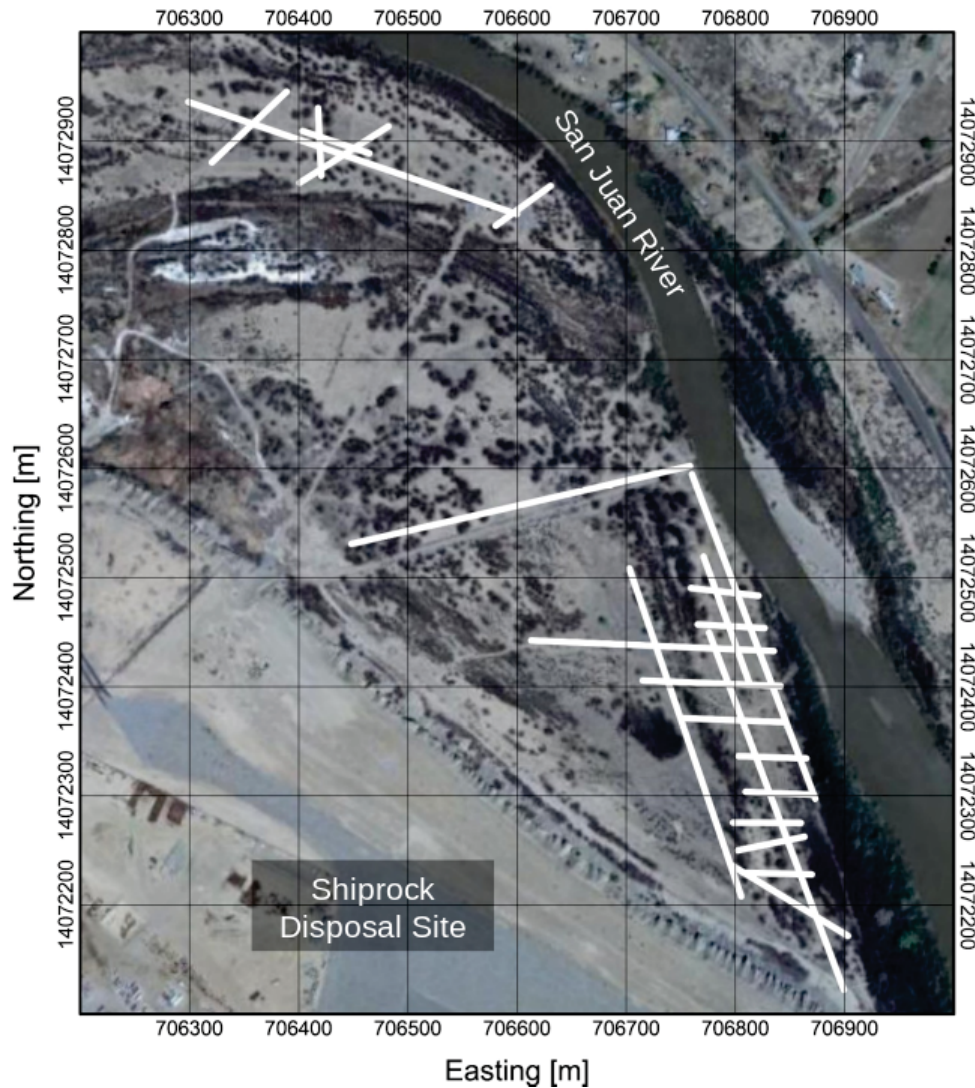


Figure 2.6: *Distribution of the TDIP profiles (white lines) at the Shiprock Site. Satellite image modified from GoogleEarth.*

collected using two configurations: a) DD skip-0 (i.e. a length of 2 m for both current and potential dipoles), and b) MG configurations with 10 potential dipoles (skip-0, skip-1 and skip-2) nested within the current dipole. DD measurements were collected as normal-reciprocal pairs. In order to reduce acquisition time, the depth of investigation was limited to 7 m, which fairly covers the aquifer and the uppermost part of the Mancos Shale.

2.6 Pseudosections

Pseudosections are an approach to visualize measured data and can also be used to display other parameters associated to measurements such as the corresponding standard deviations or signal

strengths. Every point in the pseudosection represents one measurement (i.e. one particular electrode quadrupole) and the lateral position and (pseudo)-depth are a function of the associated electrodes used for the measurement. For MG and mixed-skip DD configurations it can therefore happen that different measurements are related to the same plotting point. Hence, for such cases the sizes for the plotting points are being adjusted accordingly. Pseudosections should not be used for a direct interpretation of the electrical properties, as for example topographic effects are not taken into account. The visualization of the measured data is however commonly used to get a first thought on the data quality and the order of magnitude of the to be expected electrical properties. For example can measurements contaminated with particular systematic errors, e.g. arising from badly connected electrodes, be easily identified in pseudosections. This should be illustrated by the following example.

The panels a) to d) in figure 2.7 present the pseudosections of the apparent integral chargeability M_{int} and logarithmic apparent resistivity ρ obtained from a forward modelling for a DD and MG configuration. The forward modelling was performed using CRMod by Kemna (2000) and the corresponding three layer models, which should be representative for the Shiprock Site (c.f. section 2.5), are shown in figure 2.8. Please note that for the modelling the integral chargeability values were converted to phase-shift values following the approach mentioned in section 2.2. Figures 2.7 a) and b) illustrate the differences in the distributions of the points within the pseudosections for the DD and MG configurations, resulting from the different rules for the computation of the (pseudo)-depth for both configurations. Panels e) to h) of figure 2.7 illustrate the effects of random and systematic errors on the appearance of data in the pseudosection. The systematic error is simulated as a badly connected electrode 30, whereas the random error consists of adding gaussian noise to the signal. The characteristics of the gaussian noise can be found in table 2.1.

As can be seen is the introduced systematic error visible as bands of anomalously high values without spatial correlation within the data set and the patterns are different for the electrode configurations. Systematic errors can normally be identified and need to be removed prior to the inversion to prevent the creation of artifacts. The random error on the opposite, affecting all measurements, is practically impossible to remove as commonly neither the variance nor the distribution of it is known. It is however commonly assessed by finding a description of it (typically via a proxy) and the modelling of it's effects during the inversion.

	mean (center of distribution)	standard deviation (width of distribution)
Resistivity	0	0.5 [mV/V]
Chargeability	0	15 [Ω m]

Table 2.1: *The characteristics of gaussian noise simulating the random error in measurements.*

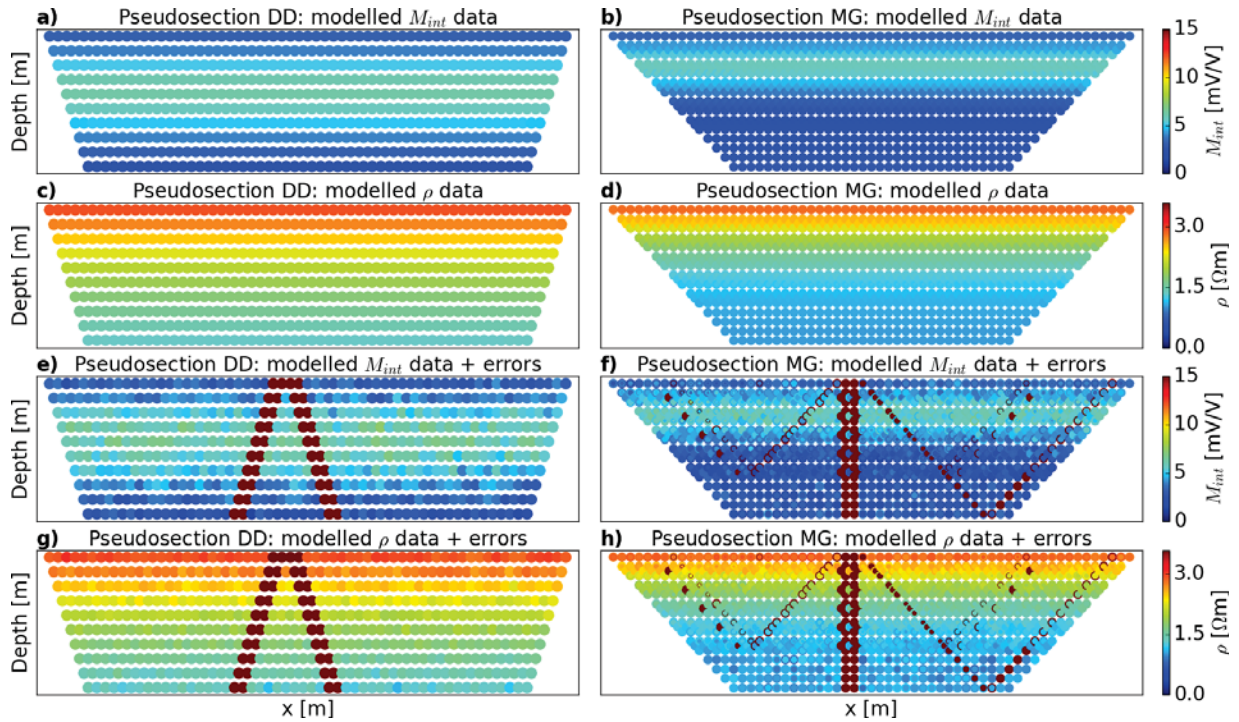


Figure 2.7: a) to d) present the pseudosections of the forward modelled electrical properties for a DD and MG configuration. Every point in the pseudosections corresponds to a particular electrode quadrupole and the calculation for the (pseudo)-depth is dependent on the type of electrode array. e) to h) show the pseudosections after the contamination with systematic and random errors.

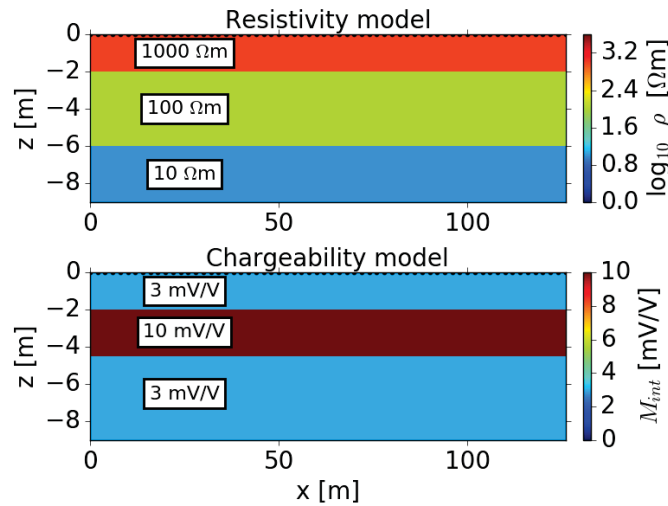


Figure 2.8: The three layer models of the resistivity (top) and chargeability (bottom) used for the forward modelling with a DD and MG configuration. The models should be representative for the Shiprock Site.

2.7 Normal-reciprocal approach

The state-of-the-art methodology for the characterization and removal of systematic errors as well as the quantification of data error is the analysis of the discrepancy of measurements collected in normal and reciprocal configuration. Numerous studies report the successful application of the normal-reciprocal approach (NRA) spanning various areas (e.g. Krautblatter et al. (2010), Koestel et al. (2008), Yang et al. (2014), LaBrecque and Daily (2008), Flores Orozco et al. (2011) and Flores Orozco et al. (2015) and others). Initially proposed for resistance measurements R only (Binley et al., 1995; LaBrecque et al., 1996), the approach has soon been applied to IP measurements (Slater and Binley, 2006; Flores Orozco et al., 2012b).

The approach is based on the calculation of the misfit between R , φ or M_{int} collected in the normal and reciprocal configuration and a following statistical analysis of the misfits. For the approach described here, the measured electrical values of the normal and reciprocal configuration are being averaged and form a new data set. Another possible option consists of keeping the normal and reciprocal measurements in separated data sets. However, averaging the two data sets has shown to further improve the consistency in the data. The classification of outliers is based on the misfit values and measurements, where the corresponding misfit value exceeds a specified threshold (commonly two times the standard deviation of all misfit values as for example used by Flores Orozco et al., 2012) are being classified as outliers and have to be removed. Choosing a multiple of the standard deviation becomes reasonable when looking at figure 2.9 which displays the misfit value (here the misfit of resistance ΔR) plotted against the associated transfer resistance R of an already filtered data set. The misfit value can be approximated by a normal distribution which easily justifies the standard deviation as a threshold value. The same assumption can also be made for the misfit of phase values. Distributions departing from a normal distribution indicate the presence of systematic errors.

To better understand the wide use of the NRA, the application of the misfit for the definition outliers needs to be properly addressed. Analogous to the misfit values derived by a simple repetition of measurements, misfit values of the NRA are only estimates of precision and not of accuracy (LaBrecque et al., 1996). However, due the specific design of the methodology, i.e. the interchange of current and potential dipole, a reciprocal measurement is not only a plain repetition of the measurement rather than another independent realization of the same measurement with different settings (e.g. the electrodes). By having two realizations of the same measurement kinds of systematic errors, for example problems with the electrodes, can be made visible.

The following example should illustrate the principle and advantages of the NRA over the

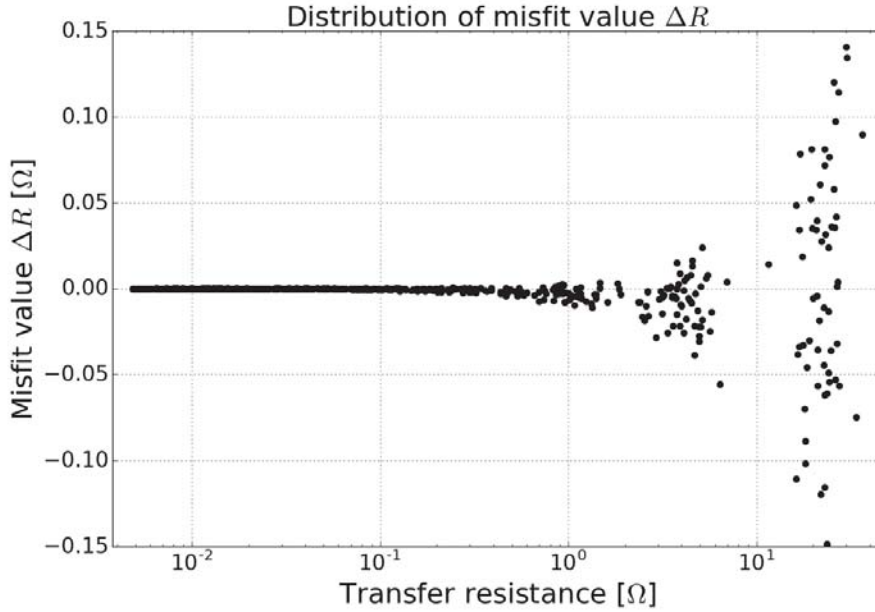


Figure 2.9: *The normal-reciprocal discrepancies for the resistance measurements plotted against their associated transfer resistances. The misfit distribution can be approximated by a normal distribution.*

repetition approach. Let's assume that in normal configuration one of the current electrodes has poor contact with the ground resulting in only low current densities being injected to the ground, resulting in a decrease in the signal strength. Depending on the subsurface conditions low current densities might lead to erroneous potential readings. A simple repetition of the same measurement will probably produce a comparable potential reading and only small variability in the misfit value. This would mean, that although the measurement might be obviously wrong, the misfit is not capable of identifying it as an outlier. On the opposite, following the NRA, for the reciprocal configuration the current injection now takes place at electrodes with proper contact to the ground and adequate current is being injected. The potential measurement might but does not necessarily need to be affected by the loosely placed electrode. In any case the reciprocal measurement will be different to the one obtained in the normal configuration thus leading to a more representative misfit value.

Nevertheless, also the NRA has its limitations. For example are there sources of noise which are fully reciprocal, meaning that they cannot be made visible by an analysis of the associated misfit. This is true for EM-coupling, which will affect the measurements in the same way regardless of the used configuration. Apart from that, there is no proper realization of the normal-reciprocal analysis for the actual decay curve in TD measurements. The NRA can only be applied on the level of the integral chargeability values, neglecting potential for in-depth analysis.

Chapter 2 Theory

There are also time and economical limitations. For large mapping campaigns, the conduction of reciprocal measurements basically doubles the amount of the acquisition time. Furthermore, measuring configurations such as the MG configuration, are not suited for the collection of reciprocal with multi-channel instruments without severely increasing the acquisition time.

Chapter 3

Fitting and Sampling of the Decay Curve

3.1 Evaluation of the sampling of the voltage decay on the derivation of the decay curve

For the understanding and design of further analysis, such as the fitting of models to the measured decay curve, it is critical to understand and investigate the effects of random noise in the voltage signal and the appropriate sampling of such noise contaminated signals. The sampling means the Mdelay and the number, distribution and width of the individual gates, whereas the gate refers to the time span used for the integration of the voltage signal as outlined in section 2.1.

The experimental set-up for this test consists of contaminating a voltage signal with different levels of gaussian noise (i.e. samples from a normal distribution) and the subsequent derivation of the corresponding decay curve with varying samplings. In order to provide an undistorted decay curve for comparison, the voltage signal has been sampled prior to the addition of noise. This experiment was conducted for two cases. The first case investigates the effects based on a modelled voltage signal, in the following referred to as the "numerical example". The numerical data was created after a power law model with an additional constant term ($V(t) = at^{-b} + c$) using a discretization of 1 ms. The other case uses a measured voltage decay, where the signal has been sampled in 10 ms steps. Here the voltage decay is already contaminated by noise, yet for this experiment it was found to be negligible. The measured voltage decay was included to (i) provide a voltage decay with another "shape" and to (ii) evaluate the effects of the samplings for a signal with a the lower discretization - 10 ms. The characteristics of the added gaussian noise can be found in table 3.1. In table 3.2 the properties of the samplings are presented. The *arithmetic* and *semi-logarithmic* samplings are standard options of the widely used Syscal Pro equipment (by IRIS Instruments). The *30ms* sampling is an artificial example to evaluate how high sampling rates and high number of gates effect the shape of the derived decay curve. Please be aware that all results shown here are only a snapshot for a given distribution of random noise and therefore all observations are a more rough description of the performance of the different samplings.

Chapter 3 Fitting and Sampling of the Decay Curve

level	mean (center of distribution)	standard deviation (width of distribution)
1	0	10
2	0	50
3	0	100
4	0	500

Table 3.1: Characteristics of the added gaussian noise for the different levels.

	Arithmetic	Semi-logarithmic	30ms	
Mdelay	240	40	30	Mdelay
Gate 1	80	40	30	Gate 1
Gate 2	80	40	30	Gate 2
Gate 3	80	40	30	Gate 3
Gate 4	80	40	30	Gate 4
Gate 5	80	40	30	Gate 5
Gate 6	80	40	30	Gate 6
Gate 7	80	40	30	Gate 7
Gate 8	80	80	30	Gate 8
Gate 9	80	80	30	Gate 9
Gate 10	80	80	30	Gate 10
Gate 11	80	80	...	Gate ...
Gate 12	80	80	30	Gate 58
Gate 13	80	80	30	Gate 59
Gate 14	80	80	30	Gate 60
Gate 15	80	160	30	Gate 61
Gate 16	80	160	30	Gate 62
Gate 17	80	160	30	Gate 63
Gate 18	80	160	30	Gate 64
Gate 19	80	160	30	Gate 65
Gate 20	80	160	30	Gate 66

Table 3.2: Mdelay, gate widths, gate numbers and their distribution for three different samplings. Note here, that all values are given in ms and that the 30ms sampling has 66 gates instead of 20.

Figure 3.1 presents the experiment's outcome for the numerical case. The left panels show the modelled voltage signal (red line) contaminated with different levels of noise (black line) as indicated in table 3.1. The right panels show the derived decay curves for the different sampling types (colored lines) as well as the decay curve for the undistorted case (black line). For the first level of noise all samplings are capable of reproducing the shape of the actual undistorted decay curve, only small differences can be observed. However, as soon as the noise level is increasing (second row of figure 3.1) first deviations occur. In particular after around 750 ms the semi-logarithmic sampling is not capable of reproducing the shape of the decay curve - in

3.1 Evaluation of the sampling of the voltage decay on the derivation of the decay curve

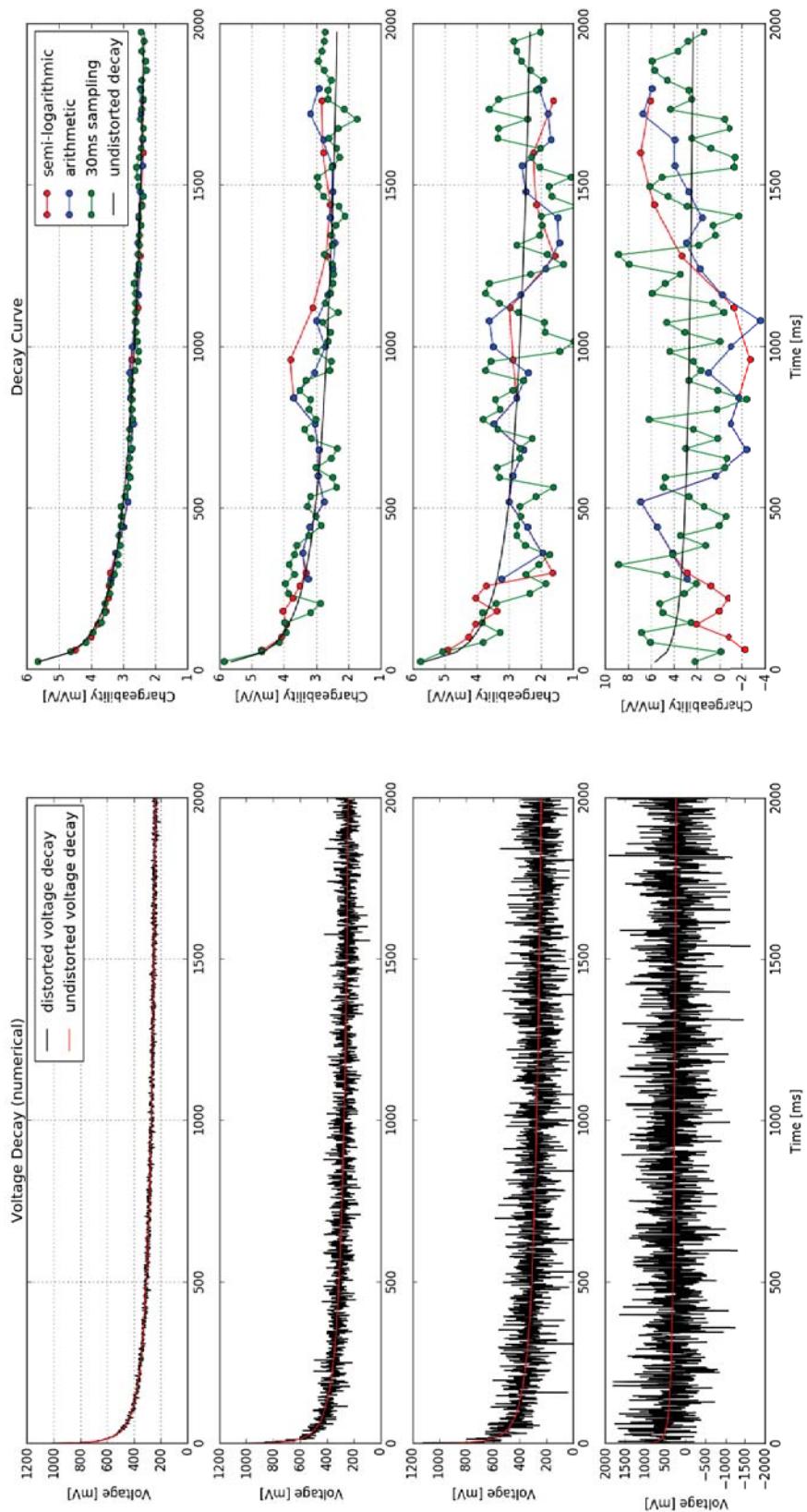


Figure 3.1: Effects of different samplings and different levels of noise on the derivation of the decay curve for a numerical example. The left panel shows the modelled voltage decay contaminated with different levels of noise and the right panel the corresponding decay curves for different samplings.

comparison with the two other types - higher sampling rates are probably needed. Row three shows the results for added noise with a standard deviation of 100. The voltage signal roughly ranges from 250-1000 mV and the maximum percentage error can be estimated at around 27% assuming a noise range of two times the standard deviation. Although being subjected to a significant level of noise, all sampling types still catch the general trend of the decay curve. The problems of the semi-logarithmic sampling observed in row two are persistent. Furthermore the arithmetic sampling underestimates the signal in the early times (from 250 to 500 ms) rendering the demand for high sampling rates there particularly for higher levels of noise. Row four of figure 3.1 clearly shows a breaking point for the methodology. Here, not even the dense 30ms sampling is capable of reproducing the original signal.

For the sake of clarity the signal of the measured voltage decay is limited to a maximum of 1200 mV as indicated by the dashed red line in figure 3.2. Compared to the numerical example the measured voltage decay has a much more pronounced decrease in the early times, which together with the coarser discretization marks the main differences between the numerical and measured case. Figure 3.3 shows the voltage signal with the different levels of added noise (left panels) and the corresponding decay curves for the tested samplings (right panels). Compared to figure 3.1 the noise exhibits a different pattern contributed to the differences in the discretization of the numerical and measured decay. The general shape of the decay is being resolved for any sampling for the first three noise levels. If of interest, the strong decrease in the early times however, would demand even higher sampling rates than the 30 ms used here. Consistent to the numerical case, the sampling methodology seems to be limited to specific amounts of random noise - resulting in unsatisfactory decay curves in comparison with the undistorted case. Results for this case are shown in the fourth row of figure 3.3. Although it seems that the general shape of the decay curve is being resolved, the fluctuations of the decay curves of the different samplings around the undistorted decay curve are much higher than the actual signal.

Based on both the numerical and measured case the following general statements can be made:

- The common methodology outlined in section 2.1 consisting of partitioning the voltage decay into gates and the subsequent integration within the gates (i.e. the derivation of the decay curve) appears to be a robust tool and can capture the general shape of the voltage decay. The integration in the gates makes it applicable even to high levels of random noise.
- The sampling needs to be chosen based on the requirements of the survey. If the decay in the early times is of interest high sampling rates and small M_{delays} are needed.
- Wider gates at the late times can smoothen out the decay curves (due to the integration in equation 2.2). They are however also prone to an under- respectively overestimation of the shape of the decay particularly for cases with high levels of noise.

3.1 Evaluation of the sampling of the voltage decay on the derivation of the decay curve

- Both the numerical and measured data case show a similar behavior of the sampling types and only minor differences between a high and lower discretization of the voltage decay as basis for the sampling can be observed.

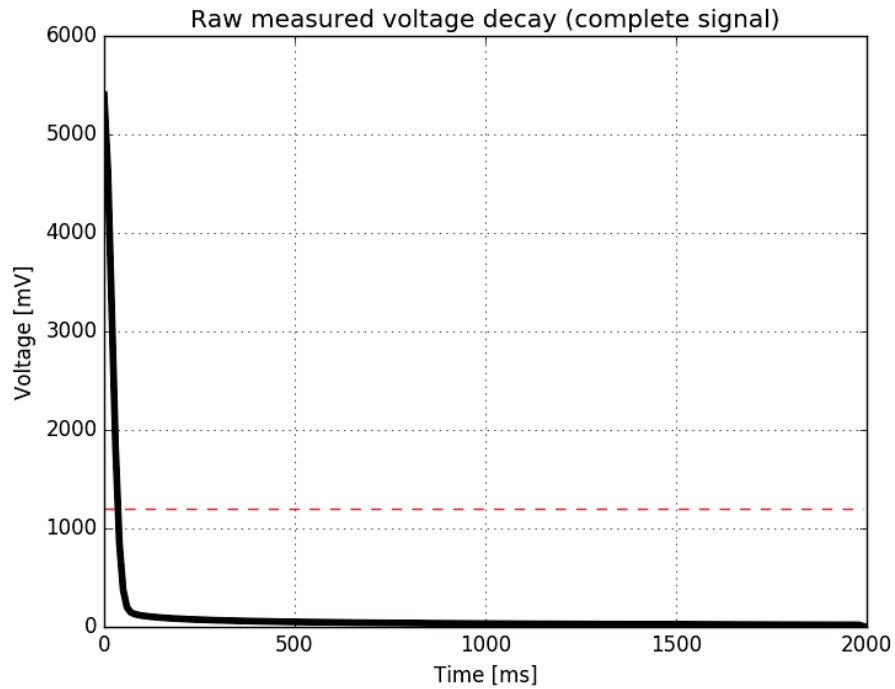


Figure 3.2: Raw measured voltage decay collected with a sampling consisting of 10 ms large gates. The red dashed line indicates where the signal is cut-off for the subsequent analysis.

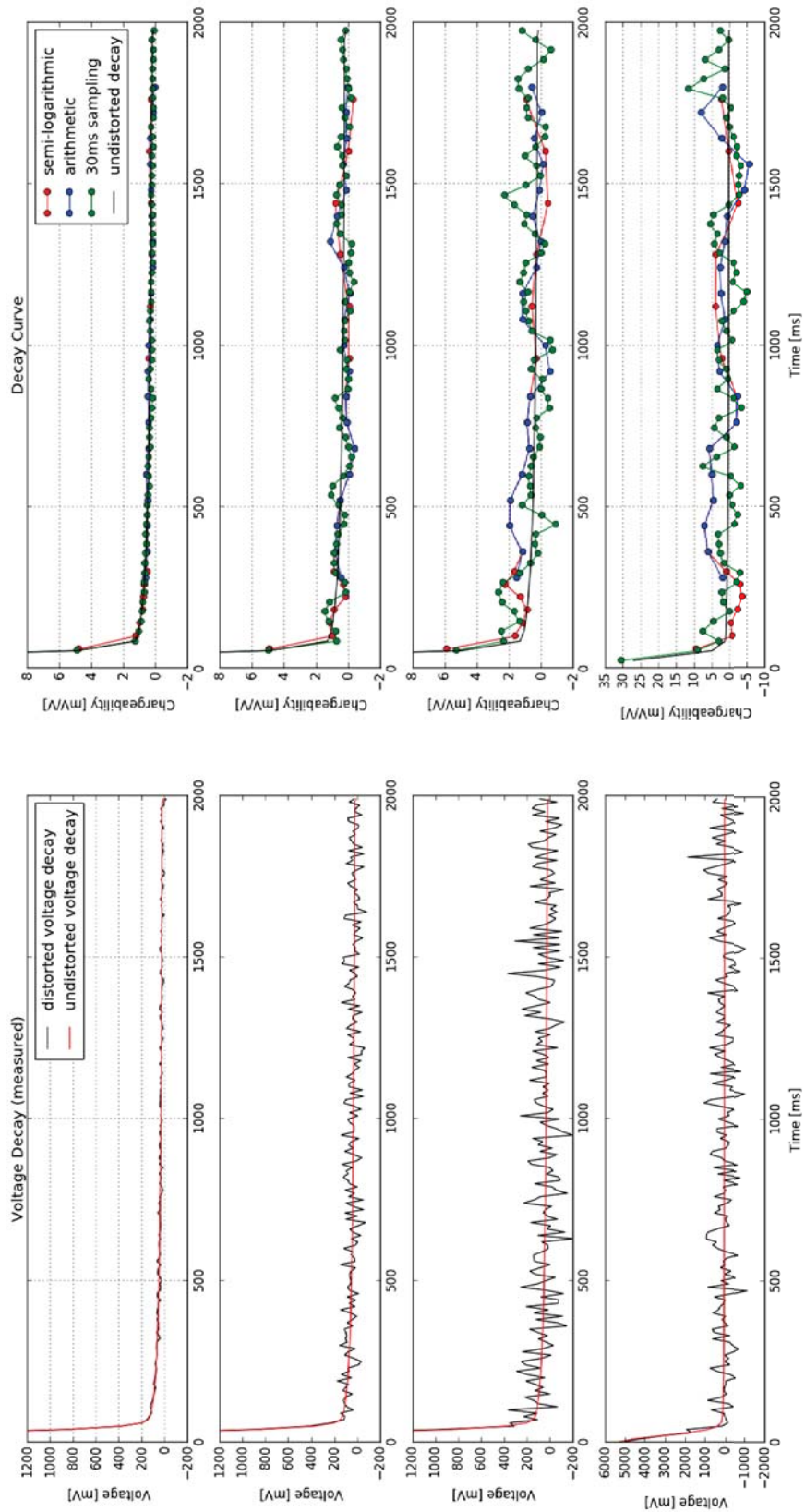


Figure 3.3: Effects of different samplings and different levels of noise on the derivation of the decay curve for a measured voltage decay. The left panel shows the voltage decay contaminated with different levels of noise and the right panel the corresponding decay curves for different samplings.

3.2 Evaluation of appropriate fitting models

As the fitting of model curves to the measured decay curves is one of the major components of the DCA it needs to be addressed in detail. The fitted model curves are commonly used to either get a smooth description of the measured decay curve as for example needed for an easier comparison with other curves of the data set (refer to chapter 5) or to characterize the inherit random noise of such measurements for the incorporation into an inversion scheme (refer to chapter 6). In particular a model function is sought which fulfills the following conditions:

- Best fitting function with a minimum number of parameters applicable to decay curves obtained with any kind of sampling, i.e. the distribution, width and number of IP gates.
- Weak dependence on starting values
- High chance on convergence
- Computationally inexpensive (as hundreds to thousands of models will need to be processed)

In order to reduce the number of the to be considered model functions a preliminary test with three models of the *exponential* family as well as three models of the *power law* family has been performed. The equations of the different model functions write (with e being Euler's number):

$$pow : f(x) = ax^{-b} \tag{3.1a}$$

$$pow2 : f(x) = ax^{-b} + c \tag{3.1b}$$

$$powm : f(x) = ax^{-b} + x^{-c} \tag{3.1c}$$

$$exp0 : f(x) = ae^{-bx} \tag{3.2a}$$

$$exp1 : f(x) = ae^{-bx} + c \tag{3.2b}$$

$$exp2 : f(x) = ae^{-bx} + ce^{-dx} \tag{3.2c}$$

Possible model functions of the *fourier* family (where the data are approximated by a sum of sin and cos functions) were not considered as the number of model parameters exceeds any of the six models above. Models of the *rational* family, although fitting most of the decay curves quite well, turned out to be too sensitive on starting values and a proper convergence could not be guaranteed. Lastly, commonly used models of the *cole-cole* family were investigated as well and are covered separately (see section 3.3).

Chapter 3 Fitting and Sampling of the Decay Curve

The fitting of any of the six model functions (equations 3.1a-c, 3.2a-c) obviously consists of solving a non-linear least squares problem. In particular model parameters are sought, so that the sum of the squares of the deviations is minimized:

$$\sum_{i=1}^k (f(x_{i,1}, \dots, x_{i,n}) - y_i)^2 \rightarrow \min! \quad (3.3)$$

In equation 3.3, y_i are the partial chargeability values of the decay curve and $f(x_{i,1}, \dots, x_{i,n})$ are the partial chargeability values of the model function. Unless otherwise stated, all non-linear least squares problems in this Master's thesis are solved using the well-known *Levenberg-Marquardt* algorithm. For more details on the algorithm please refer to Moré (1978) and Gill and Murray (1978). To get a statistical measure on the goodness of fit (gof) the *root-mean-square deviation* (RMSD) is evaluated for all models. It writes:

$$\text{gof} = \text{RMSD} = \sqrt{\frac{1}{n} \sum_{i=1}^n (m_f(t_i) - m_{m,i})^2} \quad (3.4)$$

n is the number of gates, $m_f(t_i)$ the partial chargeability of the fit at times t_i and $m_{m,i}$ the measured partial chargeability.

Figure 3.4 shows the fitted model curves (colored lines) for the exponential family (left panel) and the power law family (right panel) as well as the measured decay curve (black dots), acting as the input data for the fitting. A smooth decay curve, representative for conditions with a high SNR, was chosen in order to evaluate the general performance of the different models to describe the decay. Later in this section the fitting of models to more erroneous decay curves will be tested. It is obvious that the *exp0* model is not flexible enough to fit the decay. By modifying the initial model, which evidently goes along with an increase in model parameters, the decay is fitted far better and the calculated gof values are quite low (0.06 and 0.02 for *exp1* and *exp2* and 0.23 with the initial model *exp0*). All model curves of the power law family fit the decay to an acceptable degree with no differences being observed for the *powm* and *pow* model (also consistent in the gof values of 0.10). The best performing model is *pow2* which perfectly describes the measured decay and reaches the minimum gof value of 0.01. Based on this initial test, three models were chosen to test their performance on less smooth decay curves (i.e. more erroneous decay curves), as well as for varying pulse lengths and decay curves obtained with different samplings. The models and the individual selection criteria are stated in table 3.3.

Figure 3.5 shows the fitted model- (colored lines) and measured decay curves (black line) for decay curves obtained with arithmetic samplings for three different pulse lengths of 1 (left panels), 2 (center panels) and 4 s (right panels). Each individual row indicates a different SNR

3.2 Evaluation of appropriate fitting models

model	number of parameters	goodness of fit (gof)	selection criterion
<i>pow2</i>	3	0.01	lowest gof
<i>exp2</i>	4	0.02	2nd lowest gof
<i>pow</i>	2	0.1	only 2 parameters, acceptable gof

Table 3.3: The selected models for the fitting evaluation to less smooth decay curves as well as decay curves obtained with different samplings and pulse lengths.

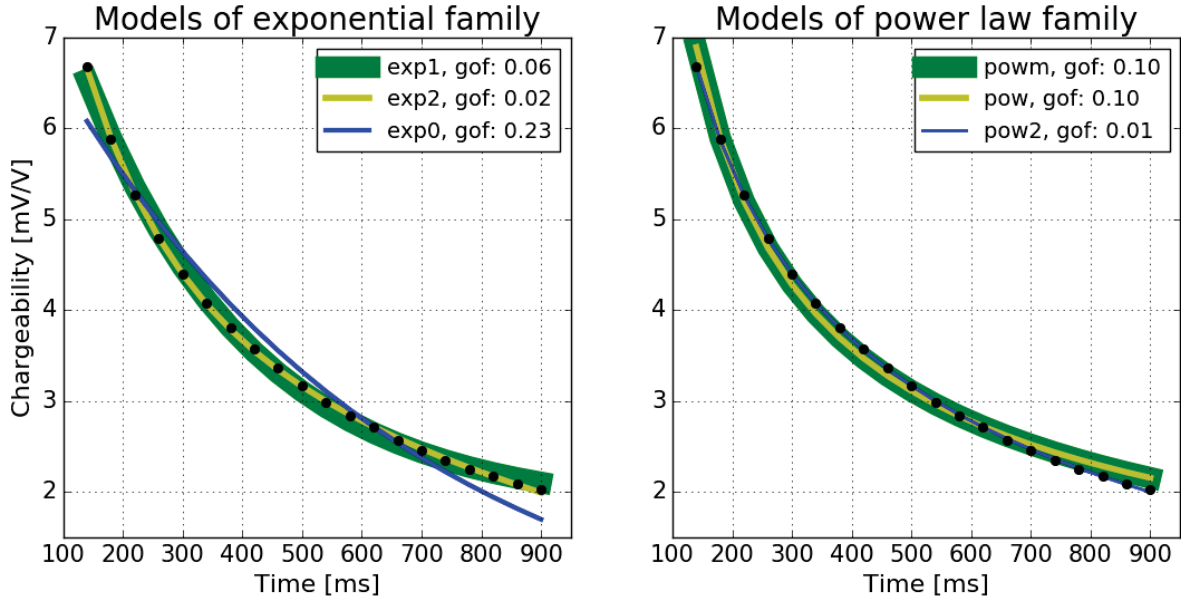


Figure 3.4: First evaluation of the fitting results for models of the exponential and power law family.

starting with a high value in the first row and decreasing downwards. All decay curves are from field data sets (obtained with a Syscal Pro unit) and the assignment of the SNR values was done based on the geometrical factor k for each measurement (please refer to section 2.1). Furthermore each row's measurements were collected with the same quadrupole of electrodes and thus the decay curves for the different pulse lengths should be comparable.

What can be seen obviously and consistently to the preliminary test is that the *pow* model is not flexible enough to fit most of the decay curves. Another important observation is the unintentional overfitting of the *exp2* model for two decay curves (third plot in the second row and first plot in the third row of figure 3.5). In such cases the gof value may not be used to evaluate the performance of the model. The gof will clearly be low despite the unusable fitting results. As expected, does the *pow2* model fit all decay curves with satisfying results. A similar comparison, as presented in figure 3.6 shows consistent results. Here, instead of using decay curves obtained with an arithmetic sampling, the decay curves obtained with a semi-logarithmic gate distribution as well as the corresponding fitted model curves are shown. The overfitting and

Chapter 3 Fitting and Sampling of the Decay Curve

the inflexible behavior of the *exp2* and *pow* model observed in figure 3.5 still occur. Consistently, the same observations can be made for data acquired with a sampling using 34 gates instead of 20. The decay curves and the fitted models are shown in figure 3.7.

Concluding, with the *pow2* model, a simple model with a minimum of parameters was found which is capable of fitting almost any tested decay curve without the threat of under- or over-fitting. Even for very erroneous and non-decaying curves (not shown here) good results can be achieved. Furthermore neither numerical instabilities respectively convergence problems nor a strong dependence on the starting values were observed and the computational effort to fit numerous decays is very limited.

3.2 Evaluation of appropriate fitting models

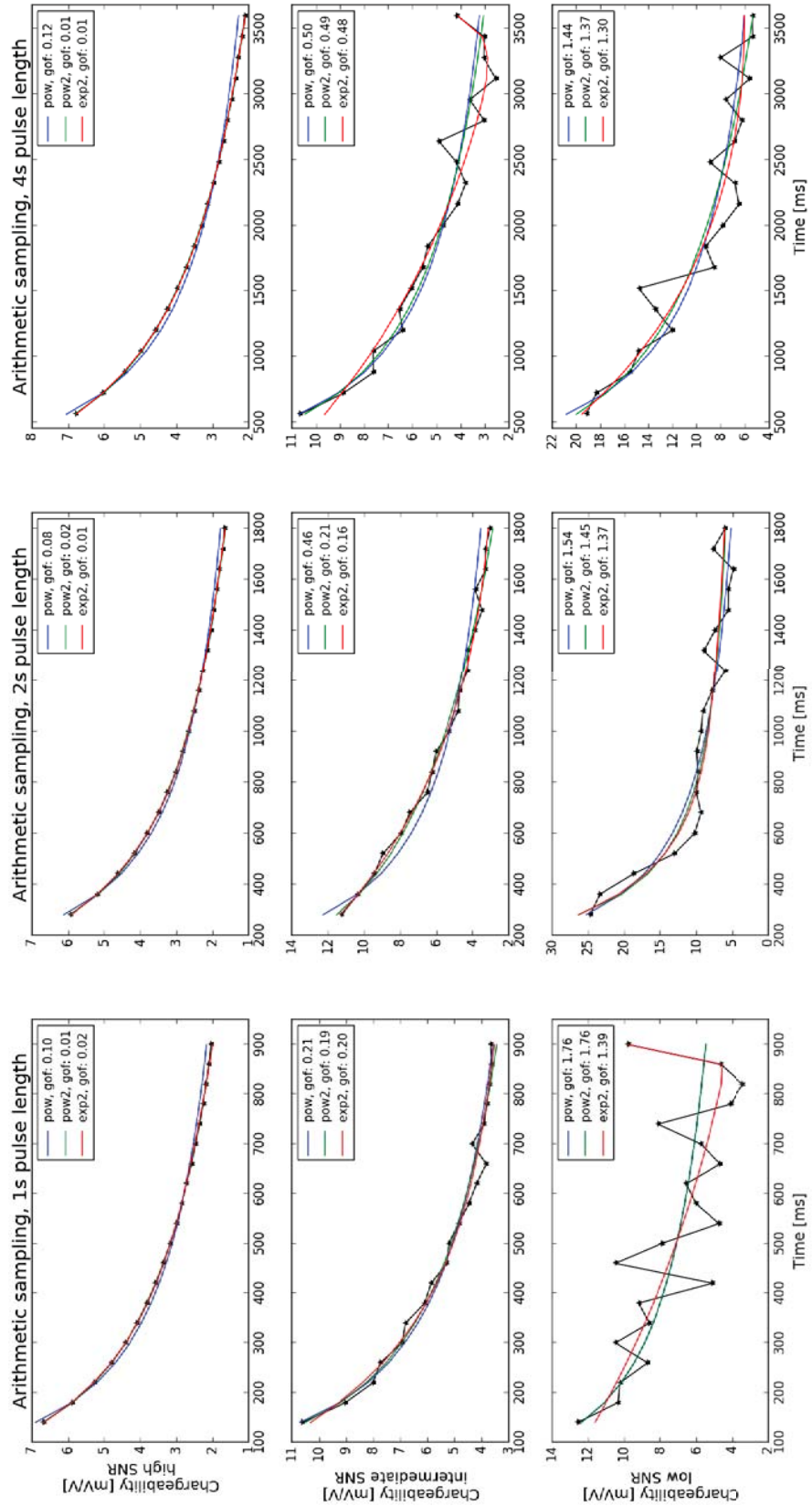


Figure 3.5: Fitted models (colored lines) and measured decay curves (black line) for an arithmetic gate distribution and three pulse lengths as well as different SNR (individual rows).

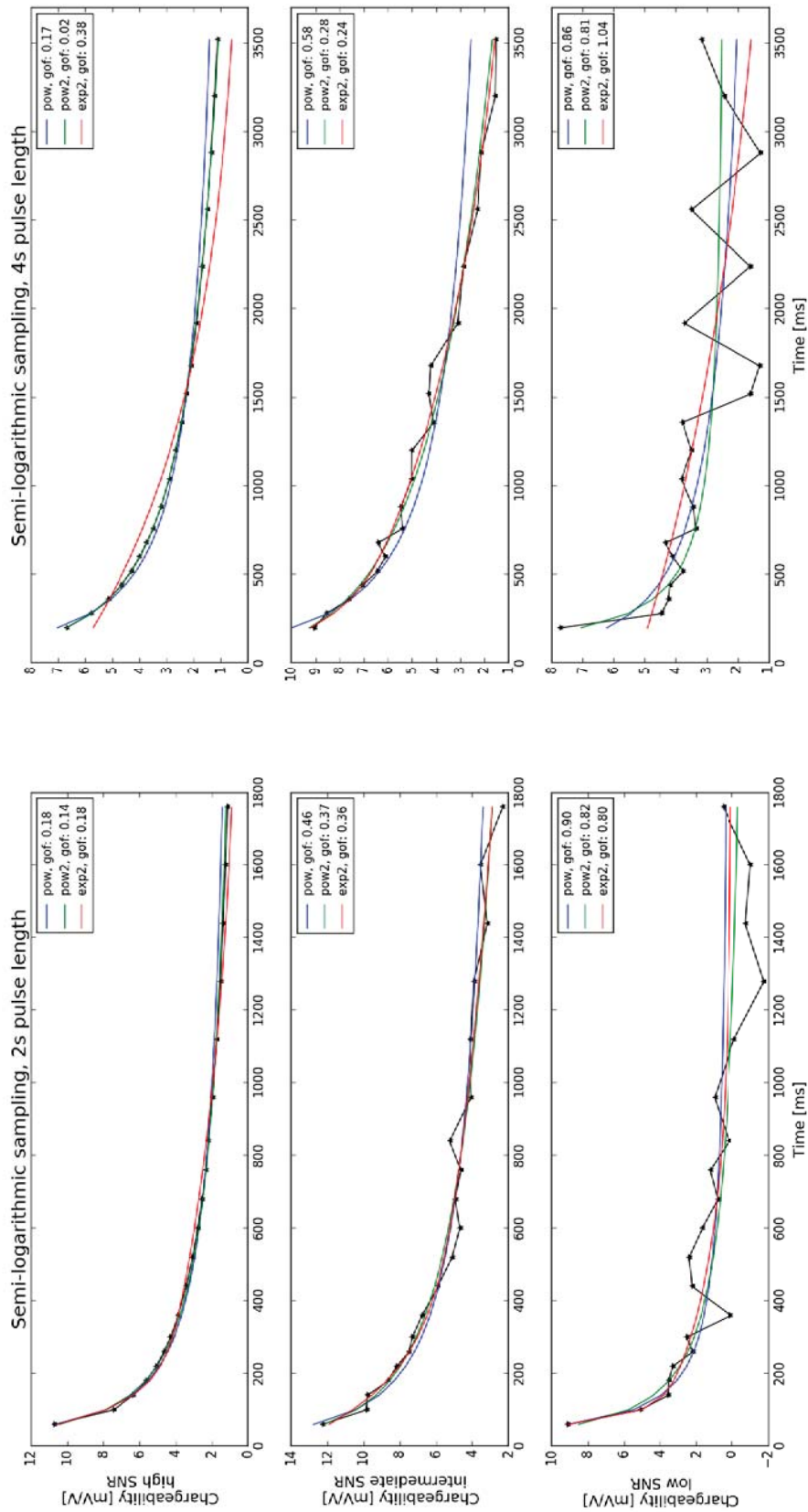


Figure 3.6: Fitted models (colored lines) and measured decay curves (black line) for an semi-logarithmic gate distribution and two pulse lengths as well as different SNR (individual rows).

3.2 Evaluation of appropriate fitting models

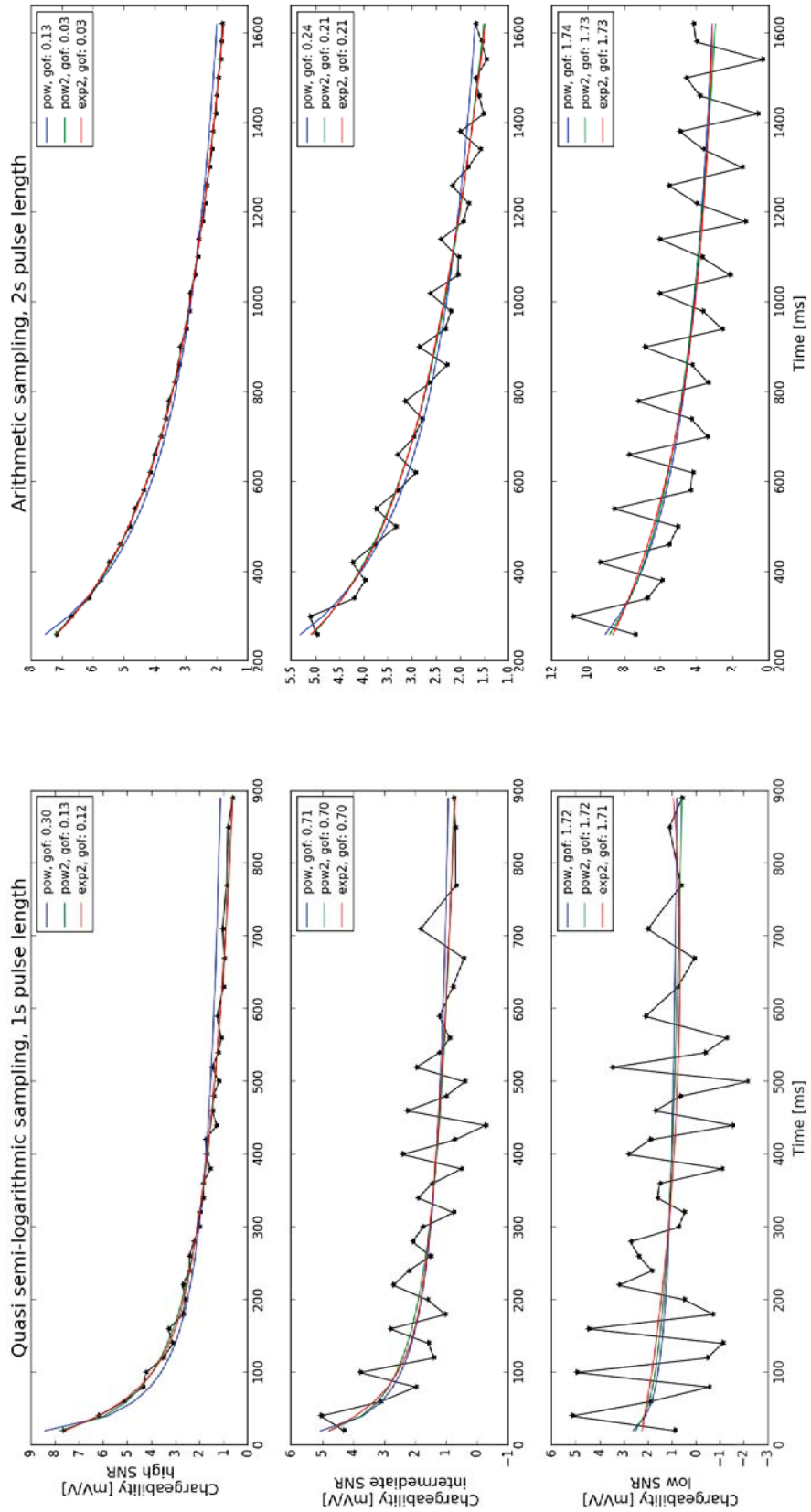


Figure 3.7: Fitted models (colored lines) and measured decay curves (black line) for different sampling types and pulse lengths as well as different SNR (individual rows).

3.3 Fitting of the time-domain Cole-Cole model

The Cole-Cole model (Cole and Cole, 1942) is a dispersion model that can be used to describe the polarization response, i.e. the relaxation curve measured in TDIP. Cole-Cole parameters can be related to the grain size distribution as well as the mean grain size (Chelidze et al., 1999; Kemna, 2000) and are widely used (Binley et al., 2005; Koch et al., 2011; Revil et al., 2014). Initially introduced for the frequency-domain, Pelton et al. (1978) proposed a time-domain formulation. Fitted to a decay curve, it is possible to determine the frequency depend parameters of the IP effect based on measurements collected in the time-domain. From that point of view it would be well reasonable to use this model instead of the power law model due a possible linkage to physical parameters. This section is sought to be a comparison of the Cole-Cole model and the power law model by means of the goodness of fit, the convergence, the dependence on starting values as well as the computational effort.

Equation 3.5 shows the time-domain Cole-Cole model as used by Pelton et al. (1978) as well as the corresponding Python implementation.

$$M(t) = M_0 \sum_{n=0}^{\infty} \frac{(-1)^n \left(\frac{t}{\tau}\right)^{nc}}{\Gamma(1 + nc)} \quad (3.5)$$

```
import numpy as np
from scipy.special import gamma

def ccm_p(t, c, tau, M0, n):
    out = np.zeros(len(t),)
    n = np.arange(0,n)
    for iter in range(len(t)):
        out[iter] = M0*sum((( -1)**n * (t[iter]/tau)**(n*c))/gamma(1+n*c))
    return out
```

M_0 , τ and c are being referred to as Cole-Cole parameters and Γ is the Gamma function. M_0 is the chargeability for $t = t_0$, τ is a time constant that characterizes the decay and c is a dimensionless constant bounded to $[0, 1]$ which controls the frequency dependence. The extremely slow convergence of this formulation for $t/\tau < 10$ is well known (Ghorbani et al., 2007; Gazoty et al., 2012a) and the authors suggest the use of an alternative formulation after Guptasarma (1982) which writes:

$$M(t) = M_0 \sum_{n=0}^{\infty} \frac{(-1)^{n+1} \left(\frac{t}{\tau}\right)^{-nc}}{\Gamma(1 - nc)} \quad (3.6)$$

```

import numpy as np
from scipy.special import gamma

def ccm_g(t, c, tau, M0, n):
    out = np.zeros(len(t),)
    n = np.arange(0,n)
    for iter in range(len(t)):
        out[iter] = M0*sum((-1)**n+1 * (t[iter]/tau)**(-n*c))/gamma(1-n*c)
    return out

```

Fitting of a model with constrained parameters isn't possible using the same Python code and libraries as for the fitting of the power law model. The LMFIT package by Newville et al. (2014) is a powerful compilation of different optimization algorithms and was used for this purpose. For this particular non-linear optimization problem the *Levenberg-Marquardt* algorithm did not produce any meaningful results - a proper convergence was just not guaranteed even for perfect starting values. Instead the *Nelder-Mead* method (Nelder and Mead, 1965) was used which is able to fit, given a set of proper starting values (which can be deduced by trial-and-error), almost all decay curves of a data set. This is however only valid for the Cole-Cole model introduced in equation 3.6. For the initial formulation after Pelton et al. (1978) neither proper starting values nor a optimization method was found which is capable of achieving meaningful fitted models. This model was therefore not further treated and no results are shown.

Figure 3.8 shows the fitted models for equation 3.6 in comparison with the *pow2* model for two different samplings and pulse lengths. The Cole-Cole model curves approximate the measured decay curves relatively well, however the associated gof values are higher than for the power law model (e.g. 0.0418 for the Cole-Cole and 0.0081 for the *pow2* fit) and particularly in the late times of the decay deviations can be observed. This can be contributed to the constrained character of the model with parameters bound to certain limits resulting in a smaller flexibility. Furthermore, it has been demonstrated, that not all IP responses can necessarily be described by a Cole-Cole model (Nordsiek and Weller, 2008; Flores Orozco et al., 2012b). As discussed in section 3.2 the desired fitting model needs to meet some important conditions, e.g. a low sensitivity to starting values and a low computational effort. For the Cole-Cole model none of them are satisfyingly fulfilled. Particularly the condition of the best possible approximation is critical as the estimation of the random noise relies on that (please refer to chapter 6). Deviations from the measured decay as observed for the Cole-Cole model would bias the error estimates and thus the resulting electrical images.

Two models of the Cole-Cole family have been examined on their potential to fit measured decay curves and were compared with the *pow2* model. No practical and more important stable

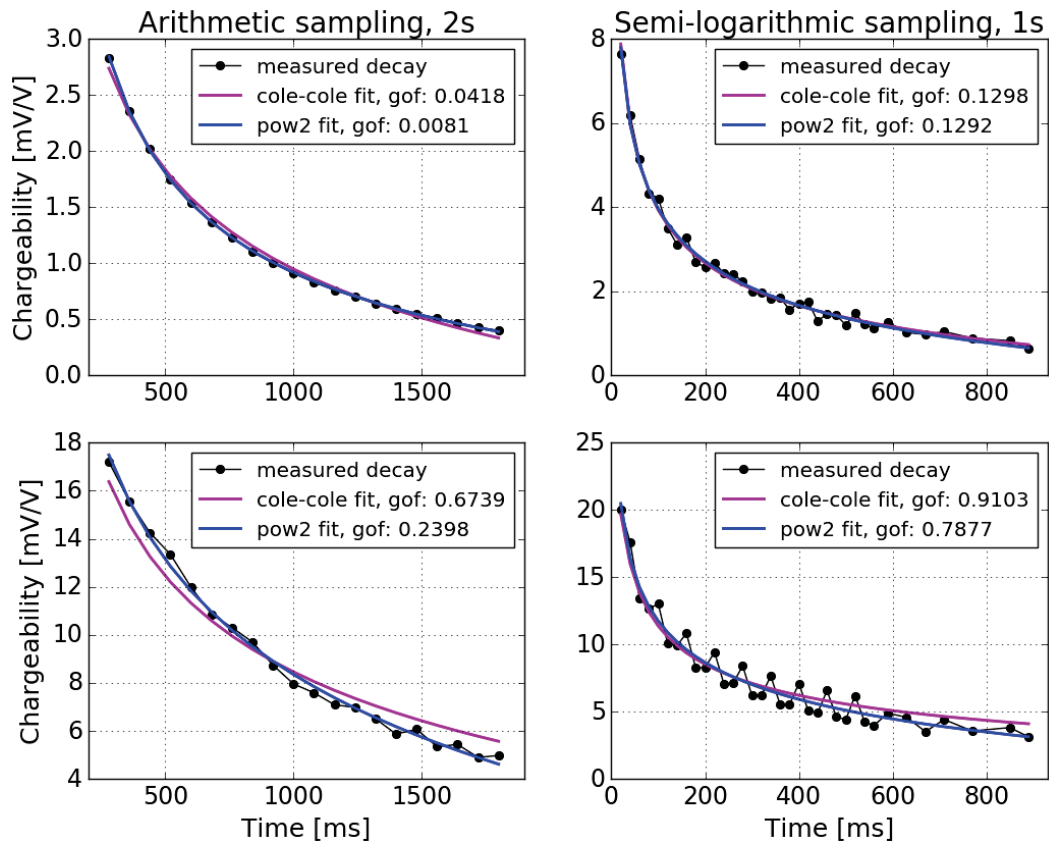


Figure 3.8: Fitted curves of the Cole-Cole model in comparison with the $pow2$ model. Visual analysis as well as the goodness of fit (gof) indicate a better approximation for the $pow2$ model.

and robust approach of fitting models based on the initial formulation after Pelton et al. (1978) was found. Fitted curves, based on the model formulation after Guptasarma (1982), when provided with proper starting values, proved to be able to fit most decay curves. However, a visual analysis as well as the goodness of fit showed that the $pow2$ model approximates the measured decay far better which is critical for further analysis. The gof values for fitted curves of the Cole-Cole and $pow2$ model can be found in table 3.4. Although not quantified here, the computational effort to fit the Cole-Cole model is not negligible and particularly relevant when fitting hundreds or thousands of curves of a data set. By means of a theoretical background the Cole-Cole model might be the best-suited model to approximate any decay curve. However, given the reasons here, it must be concluded that a robust and simple model, such as the $pow2$ model, is probably the better choice.

3.4 Evaluation of the sampling on the model fitting

		Goodness of fit	
Sampling	Case	Cole-Cole	<i>pow2</i>
Arithmetic	1	0.0418	0.0081
	2	0.6739	0.2398
Semi-log.	1	0.1298	0.1292
	2	0.9103	0.7877

Table 3.4: Values for the goodness of fit for fitted curves of the Cole-Cole and *pow2* model for two cases of decay curves obtained with an arithmetic and semi-logarithmic sampling.

3.4 Evaluation of the sampling on the model fitting

The evaluations in section 3.2 geared more towards a general description of the fitting of model curves to the measured decay and a deduction of a best-fitting model. Furthermore tests with decay curves obtained with different samplings of the voltage decay revealed consistent results in terms of the model fitting. However since the decay curves are from field data sets and the voltage decays are not known the "goodness of the approximation" of the fitted model curves to the actual voltage decay could not have been evaluated. Therefore a series of numerical tests were conducted aiming at the understanding of the representativeness of the fitted model curve and the effects of different samplings of the voltage decay on the model fitting. In particular the question of "is there a best sampling (i.e. the distribution, number and width of the IP gates) for the model fitting" should be answered.

Consistent to the approach in section 3.1 the voltage decay was modelled after a power law function and subsequently contaminated with different levels of gaussian noise with standard deviations of 50, 100, 500 mV representing different SNR. For each of the samplings in tables 3.2 and 3.5 the decay curves for the clean voltage decay as well as the contaminated decays were derived following the standard approach stated in section 2.1. To the four decay curves of each sampling type (one for the clean voltage and three for the contaminated voltage decays) the proposed power law (see section 3.2) was fitted. In order to have statistical parameters for the goodness of approximation the RMSD (see equation 3.4) between the fitted model and the decay curve for the clean voltage signal as well as the misfit ΔM_{int} of the integral chargeability values (see equation 2.3) of both curves were calculated. The equation for ΔM_{int} writes

$$\Delta M_{int} = M_{c,int} - M_{f,int} \quad (3.7)$$

with $M_{c,int}$ being the integral chargeability of the decay curve (clean voltage decay) and $M_{f,int}$ the integral chargeability of the fitted model curve.

Figure 3.9 shows the modelled voltage with the different noise levels (top panel) and the fit-

	Semi-logarithmic mod	Cole-cole	Test
Mdelay	160	20	50
Gate 1	40	20	50
Gate 2	40	30	50
Gate 3	40	30	120
Gate 4	40	30	50
Gate 5	40	40	120
Gate 6	50	40	50
Gate 7	50	50	120
Gate 8	50	60	50
Gate 9	50	70	120
Gate 10	50	80	50
Gate 11	90	90	120
Gate 12	90	100	50
Gate 13	90	110	120
Gate 14	90	120	50
Gate 15	90	130	120
Gate 16	120	140	50
Gate 17	120	150	120
Gate 18	120	160	50
Gate 19	240	180	120
Gate 20	240	200	50

Table 3.5: *Mdelay*, gate widths, gate numbers and their distribution for three different samplings. All values are given in ms.

ted model curves for different SNR (rows two to four). For the sake of clarity the six tested samplings respectively the corresponding model curves are distributed on two columns. As for the case of a high SNR all models approximate the decay curve of the clean voltage signal well with only small deviations being observed for the model curves of the left column. This visual analysis is also supported by the small values for the parameters of the RMSD and ΔM_{int} , e.g. for the arithmetic sampling $\text{RMSD} = 0.16$ and $\Delta M_{int} = 0.153$ mV/V. Also for decreasing SNR (third row of figure 3.9) the results are quite promising with a maximum deviation for the fit of a modified semi-logarithmic sampling of $\Delta M_{int} = 0.353$ mV/V. The mean value of all integral chargeability values $M_{c,int}$ is 2.823 mV/V (also see figure 3.9) and thus a deviation of 0.353 mV/V represents an error of approximately 9%. Regarding the model curves for the most distorted voltage decay (fourth row of figure 3.9) some observations can be made. Although the fitted model curves of the left column by no means approximate the undistorted decay curve, the difference of the integral chargeability values are small, in fact even lower as for the fitted model curves of the third row. This is an important observation because it means that ΔM_{int} alone is probably not enough to describe the goodness of approximation. Also the RMSD values need to be considered. Furthermore it seems that model curves fitted to decay curves obtained with samplings characterized by a small *Mdelay* and more narrow gates in the early times of

3.4 Evaluation of the sampling on the model fitting

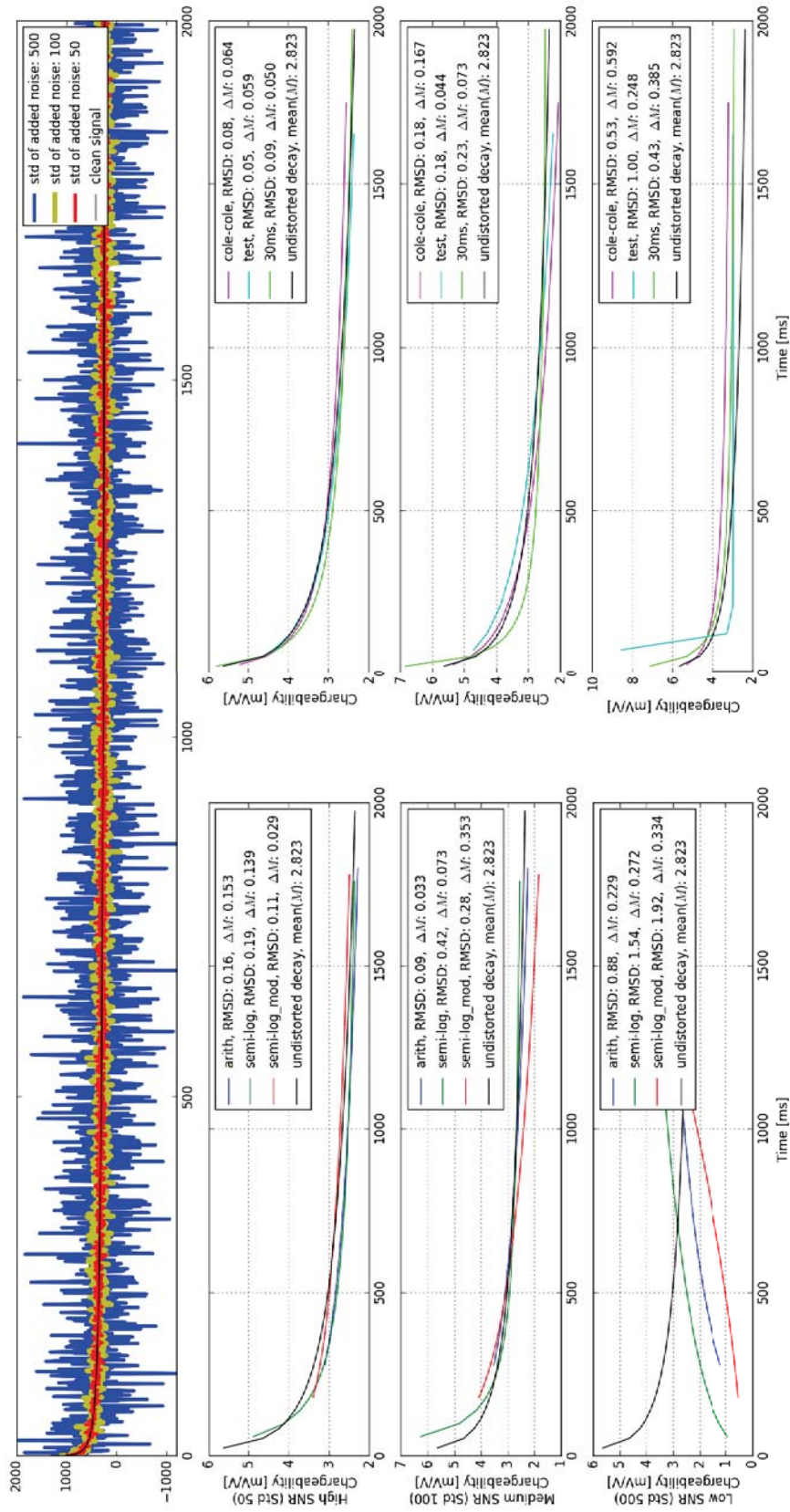


Figure 3.9: The effects of the sampling of the voltage decay on the fitting of a model curve. The first row shows the modelled voltage decay contaminated with different levels of noise and the rows two to four the fitted model curves for different samplings and noise levels.

the decay tend to approximate the undistorted decay far better. The maximum value of ΔM_{int} for the *Cole-cole* fit is 0.592 mV/V and represents an error of around 20% which is acceptable considering the high level of noise in the voltage decay. Except for the *test* fit also the RMSD values are relatively low with 0.53 mV/V for the *Cole-cole* and 0.43 mV/V for the *30ms* fit.

All observations and conclusions made for the results presented in figure 3.9 are however only valid for this one specific distribution of noise in the voltage decay. To evaluate the general performance of the individual samplings for the model fitting another experiment has been conducted. It consisted of repeating the setup as described above 100 times and a statistical analysis of the parameters ΔM_{int} and RMSD. Figure 3.10 shows the distributions of ΔM_{int} (upper panel) and the RMSD (bottom panel) plotted against M_{int} for low levels of noise (light colors), medium levels of noise (medium-dark colors) and high levels of noise (dark colors) as obtained for the different samplings and corresponding fitted model curves. The standard deviations presented in the legends of figure 3.10 are the values calculated for all 100 samples of the individual noise levels (starting with the value for the low noise case). Apparently, of all tested samplings, the *30ms* fit has the lowest values of ΔM_{int} and RMSD with both values being a factor 0.5 smaller than for the next best sampling (0.06 vs. 0.1 mV/V of the *test* fit for ΔM_{int} and 0.03 vs. 0.07 mV/V for the RMSD). This confirms the observations made before with a preference for samplings with a high number of narrow gates. On the opposite however, the other samplings with a small M_{delay} and dense sampling of the early times are not performing significantly better than the widely used *arithmetic* sampling and the standard deviations for the ΔM_{int} and RMSD values as well as the distributions observed in figure 3.10 are similar. That is unexpected, because following the conclusions from earlier, at least the RMSD values should show more variance for the *arithmetic* and the modified *semi-logarithmic* sampling. Two possible explanations are i) the experimental setup is insufficient and a sole visual analysis of the fitted curves is needed or ii) the distribution and width of sampling is of less importance for the model fitting.

To summarize this section in the following the general conclusions of this experiments:

- In section 3.1 the effects of random noise as well as the sampling of the voltage decay were evaluated concluding that for random noise with a standard deviation of 500 the decay curves become erroneous and an approximation to the undistorted decay is hardly given. However, following the observations made here, it is clear that the fitted model curves are able to reproduce the shape of the undistorted decay to a certain degree, despite the erroneous decay curves as the input parameter.
- The goodness of approximation is difficult to quantify. The values for the ΔM_{int} and RMSD might not be sufficient and probably demand an additional visual analysis of the fitted curves.

3.4 Evaluation of the sampling on the model fitting

- It seems that the number of gates is the dominating factor for the model fitting. Whereas only small differences can be observed for the samplings with 20 IP gates the statistical indicators (i.e. the standard deviations for ΔM_{int} and RMSD) for fitted model curves of the sampling with 66 gates were much lower. However please be aware that this statement might be compromised by the insufficient quantification of the goodness of approximation as described above.

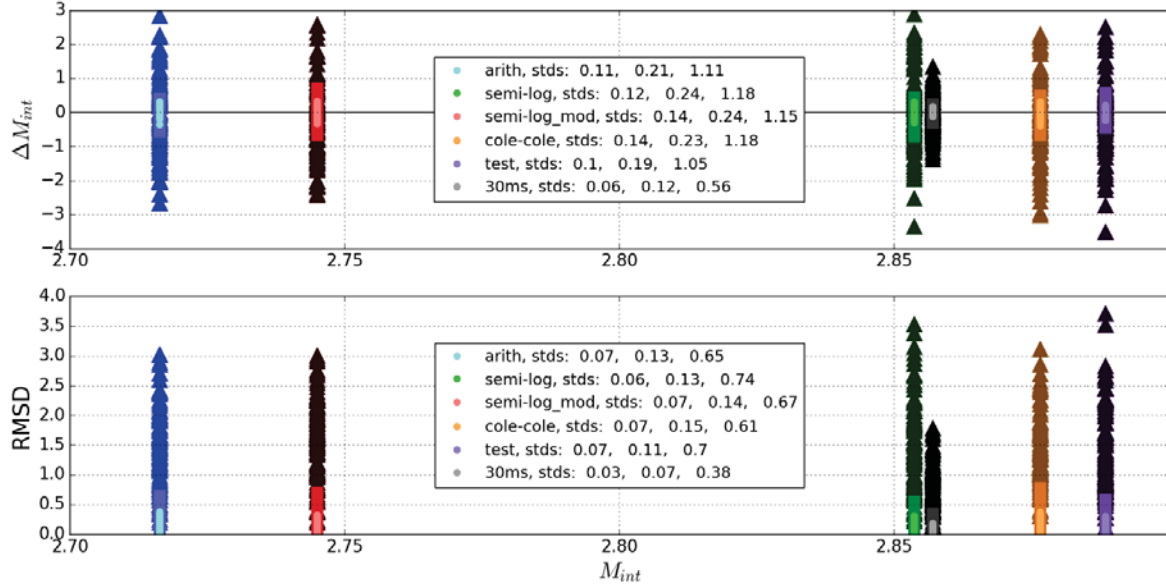


Figure 3.10: The general performance of the samplings on the model fitting was evaluated by calculating ΔM_{int} and RMSD for 100 different distributions of random noise in the voltage decay for the three particular noise levels. Light colors and circle markers correspond to the added noise with a standard deviation of 50, medium-dark colors and square markers to standard deviations of 100 and dark colors and triangle markers to standard deviations of 500. The standard deviations in the legends are computed for all 100 values for each noise level starting with the lowest one.

Chapter 4

Histogram Analysis

The identification and removal of outliers could be performed by setting thresholds for the measured electrical values, e.g. the apparent resistivity ρ_a , the transfer resistance R or the integral chargeability M_{int} . Filtering schemes following this approach are fully automatable, therefore being applicable to extensive data sets. However the definition of appropriate thresholds can be arbitrary and is mostly based on subjective observations. Only under rare circumstances, for example with data being normally distributed, threshold values can be defined with a proper statistical background.

The following example should illustrate some problems typically related to the characterization of outliers based on the thresholds in the histogram. Let it be assumed that 90% of a data set's apparent resistivity values are valid measurements and follow a normal distribution (blue bins in figure 4.1), 7% are outliers by means of not being part of the normal distribution (green bins in figure 4.1) and 3% of the values are being associated to outliers without spatial correlation within the data set (red bins in figure 4.1). This spatially inconsistent outliers are however in the range of magnitude of the values of the normal distribution. For normally distributed data, the interval $\pm 2\sigma$, with σ being the distribution's standard deviation, contains 95.45% of all values of the normal distribution. Therefore a first approach for the definition of a threshold could consist of two or three times the distributions standard deviation as values exceeding those thresholds are probably not part of the normal distribution.

Now, some observations can be made:

- Based on the threshold, outliers not associated to the normal distribution can be classified and removed. However, also valid measurements are being rejected. Therefore the threshold may be justified by a statistical point of view, yet may not be fully optimal.
- Outliers characterized by a lack of spatial correlation within the data set, however characterized by values within the same range of values as the valid measurements cannot be classified with simple thresholds of the electrical values. Other approaches are needed.

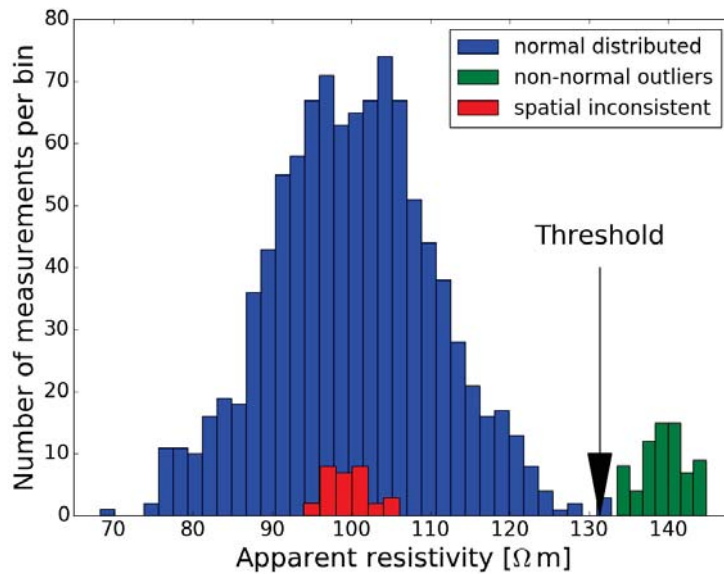


Figure 4.1: *The threshold identifies and filters non-normal outliers not associated with the valid measurements of the normal distribution. However also valid measurements are being identified as outliers. Furthermore, spatial inconsistent outliers with magnitudes within the range of valid measurements cannot be assessed using this filtering approach.*

- Even though this is a fictitious example with ideal distributions of measurements and outliers, the estimated threshold is not optimal. Generally, under normal conditions, ideal normal distributions are a rare exception and measured data distributions differ from well-known statistical models. This raises the questions whether appropriate thresholds can be defined based on statistical analysis such as the standard deviation or percentiles or if optimal thresholds can only be deduced by a visual analysis of the measured data's distributions respectively a-priori information on the data (e.g. apparent resistivity values are only expected up to 130 Ωm). This again, confines the application of this approach in automated filtering schemes.
- There is no possibility to quantify the amount of random noise based on the threshold approach as needed for the application during the inversion.

In order to account for some of the above mentioned deficiencies another approach has been developed. The so-called *histogram analysis* relies on the background that histograms of the integral chargeability values of clean data sets are typically characterized by a high degree of connectivity between the individual bins (e.g. refer to figure 4.2 a). Therefore can discontinuities or gaps (i.e. empty bins or bins with a low number of counts) indicate the presence of outliers. However only under the assumption that the histogram was computed for a representative number of bins. As discussed before can outliers for example be related to measurements

without spatial correlation within the data set or to anomalously high integral chargeability values. For the latter type of outliers the histograms commonly reveal patterns similar to figure 4.2 b), where additionally to a main distribution, separated clusters of bins with only a limited number of counts are present. The main distribution corresponds to the valid measurements, whereas the clusters are associated to outliers. The assumption that outliers are clustered apart from the main distribution (without direct connection) is the key premise of this methodology. The histogram analysis/filter searches the histogram for possible gaps and removes those measurements associated to minimal counts and separated bins.

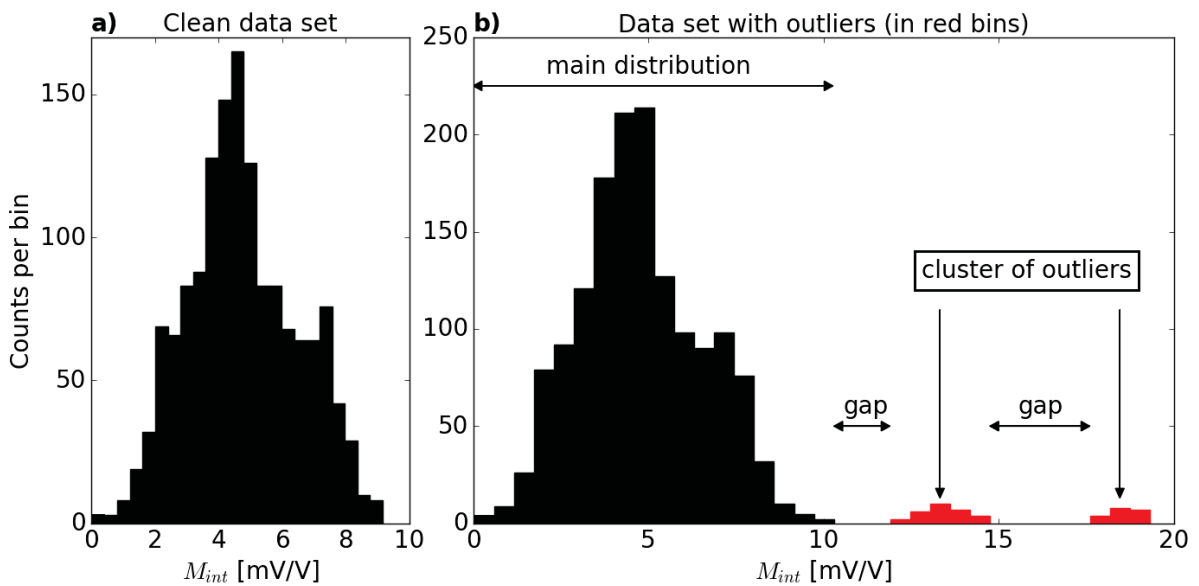


Figure 4.2: a) presents a histogram typical for a clean data set without the occurrence of gaps between bins. The histogram presented in b) is based on a data set with outliers characterized by anomalously high integral chargeability values (measurements in red bins). Large gaps (i.e. empty bins) are considered as an indication of outliers.

Subsequently the general design of the histogram filter will be illustrated. Details on particular parameters of the filter will be discussed later on. Figure 4.3 presents a block chart of the work flow. As a first step the number of bins n_b for the histogram is defined and the histogram is computed. The second step consists of a loop iterating over the individual bins starting with the bin with the lowest chargeability values. A bin is then classified as gap if the counts per bin (i.e. the number of measurements in the bin) is lower than a freely selectable threshold t_g . If no gaps can be identified it is assumed that the data set is free of outliers and the analysis stops. Bins classified as gaps can be subject to a set of optional queries, here denoted as *secondary conditions*. If the secondary conditions are not fulfilled the loop continues with the next iteration. For the other case an integral chargeability in the bin, typically realized as the

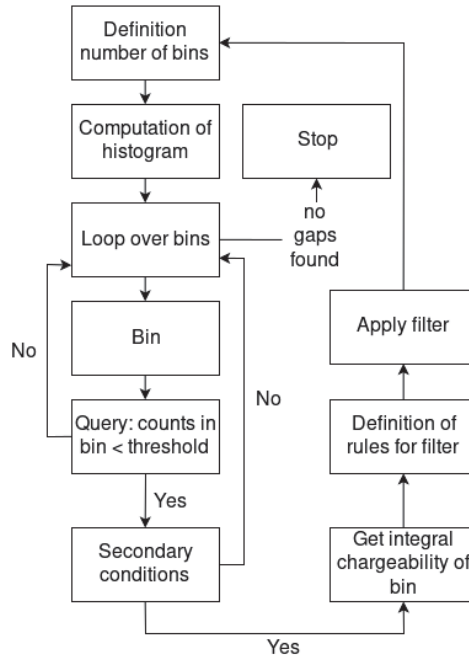


Figure 4.3: Schematic block chart of the histogram analysis.

integral chargeability value associated to the left boundary of the bin, is selected. The value is subsequently used to define rules for a filter (e.g. remove all measurements exceeding this threshold). After the application of the filter the next iteration of the histogram analysis starts. However this time the updated (filtered) data set is used for the definition of n_b . The number of iterations n_i of the histogram analysis can be chosen freely. Nevertheless, a large number of iterations may lead to the removal of data of spatially constrained anomalies that are not necessarily outliers.

The selection of an adequate number of bins is critical. Histograms calculated for a large number of bins are typically characterized by the appearance of many thin separated bins and applying the filter can result in the removal of measurements that are not outliers (e.g. the data set is overfiltered). A low number of bins leads to histograms with very broad bins and outliers, even if they may be well-separated from the main distribution, might be grouped in the same bin as valid measurements and therefore only a poor identification of outliers is given (e.g. the data set is underfiltered). To better illustrate the problem, figure 4.4 presents the histograms and filter thresholds (blue lines) for three iterations n_i and different parameterizations of n_b . The rules for the calculation of n_b are presented in table 4.1. n_b used in the first row of figure 4.4 corresponds to a value determined by an empirically deduced equation, for the second row n_b was defined as a fifth of the number of measurements of the data set and for the third row n_b is a function of the integral chargeability values of the data set. Based on a visual analysis of the histogram and the corresponding pseudosection an optimal threshold for outliers was

	Rule
Row 1	$n_b = 1 + 4.5 \cdot \log(n)$, n ...number of measurements
Row 2	$n_b = n/5$
Row 3	$n_b = \max(M) \cdot 1.25$, M ...array of integral chargeability values

Table 4.1: *Three different rules for the calculation of n_b were investigated with two of them being a function of the number of measurements n and one as a function of the associated integral chargeability values of the data set (Row 3).*

defined denoted by the red line in figure 4.4. t_g was chosen with 1 (i.e. a gap is defined as an empty bin) and a secondary condition was introduced consisting of a check whether the integral chargeability of the bin is higher than the median value of integral chargeability values of the data set.

Results for the first row reveal that the outliers are well separated from the main distribution and the corresponding gaps can be easily detected. Already after the second iteration all outliers are removed. Since there are no gaps left the third iteration stops without a loss of valid measurements. Quite obviously the second row represents the case of a number of bins chosen too high. Particularly for the second iteration, where the filter threshold is based on a single gap within the valid measurements resulting from to the inadequately defined number of bins, a significant amount of valid measurements is removed. The same applies for the third iteration. For the third row, the parameterization based on the integral chargeability values leads to an underestimation of the number of bins and although starting with a number of bins close to values of the first row, the values for n_b in the second and third iteration will not lead to a removal of remaining outliers.

The proposed histogram analysis can also be used to investigate the distributions of other parameters as for example the normal-reciprocal misfits or parameters determined in an analysis of the spatial consistency. However it may be necessary to adapt the filter parameters and particularly for such applications it has shown that the choice of the threshold value t_g used for the classification of a gap is not necessarily confined to the value of 1. The before mentioned secondary conditions are thought to imply additionally constraints to the data values associated to the as gap classified bin and are often of empirical nature and based on subjective observations. The secondary condition introduced for the example before, consisted of only allowing gaps associated to integral chargeability values higher than the median value of the data set. Gaps in the vicinity of the median value, which for normal conditions is located at the peak of the main distribution, would result in a drastic removal of valid measurements. Other secondary conditions could consist of percentiles or median values with added standard deviations.

Outliers can also be related to measurements with anomalously low integral chargeability

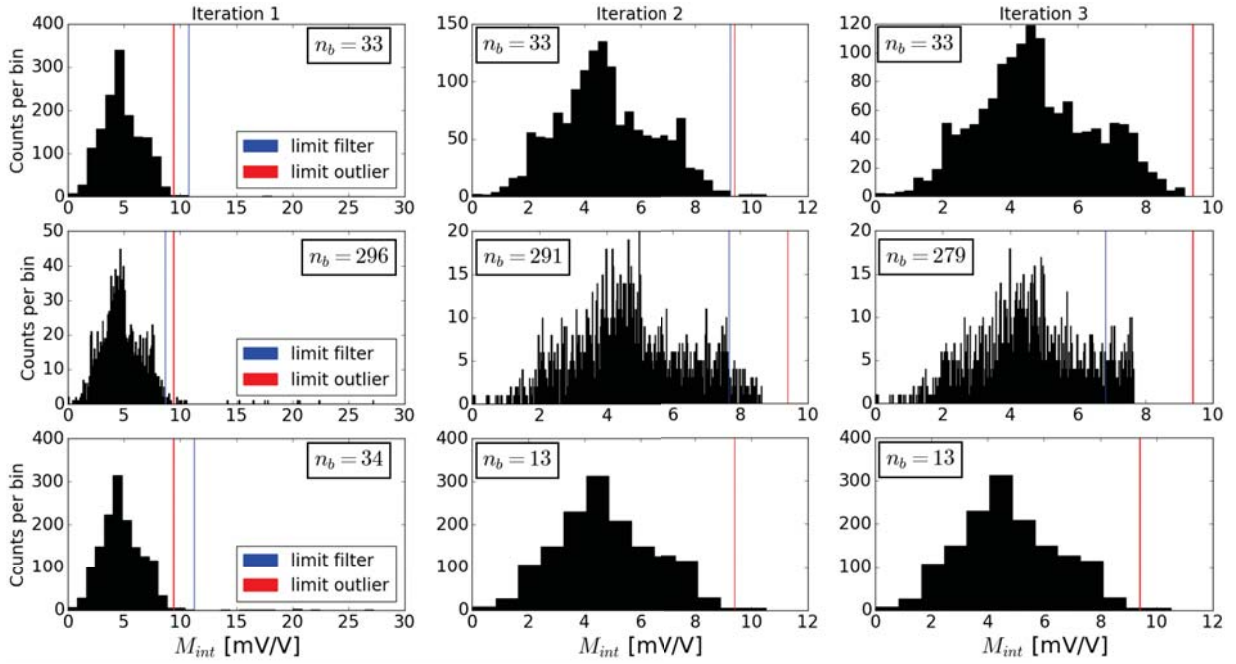


Figure 4.4: Histograms and defined filter thresholds (blue lines) of the histogram analysis for three iterations and different parameterizations of the number of bins n_b (c.f. table 4.1). The red line indicates the optimal threshold for outliers determined by an visual analysis of the histogram and the corresponding pseudosection of the data set.

values without connection to the main distribution. By adapting the direction in which the histogram bins are iterated over (i.e. starting with the rightmost bin, e.g. the bin with the highest integral chargeability value) such outliers can also be removed. Clearly a change of direction also requires the adjustment of possible secondary conditions.

Chapter 5

Analysis of the Spatial Consistency

Spatial consistency is a key parameter of clean data sets (e.g. free of outliers). For electrical measurements, such as the IP method, the measured parameters are expected to vary smoothly and sharp contrast between neighboring measurements could indicate systematic errors needed to be removed prior inversion. Figure 5.1 presents an integral chargeability pseudosection before and after an analysis of the spatial consistency (and the corresponding filtering). The unfiltered data set is characterized by measurements contaminated by systematic errors (dark red points in the pseudosection in figure 5.1 with $M_{int} > 15$ mV/V). Outliers like this don't have any connection to the surrounding measurements in the pseudosection and the removal of such outliers improves the integrity in the data and allows to solve for images with higher contrast. To

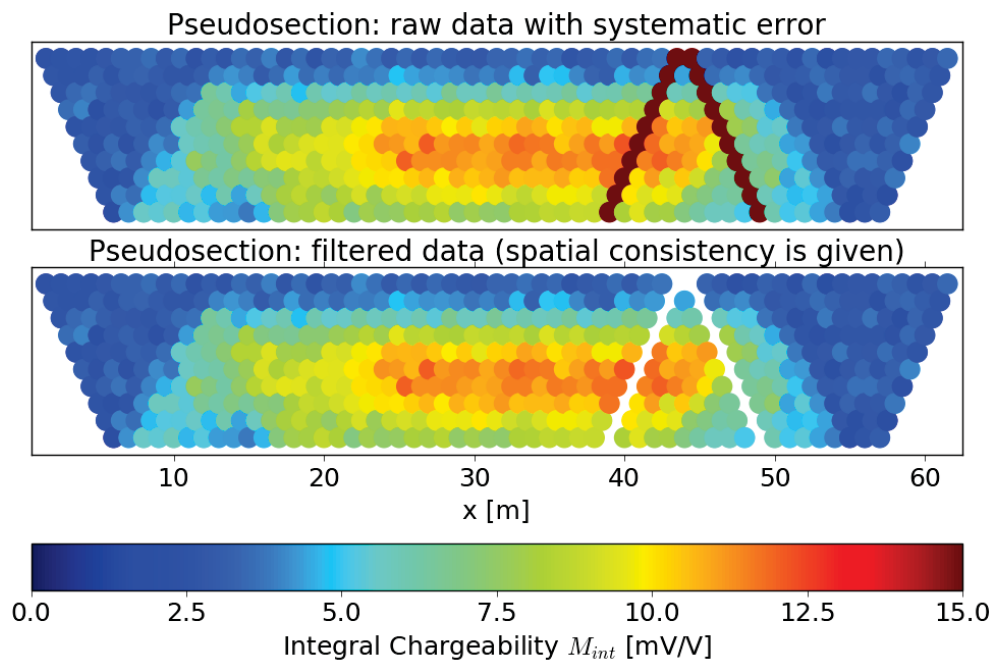


Figure 5.1: Pseudosections of integral chargeability data before and after filtering with a spatial consistency based approach.

be practical, data filtering approaches based on an analysis of the spatial consistency need to take into account more than one measurement at a time. This can be easily illustrated on the following example. A smooth decay curve, which is characterized by a high goodness of fit (see section 3.2) can however be situated in the wrong range of magnitude. There is probably neither a correlation in the integral chargeability values nor in the characteristics of the shape of the decay curve in regard to the neighboring measurements. However, without taking into account either a-priori information (i.e. integral chargeability values exceeding 10 mV/V are not being expected) or other measurements for comparison, there will be no possibility to characterize the decay curve as an outlier.

The proposed approach for the analysis of the spatial consistency applied in the DCA is realized as a comparison of a reference decay curve with either the measured or the fitted decay curve. The reference curves should be representative for a subset of decay curves and the spatial inconsistency can be characterized by means of i) a deviation from the shape of the reference curve and ii) a deviation from the magnitude of the reference curve. Understandingly, both deviations are in most cases coupled.

The following sections discuss the:

Computation of reference curves: Reference curves need to be as smooth as possible to avoid biasing deviation estimates. Furthermore, the computation needs to be robust, by means of an independence to erroneous curves and the reference curve needs to represent the characteristics of the decay curves used for the computation.

Partitioning of data sets: The proper choice of subsets for the computation of the reference curve is critical. Subsets can be defined on characteristics of the decay curves but also on general properties of measurements such as the electrode configurations or the number of depth levels in the pseudosection.

Analysis of the spatial consistency - the reference curve approach: A detailed description of the analysis approach.

Characterization of outliers: To be of use, the deviation parameters derived during the analysis of the spatial consistency need to be capable of characterizing outliers. This section will discuss deviation parameters obtained for different realizations of the reference curves.

Definition of parameter thresholds: Finally different approaches to define parameter thresholds as needed for the filtering will be discussed.

5.1 Computation of reference curves

Reference curves (RCs) need be representative for the given subset of either measured decay curves (MDCs) or fitted decay curves (FDCs). In order to avoid biasing during the comparison reference curves further require to be as smooth as possible. Therefore, in a first step, non-decaying curves are not taken into account for the computation of a reference curve. Equations 5.1a-e show five different computation approaches which in the following should be evaluated.

$$\text{mean(MDC)} : m_{r,i} = \text{mean}([m_{m,i}, m_{m,i+1}, \dots, m_{m,N}]) \quad (5.1a)$$

$$\text{median(MDC)} : m_{r,i} = \text{median}([m_{m,i}, m_{m,i+1}, \dots, m_{m,N}]) \quad (5.1b)$$

$$\text{median(FDC)} : m_{r,i} = \text{median}([m_{f,i}, m_{f,i+1}, \dots, m_{f,N}]) \quad (5.1c)$$

$$\text{weighted average(MDC)} : m_{r,i} = \frac{\sum_{j=1}^N (w_j \cdot m_{m,i,j})}{\sum_{j=1}^N w_j} \quad (5.1d)$$

$$\text{weighted average(FDC)} : m_{r,i} = \frac{\sum_{j=1}^N (w_j \cdot m_{f,i,j})}{\sum_{j=1}^N w_j} \quad (5.1e)$$

$$\text{with : } w_j = \left[\text{RMSD}_j \cdot \max \left(\frac{1}{[\text{RMSD}_j, \text{RMSD}_{j+1}, \dots, \text{RMSD}_N]} \right) \right]^{-1} \quad (5.1f)$$

$m_{r,i}$ is the calculated partial chargeability for the reference curve, $m_{m,i}$ the measured partial chargeability and $m_{f,i}$ the partial chargeability of the fitted curve, all for the i -th gate. N is the number of decay curves of the given subset. w_j is a weighting factor realized as the normalized inverse of the individual RMSD for each MDC/FDC pair (as introduced in equation 3.4). Noisy decay curves are therefore being assigned to lower weights than smooth decay curves. Hence, defining the weighting factors like this, further favors smooth reference curves.

Figure 5.2 presents the calculated reference curves as well as the MDCs and FDCs for the case of a high SNR (left panel) and low SNR (right panel). The subset of decay curves for the high SNR case is characterized by a majority of smooth curves with only a few curves showing erroneous behavior. Apparently all five proposed computation approaches provide smooth reference curves which are further representative for the subset. Only minor differences can be observed and even the rather non-robust approach of calculating the mean value of each gate of the MDCs (see equation 5.1a) is performing satisfyingly.

However, as presented in the right panel of figure 5.2, with increasing number of noisy decay curves the approaches of calculating the mean/median value of the MDCs (equations 5.1a, 5.1b) seem to reach a breaking point. The calculated RCs are no longer smooth and also the magnitude of the mean calculation is overestimated and not representative. This is due to the two high magnitude decay curves and highlights the non-robust behavior of a mean calculation

in presence of outliers (which, for the given subset, the two decay curves obviously are). The weighting average (both based on the FDCs and MDCs) and the median calculation for the FDCs provide smooth RCs in the similar range of magnitude. They can be considered as representative for the subset and it appears that the weighting significantly reduces the influence of noisy decay curves - even for the MDC case.

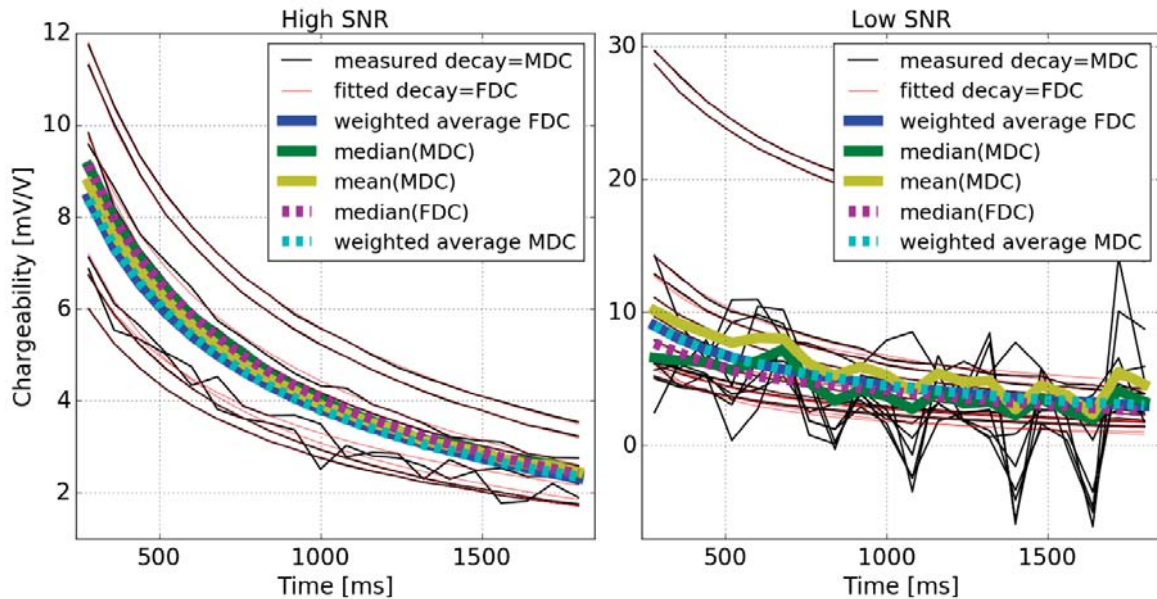


Figure 5.2: Different realizations of the computed reference curve for the case of a high SNR subset (left panel) and a low SNR subset (right panel) of decay curves.

To further validate whether the above observations, regarding the smoothness of the RCs, are only applicable to this given subset a series of tests have been conducted. From two data sets, characterized by different SNR (high and low), N random sized subsets of decay curves were drawn and the RCs calculated (non-decaying curves were removed before). The smoothness of each calculated RC was evaluated by means of its gof respectively RMSD when fitting a $pow2$ model. Smooth RCs should be characterized by low gof values whereas noisy realizations show higher values. Finally, the general estimation of smoothness was evaluated as the standard deviation of all of the N gof values. This was done for each computation approach separately.

Table 5.1 shows the number of subsets for each data set and the corresponding calculated standard deviations. The calculation based on the weighted average of the FDCs has the lowest value for both data sets with standard deviations being a factor 10 to 1000 smaller than for other calculations. Even the approaches of weighted average of the MDCs and median of the FDCs, which appeared to perform comparable as can be seen in figure 5.2, are associated to much higher standard deviations. It is further interesting, that the different SNR of the data

sets is directly being reflected by the estimated standard deviations. In summary it is fair to conclude that the computation approach based on the weighted averaging of the fitted curve's partial chargeability values (as written in equation 5.1e) represents the most robust methodology to calculate smooth reference curves.

Computation approach	Data set 1 - high SNR	Data set 2 - low SNR
	Subsets: $N = 164$	Subsets: $N = 65$
	Standard deviation	Standard deviation
Mean(MDC)	0.1532	0.9252
Median(MDC)	0.0795	0.2314
Median(FDC)	0.0277	0.0204
Weighted average(MDC)	0.0031	0.0369
Weighted average(FDC)	0.0002	0.0037

Table 5.1: Results of the evaluation of smoothness of the RCs for the different computation approaches.

5.2 Partitioning of data sets

The partitioning of data sets, i.e. the definition of appropriate subsets for the computation of the reference curve, is not trivial. The reference curve should be representative for the subsets and thus the number of decay curves, however also the quality of corresponding the decay curves need to be selected properly. Partitioning the data set in too many subsets might results in reference curves not able to characterize outliers, as they might even be defined for outliers themselves. Considering the opposite case of just a few subsets defined, the dynamic in the decay curves may be too large to permit a proper identification of outliers. Moreover even valid measurements with low and high integral chargeability values might be classified as outliers (as it will be later discussed in section 5.4).

To better illustrate the problem figure 5.3 presents the subsets (blue) and reference curves (black) for a given data set for the case of too few reference curves (left panel) and too many reference curves (right panel). FDCs in red color indicate the classified outliers following the reference curve approach. To set it in a relation it is assumed that decay curves exceeding an average magnitude of about 10 mV/V can be seen as outliers. The limit is indicated by the dashed green curve. Whereas only a few measurements are being classified for the case of too many reference curves, the classification based on only one reference curve would lead to drastic removal of measurements during the filtering.

As it can be seen in figure 5.3, the reference curves require to describe the characteristics of valid measurements. For reference curves defined on a subset of outliers the derived deviations

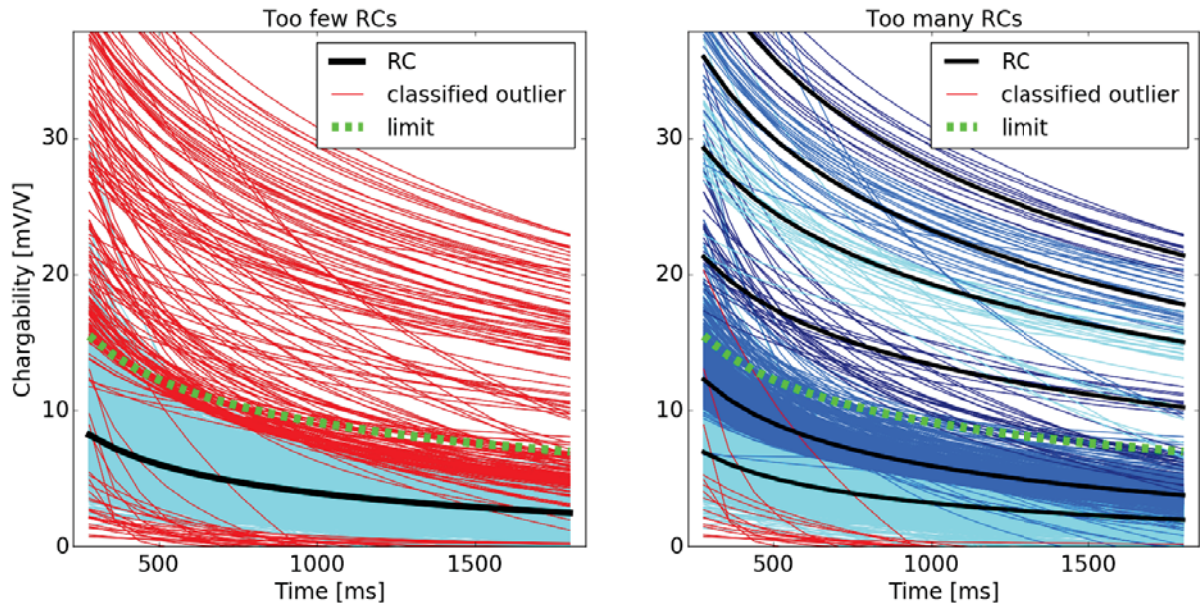


Figure 5.3: Comparison of classified outliers (red lines) for the case of too few reference curves (left panel) and too many reference curves (right panel). The dashed green line is the assumed limit for outliers and the blue decay curves indicate the subsets used for the computation of the reference curves.

parameters will be very small and thus the outliers won't be removed in the filtering procedure. This marks a limitation of this data set partitioning approach as an adequate prefiltering is required in order to define the reference curves on the valid measurements. In fact, the most representative reference curves would be defined for clean data sets. However, since clean data sets represent the desired outcome of such analysis, circular reasoning applies here. Alternatively, subsets can be defined based on the characteristics of the survey, i.e. the geometrical factors, potential dipoles belonging to the common current dipole or measurements of the same depth level of the pseudo section. Such approaches cluster the measurements in a different manner and require, compared to the partitioning discussed above, a less sophisticated prefiltering of the data beforehand.

The following sections are intended to introduce different realizations of data partitioning with a distinction between approaches based on the integral chargeability and approaches taking into account the electrode configuration (i.e. the geometry used for current injection and voltage readings).

Uniform partitioning - binning in uniform subsets: As a first approach the integral chargeability values of a prefiltered data set (after the removal of non-decaying curves and decay curves with implausible high integral chargeability values) were divided into uniform subsets. For the definition of subsets the range of integral chargeability values was calculated

and used to formulate the boundaries of the subsets by dividing it into three equal parts. The choice of three subsets is empirical and might need to be adjusted for particular data sets. For the present data sets it is however an acceptable compromise, when keeping in mind the trade-off between too many and too few subsets. The boundary definition for the uniform partitioning can be found in table 5.2.

$$\text{range}(M_{int}) = \max(M_{int}) - \min(M_{int})$$

$$\text{third} = \text{range} / 3$$

Subset 1	$\min(M_{int})$	$\min(M_{int}) + \text{third}$
Subset 2	$\min(M_{int}) + \text{third}$	$\min(M_{int}) + \text{third} * 2$
Subset 3	$\min(M_{int}) + \text{third} * 2$	$\max(M_{int})$

Table 5.2: Formulation of the range and the subsets for the case of a uniform partitioning. Here, M_{int} denotes an array containing the integral chargeability values of the prefiltered data set.

Focused partitioning - histogram analysis for focused bins: Analogous to the uniform partitioning, is the focused approach based on the integral chargeability values. However contrary to before, are the subsets in this case defined by the distribution of values in the histogram. In particular, relative minima of the binned integral chargeability values are sought and later on used for the definition of subset boundaries. It is clear that the occurrence and number of such minima is to a large part dependent on the number of bins in the histogram. For the present data sets, the formulation already presented in table 4.1 was used (with n being the number measurements). It writes

$$n_b = 1 + 4.5 \cdot \log(n) \quad (5.2)$$

The detection of the relative minima was performed using a standard function of the Scipy stack (Jones et al., 2001–; Du et al., 2006). It allows to choose the number of values on each side to use for the comparison with the value currently being tested. The intent is to solve for three subsets again. Thus the number is varied until at least three minima are found. For the case that only two, one or no relative minima or minimum can be located the approach degenerates to a uniform partitioning. For the case of three or more minima there is further a differentiation consisting of a check whether the first minimum is closely located to zero (i) or not (ii). The boundary definitions for (i) and (ii) can be found in table 5.3 and 5.4. The minima in the number of integral chargeability values per bin b_i are therefore being transferred to the position along the chargeability values $M_{int}(b_i)$ as the left bound of the corresponding bin (figure 5.4). As can be seen in the tables 5.3 and 5.4, only the first two to three minima are taken into account for the boundary definition. Minima in the higher range of integral chargeability values, which are typically relatively small compared to the first two to three minima, are merged into one subset.

$b_i \dots$ relative minima		
$M_{int}(b_i) \dots$ corresponding chargeability		
(i) $M_{int}(b_1)$ close to zero		
Subset 1	0	$M_{int}(b_2)$
Subset 2	$M_{int}(b_2)$	$M_{int}(b_3)$
Subset 3	$M_{int}(b_3)$	$\max(M_{int})$

Table 5.3: Definition of the boundaries for the focused partitioning when $M_{int}(b_1)$ is close to zero. Here, M_{int} denotes an array containing the integral chargeability values of the prefiltered data set.

$b_i \dots$ relative minima		
$M_{int}(b_i) \dots$ corresponding chargeability		
(ii) $M_{int}(b_1)$ not close to zero		
Subset 1	0	$M_{int}(b_1)$
Subset 2	$M_{int}(b_1)$	$M_{int}(b_2)$
Subset 3	$M_{int}(b_2)$	$\max(M_{int})$

Table 5.4: Definition of the boundaries for the focused partitioning when $M_{int}(b_1)$ is not close to zero. Here, M_{int} denotes an array containing the integral chargeability values of the prefiltered data set.

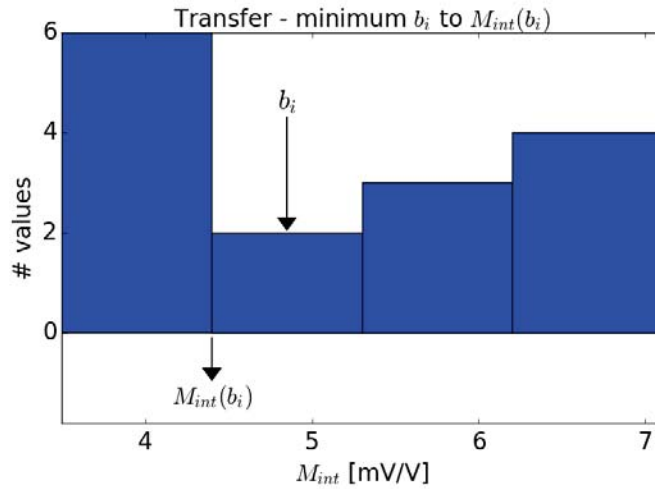


Figure 5.4: The computed relative minima b_i refer to the number of values per bin. For the partitioning (based on the integral chargeability values) the left bound of the corresponding bin, here denoted as $M_{int}(b_i)$, is used.

Figure 5.5 presents the reference curves (black lines), subsets (blue lines) and histograms indicating the boundaries for the subsets for the uniform partitioning (top panels) and focused partitioning (bottom panels). The blue decay curves shown here are the fitted decay curves. Although the first subsets are different the computed reference curves are

similar. The reason for that is the number of measurements in this particular subset and the robust formulation of the reference curve. When looking at the histogram it is logical that the reference curve will be centered in the distributions maximum, regardless of the change in the right bound of the subset. Major differences can however be observed for the reference curves of the subsets two and three. Whereas the focused partitioning provides reference curves describing the higher magnitude decay curves appropriately, the uniform partitioning obviously underestimates the influence of such measurements.

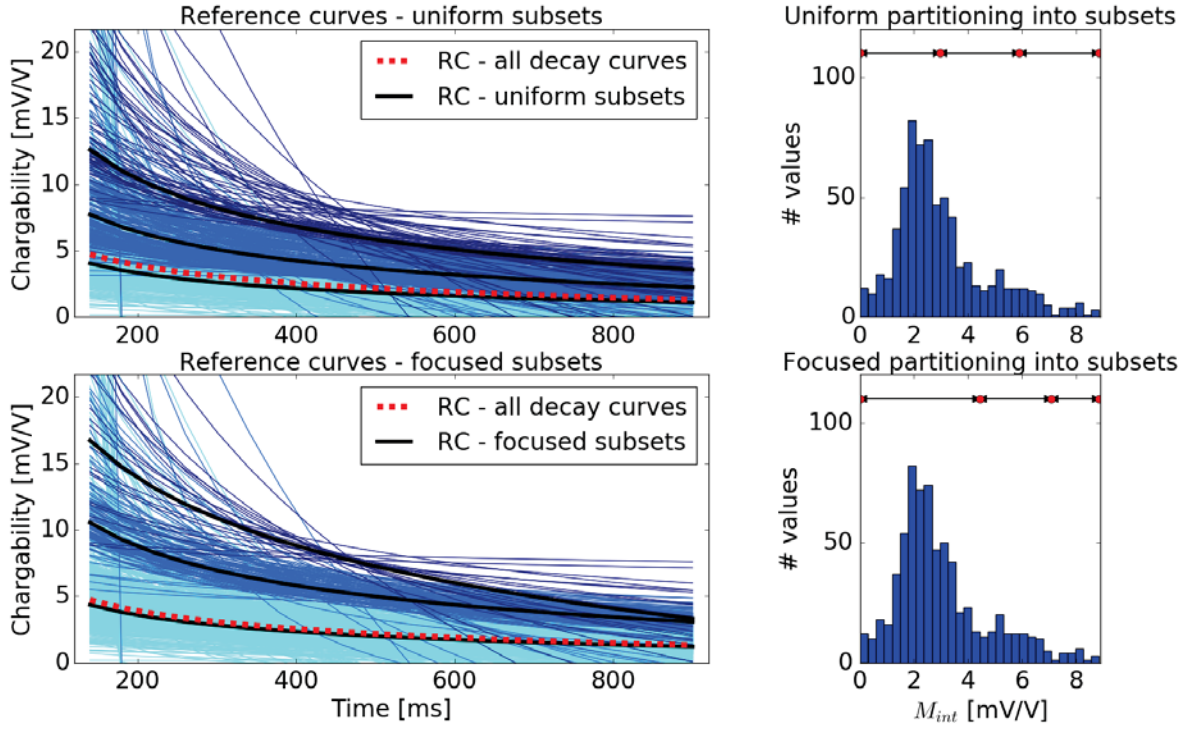


Figure 5.5: Computed reference curves (black lines), fitted decay curves of the subsets (blue lines), and the corresponding histograms indicating the boundaries of the subsets for the cases of a uniform partitioning (top panels) and the focused partitioning (bottom panels).

Current dipole partitioning - subsets for measurements sharing the current dipole: The current dipole partitioning is the first representative of the data partitioning approaches based on the electrode configuration and clusters measurements differently when compared to the approaches introduced before. Subsets are defined for measurements for which the potential dipoles are sharing the same current dipole. The number of reference curves is therefore not limited to the empirical value of three and is solely based on the characteristics of the deployed measurement configuration (i.e. the sequence of electrodes being addressed). Further, measurements within a subset are related to the same current density and thus fairly similar signal strengths and subsets should moreover cluster measurements

of similar SNR, when compared among each other. Table 5.5 shows the definition of two subsets for an exemplary DD data set. As can be seen, measurements of a subset typically span a range of different SNR due to the increasing separation between the current and potential dipole.

	Current electrodes		Potential electrodes	
	A	B	M	N
Subset 1	2	1	3	4
	2	1	4	5
	2	1	5	6
	2	1	6	7
Subset 2	7	6	8	9
	7	6	9	10
	7	6	10	11
	7	6	11	12

Table 5.5: Exemplary definition of subsets, following the current dipole partitioning approach for a Dipole-Dipole data set. A, B are the current electrodes and M, N are the potential electrodes.

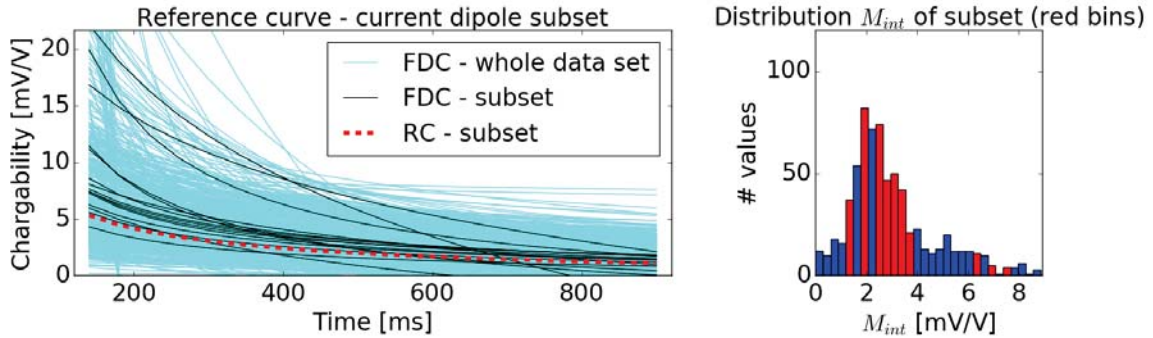


Figure 5.6: The fitted decay curves (black lines) and computed reference curve (dashed red line) for a subset based on the current dipole partitioning. The red bins in the histogram in the right panel indicate bins containing the integral chargeability values of the subset.

Figure 5.6 shows the fitted decay curves of a subset (black lines), the computed reference curve (dashed red line) and for comparison all fitted decay curves of the data set (light blue lines). The FDCs of the subset, when compared with a subset of the uniform partitioning approach, span a wider range of magnitudes and different shapes. This marks a major difference between the two approaches. The computed reference curve however, is similar to the one computed for all measurements (when compared with figure 5.5). The variety of measurements in the subset is also visible in the integral chargeability values, presented in the right panel of figure 5.5 where the distribution of integral chargeability values of the subset is indicated by the red bins. Blue bins refer to the distribution of integral

chargeability values of the entire data set.

Partitioning on the levels of the pseudosection: Another approach of partitioning the data set based on the electrode configuration is the definition of subsets for each depth level of the pseudosection. The plotting depth respectively (pseudo)-depth, which isn't necessary representative for the real distribution of electrical properties in the subsurface, is dependent on the electrode configuration and the separation between electrodes (as discussed in section 2.6). Since the topography is commonly not taken into account for the simple visualization of data in pseudosections, several measurements refer to the same depth and thus can be clustered (see red and black rectangle in figure 5.7). It is important to point out that the number of measurements as well as the SNR typically decrease with increasing depth. Hence, depth level partitioning groups measurements of similar signal strength. The subsets among each other however, considered in terms of the general SNR, are in fact not comparable. Depth level partitioning doesn't consider changes in the signal strength due to variations in the electrical properties. This may however be an important problem particularly for long profiles.

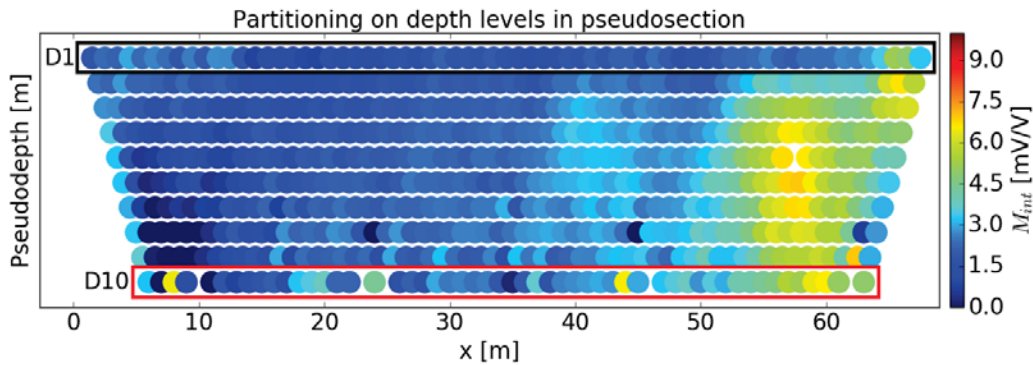


Figure 5.7: Measurements plotted to the same depth level can be grouped into subsets. The red and black rectangles indicate the measurements of the subset D1 and D10. Deeper depth levels are associated to lower SNR.

The fitted decay curves (black lines) and reference curves (dashed red lines) for the subsets D1 and D10, where D1 and D10 refer to different depths in the pseudosection, are presented in figure 5.8. The blue lines indicate the fitted decay curves of the entire data set. Again, the reference curves are in a similar magnitude as for the case of a single bin (i.e. no partitioning into subsets) and the histogram for D1 shows a grouping of integral chargeability values around 2 mV/V. This is also represented by the cluster of decay curves (in the left panel). The values for D10 are more evenly distributed which could point to the decreasing SNR of this subset (with a few outliers also visible in figure 5.7).

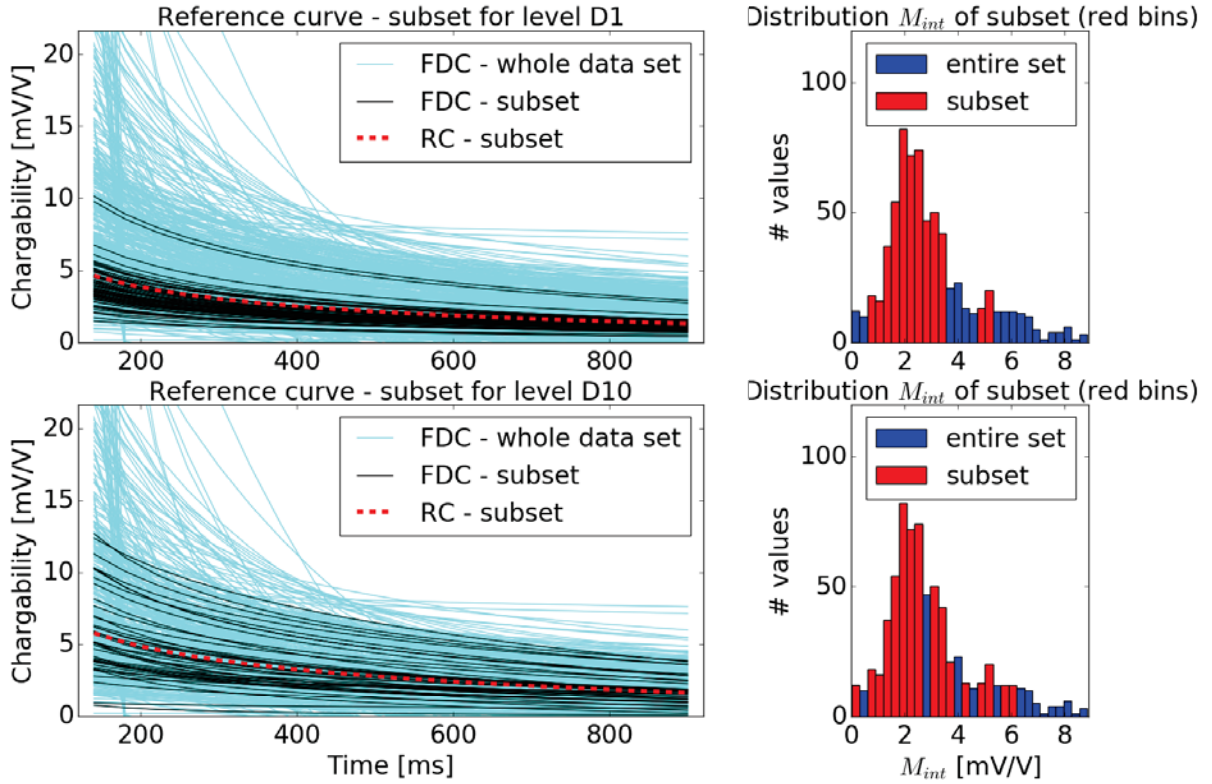


Figure 5.8: The fitted decay curves (black lines) and computed reference curves (dashed red line) for subsets based on the depth level partitioning. The red bins in the histograms in the right panels indicate bins containing the integral chargeability values of the subsets D1 and D10.

5.3 Analysis of the spatial consistency - the reference curve approach

The analysis of the spatial consistency realized in the DCA is based on the comparison of a reference curve with the MDC or FDC. Spatially inconsistent measurements can be either characterized by erroneous decay curves with implausible shape or magnitudes (i.e. integral chargeability values) without correlation within the data set. The reference curve approach can provide both - parameters describing deviations in the shape of the decay curve as well as deviations from the magnitude, both in regard to the reference curve. Such parameters are commonly applied for the characterization of outliers.

The analysis is based on a minimization process of the RMSD for $\Delta m_i = m_{m,i} - m_{RC,i}$ with $m_{m,i}$ and $m_{RC,i}$ being the partial chargeability values of the RC and MDC for the i -th gate. In small incremental steps, the RC is therefore being shifted along the chargeability axis in direction of the decay curve. For each shifting step the RMSD for Δm (for all gates) is calculated and compared with the previous one. Understandingly, the RMSD should decrease with each step moving the RC in direction of the decay curve. The minimization process stops for the condition

5.3 Analysis of the spatial consistency - the reference curve approach

$\text{RMSD}_j > \text{RMSD}_{j-1}$ (j is the step number) and the RMSD reaches a minimum at step $j - 1$. The RMSD_{j-1} (i) and the cumulative shift (ii), from the initial position of the reference curve to the position with minimized RMSD, are the parameters for the deviation in shape g (i) and deviation in magnitude k (ii) and represent the output of the reference curve approach. The principle of the reference curve approach is illustrated in figure 5.9.

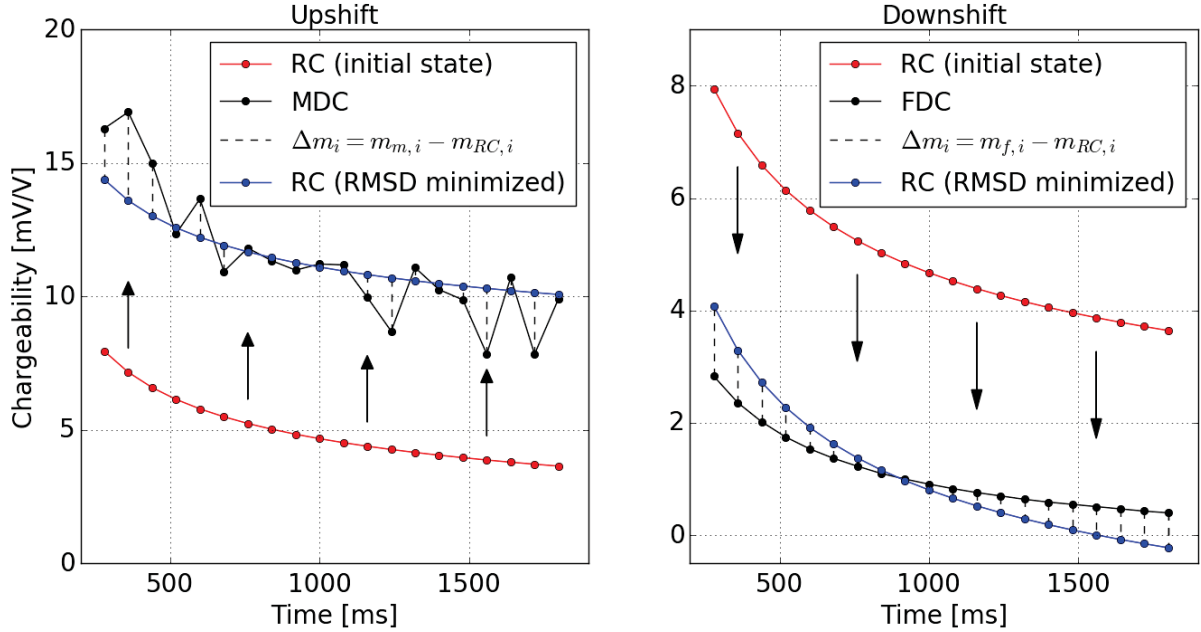


Figure 5.9: Illustration of the reference curve approach for an "up-shifting" and comparison with MDC (left panel) and "down-shifting" and comparison with FDC (right panel).

The comparison with the reference curve is strictly limited to a shifting along the chargeability axis - no deformations or rotations are being applied. Further, the step size needs to be chosen carefully to allow to characterize small changes in the RMSD values and thus an adequate approximation of the reference curve to the decay curve. A high value for the step size would result in overestimated RMSD values as well as wrong estimates of the deviation in magnitude (as the reference curve cannot approximate the decay curve). It is important to point out that the minimized RMSD only represents a local minimum. For rare cases, there might be a second minimum for the RMSD with an even smaller value - this would then be referred to as global minimum. However, solving for the global minimum would require shifting the reference curve over a much broader range of values, resulting in a higher computational effort. Nevertheless, for the DCA it has shown that the use of the local minimum is sufficient.

The comparison with the reference curve can be applied for the MDC and FDC depending on the objective of the analysis. Using the FDC instead of the MDC has shown to provide

more appropriate estimates of the deviations in shape as the random noise in the MDC would bias the RMSD. As illustrated in figure 5.9 is the comparison not limited to an "up-shifting" of the RC. In order to differentiate between an "up-" (k_u) and "downshift" (k_d) of the RC the resulting deviations in magnitude are being assigned to positive and negative signs respectively. The reason for that is an easier definition of thresholds for the filtering.

5.4 Characterization of outliers

To be of practical use parameters obtained from the reference curve approach need to describe possible outliers in a data set. Hence, in this section the deviation parameters k and g for different realizations of the reference curves (i.e. partitioning approaches) on the basis of a MG and DD data set will be investigated. The data sets were selected due to the different SNR of the DD and MG configuration and the dynamic in the integral chargeability values. The pseudosections of the raw data are presented in figure 5.10 a) and b). In order to validate the correlation between the parameters and outliers, the DD data set was filtered following the normal-reciprocal approach (as described in Flores Orozco et al., 2012). Measurements for which the normal-reciprocal misfit of the integral chargeability exceeds a value greater than two times the standard deviation of all misfits were removed as outliers. The small differences in the integral chargeability values, as can be observed between the raw and filtered pseudosection in figure 5.10 b) and d), are due to the averaging of the integral chargeability values of the normal and reciprocal data set (as mentioned in section 2.7). For the MG data set a manual removal of outliers was performed and the corresponding pseudosection is presented in figure 5.10 c). Let it be assumed that both the filtered MG and DD data set are free of systematic errors (outliers).

Outliers, associated to non-decaying curves would bias statistical analysis (e.g. the computation of the reference curve) and therefore need to be removed beforehand. The identification of non-decaying curves is based on a two step procedure. In the first step a linear model ($f(x) = c + dx$) is fitted to the measured decay and curves with increasing tendency as well as negative curves (characterized by only negative partial chargeability values) can be identified by an analysis of the model parameters. A positive parameter d indicates non-decaying curves whereas negative decay curves should be characterized by negative values of the parameter c . However, cases might occur (typically related to measurements characterized by low SNR) where this approach is not able to identify a non-plausible curve. Hence, the second step consists of an analysis of the model parameters of the fitted decay curve (c.f. equation 3.1b). FDCs for which the model parameters fulfill the conditions $a < 0$ and $b < 0$ or $a > 0$ and $b > 0$ are being removed. Data sets after the removal of non-decaying curves will from now be referred to as prefiltered data sets. The pseudosections of the prefiltered MG and DD data set used in the following sections are presented in figure 5.10 e) and f).

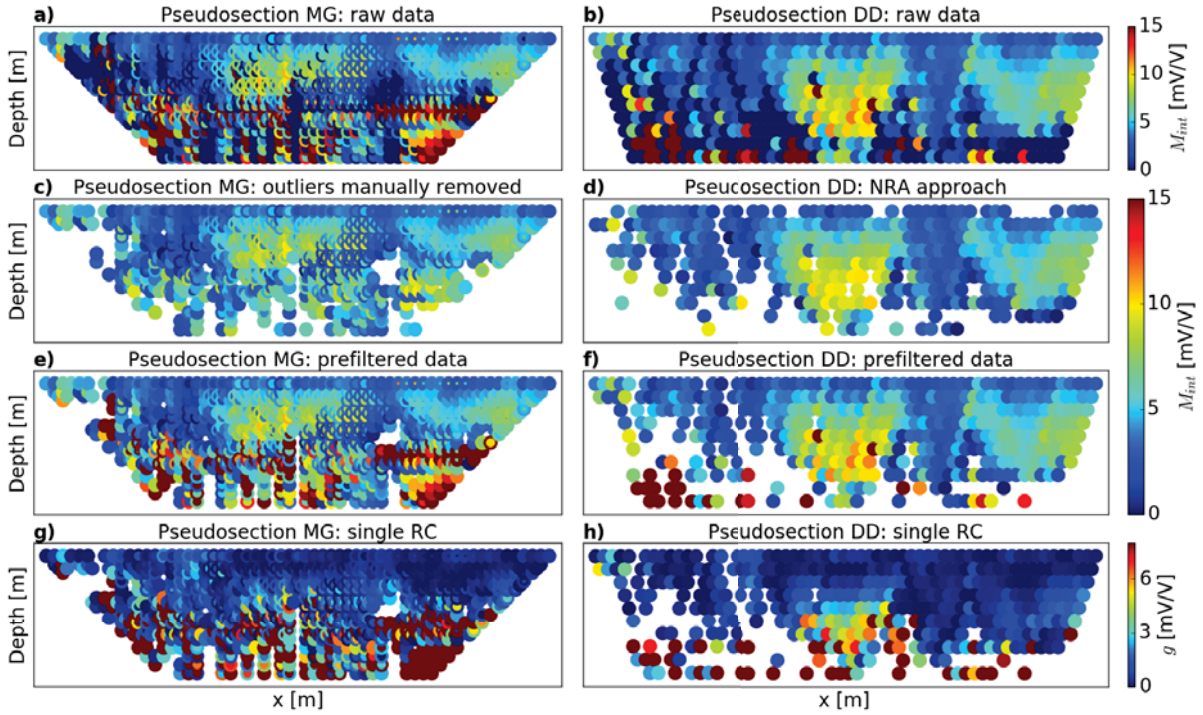


Figure 5.10: Pseudosections of the raw data sets for a MG a) and DD b) configuration, after the removal of outliers c) and d) and the after the removal of non-decaying curves only e) and f). g) and h) present the pseudosections of deviation in shape g as obtained from the reference curve approach using only one single reference curve (RC).

5.4.1 Single reference curve

The analysis of spatial consistency can also be conducted using just one single reference curve. Therefore, all measurements after the prefilter were used to compute the reference curve. The deviation parameters g (for the shape) and k (for the magnitude) as introduced in section 5.3 were determined in regard to this single RC using the fitted decay curve of each measurement.

Panels g) and f) of figure 5.10 present the pseudosections of the deviation parameter g for the MG and DD data set. It seems that g obtained from this method is sensitive to outliers, yet some exceptions can be observed. In particular for the DD configuration several outliers in the bottom left section of the pseudosection are not being identified. Furthermore would a removal of high g values lead to a removal of measurements associated to high integral chargeability values in the center of the array. Hence, following the requirement to remove as few measurements as possible, the analysis of g appears poorly suited, as such method may be too sensitive to random error even for measurements related to high signal strength.

For one single RC the values of k , in a first approximation though, are similar to a difference of the measured integral chargeability to a median value of the data set. The pseudosections would therefore display the same distributions as in a) and b) of figure 5.10 after the subtraction of the median of the integral chargeability values of the data set. Although the parameters would perfectly describe the corresponding outliers the problem would still be the same, namely adequate thresholds for outliers cannot be defined. For such either a-priori information or a visual analysis of the corresponding histograms are needed (as discussed in chapter 4).

5.4.2 Current dipole partitioning

The values for the deviation in shape g are presented in the pseudosections in figure 5.11 a) and b) and the corresponding values for the deviation in magnitude k are shown in 5.12 a) and b). An analysis of both values revealed a strong correlation with outliers regardless of the electrode configuration. The cluster of outliers in the right bottom section of the MG data set is slightly better characterized by k , however the distinction between outliers and valid measurements is more exact for g when compared with the filtered data sets in figure 5.10 e) and f). One might argue that the pseudosections reveal a similar pattern to the prefiltered data presented in figure 5.10 c) and d) and raise the question on the difference between k values for the single RC and the current dipole partitioning. In contrast to the single RC the comparison with multiple RCs of the current dipole approach cannot be approximated by a single subtraction (i.e. a difference to one median value) which results in a higher variability of k for a comparison with the multiple reference curves.

5.4.3 Depth level partitioning

The distributions of the deviation parameters after performing the reference curve approach on the basis of the depth level partitioning are in figures 5.11 c) and d) presented for g and in figure 5.12 c) and d) for k . The deviation in shape g reveals only a weak correlation with the associated outliers for the MG data set (figure 5.11 c)). The cluster of anomalously high integral chargeability values in the center right section of the pseudosection is not represented by g which can be related to an excess of outliers in the corresponding subsets and thus a comparison with a reference curve only representative for outliers. A comparison with the pseudosection of the DD data set after the removal of outliers following the NRA approach (figure 5.10 d)) indicates a stronger correlation of g with outliers for the DD configuration (figure 5.11 d)). For both data sets, horizontal band-like distributions of g can be observed, with values of $g > 15$ mV/V (figure 5.11 c)). The pseudosections of the deviation in magnitude k , as presented in figure 5.12 c) and d), show similar patterns (horizontal bands). Furthermore, for the MG data set k reveals only a weak correlation with outliers (consistently to g). The again more adequate

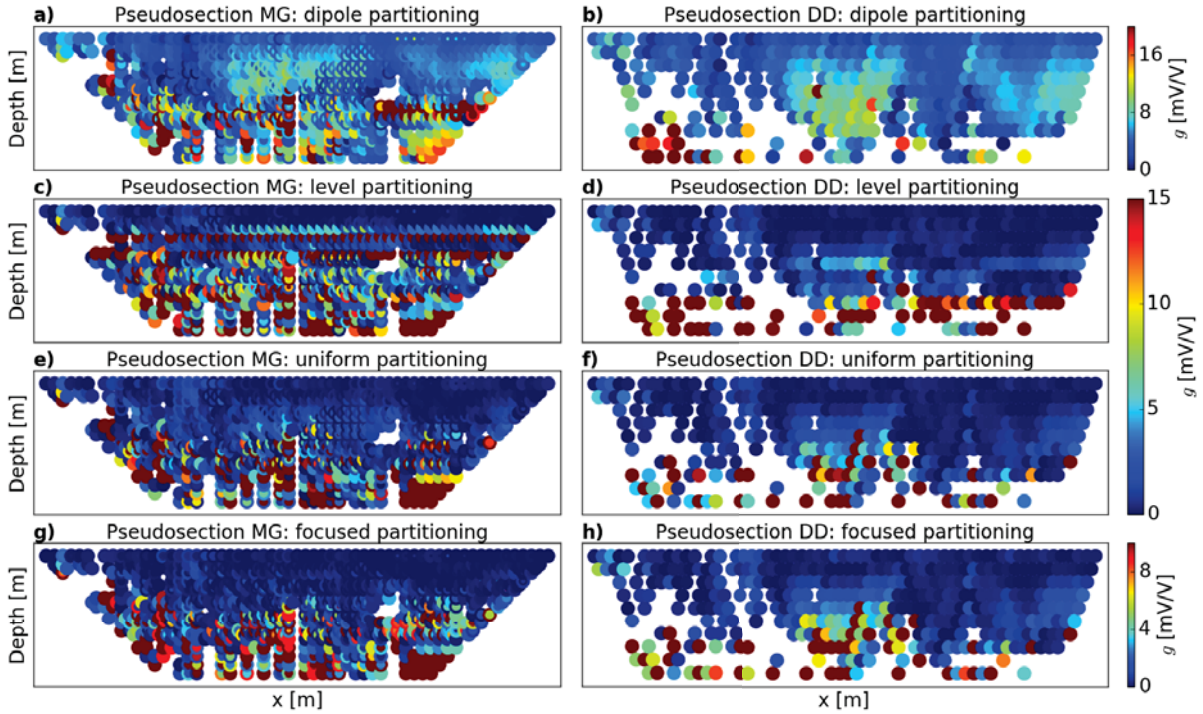


Figure 5.11: Pseudosections of the deviation in shape g , as obtained with the reference curve approach, for the current dipole- a) and b), the depth level- c) and d), the uniform- e) and f) and the focused partitioning approach. Figures of the left column refer to a MG dataset, figures of the right column to a DD data set. Please note the different color scales.

identification of outliers (here based on k) for the DD data set, as presented in figure 5.12 d) and in agreement with the NRA results in figure 5.10 d), is compromised by the band of negative k values (< -10 mV/V). A removal of such values would lead to a removal of measurements not related to outliers (as can be seen in figure 5.10 d)).

The band-like distributions of low and high values of both deviation parameters g and k are limiting the application of such in the scope of the identification of outliers, following the premise to remove as few measurements as possible. Further research is needed to investigate the applicability of such method for the determination of the deviation parameters. In its current form, the method seems to be highly sensitive to large spatial changes in the measured data leading to a poor statistical analysis.

5.4.4 Uniform partitioning

Until now, the choice of the RC for the comparison with the fitted decay was implicitly defined by the subset. Measured decay curves, respectively fitted decay curves of a subset were compared with the subset's RC. For the uniform partitioning the selection of the RC is performed

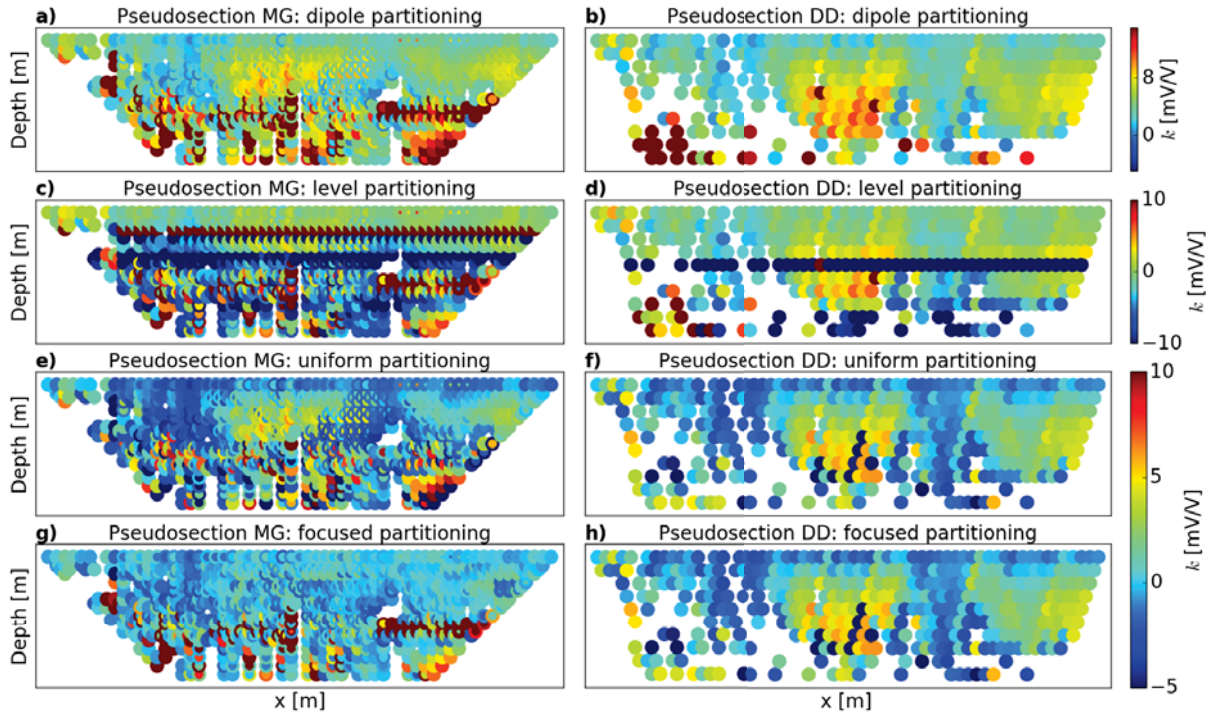


Figure 5.12: Pseudosections of the deviation in magnitude k , as obtained with the reference curve approach, for the current dipole- a) and b), the depth level- c) and d), the uniform- e) and f) and the focused partitioning approach. Pseudosections in the left column refer to a MG dataset, pseudosections in the right column to a DD data set. Please note the different color scales.

differently. Therefore the mean value of the partial chargeability values of the RCs and the mean value of partial chargeability values of the fitted decay curve (which equals an unweighted calculation of the integral chargeability - please refer to equation 2.3) are calculated. The RC used for comparison is the one with the smallest absolute difference to the fitted decay curve's mean value.

Panels e) and f) of figures 5.11 and 5.12 present the distribution of the deviation in shape g and deviation in magnitude k in pseudosections. Outliers in the bottom left and center areas of the MG pseudosection (figure 5.11 e)) correlate well with g . The cluster of outliers in the center right section is however not represented by g . A possible explanation is that the computation of one of the reference curves was actually based on this particular measurements (i.e. outliers) and deviations (g and k) for this measurements will therefore be small. For the DD data set the agreement of outliers and g is small (compare with 5.10 d)). Valid measurements of the polarizable anomaly in the center of the pseudosection are furthermore characterized by high values of g and at risk to be removed during the filtering.

As for the pseudosections of the deviation in magnitude k it is obvious that there is hardly

any possibility for an usage in the identification of outliers. Neither the MG nor the DD data set reveal a clear distinction in the values of k between valid measurements and outliers. Also, particularly for the DD data set the highest values of k correlate with the polarizable anomaly in the center which is in fact the opposite of what the characterization was intended for. Summarizing it can be concluded that k as obtained with the uniform partitioning approach is not suited to detect outliers. The deviation in shape g is potentially better suited.

5.4.5 Focused partitioning

The reference curve for the comparison with the FDC was selected following the techniques mentioned before, however using RCs defined for subsets based on the focused partitioning approach. The pseudosections in figure 5.11 g) and h) present the distribution of the deviation in shape g . When compared with the MG pseudosection of g following the uniform partitioning, as presented in figure 5.11 e), the choice of the different subsets used for the computation of the RC is directly reflected in g . For the focused partitioning (figure 5.11 g)) also the cluster in the center right section of the pseudosection is represented by increased values of g (>8 mV/V) and there's an adequate discrimination in the values of g between valid measurements (0 to 5 mV/V) and outliers (>5 mV/V, c.f. figure 5.10 c)). The performance of g for the identification of outliers for the DD data set (figure 5.11 h)) is less convincing. When compared with the pseudosection of g in figure 5.11 f) a quick analysis reveals a similar distribution as for the uniform partitioning. Apparently the subsets and corresponding reference curves are similar to the ones defined for the uniform partitioning. As stated in section 5.2 does the focused partitioning degenerate to the uniform partitioning approach when no relative minima in the histogram can be found. However for such a case the pseudosections in 5.11 f) and h) would need to be identical - which is not the case. Likely the similarity is simply related to almost identical subsets. Panel g) of figure 5.12 presents the pseudosection of the deviation in magnitude k for the MG data set. High values of k are in agreement with outliers (c.f. figure 5.10 d)) and are well delimited from k for valid measurements (-5 to 5 mV/V for valid measurements and >10 mV/V for outliers). The pseudosection of k for the DD data set (figure 5.12 h)) reveals an identical distribution of k as for the uniform partitioning (figure 5.12 f)). A discussion on that can be found in the section above.

5.4.6 Other parameters

5.4.6.1 Goodness of fit

Figure 5.13 c) and d) presents the pseudosections of the logarithmic goodness of fit (gof) for the MG and DD data sets used in the previous sections. The gof was computed based on the equation 3.4 and a strong correlation between outliers, as visible in 5.13 a) and b) and the gof can be observed. As the gof is a parameter of the deviations of the FDC from the MDC it is

strongly sensitive to changes in the shape of the curve. The erratic behavior of the decay curves typically increases with decreasing SNR (as discussed in section 3.1) and it can be assumed that the gof is an indicator of the signal strength. This is also justified by the small gof values for the highly polarizable anomaly in the pseudosections. Furthermore, the different SNR of the used electrode configurations are also represented by the magnitude of the gof, revealing higher gof values for DD than for MG configurations.

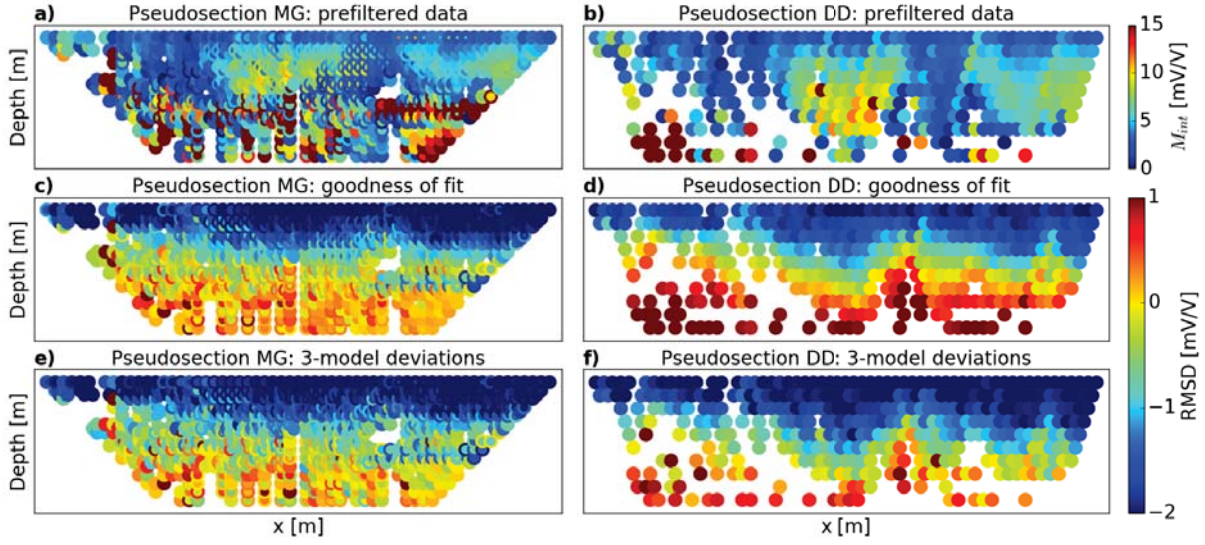


Figure 5.13: Pseudosections of the prefiltered MG a) and DD b) data sets and the corresponding pseudosections of the goodness of fit c) and d) and 3-model deviations e) and f).

5.4.6.2 Deviation between model curves fitted to all gates and gates with even/uneven numbers – 3-model deviations

An early stage approach for the characterization of outliers was based on a comparison of the model curves fitted to all gates of the MDC with those fitted to gates with an even and uneven number. If $m_a = [m_1, m_2, \dots, m_n]$ are the n partial chargeability values of the decay curve, $m_e = [m_2, m_4, \dots, m_n]$ and $m_u = [m_1, m_3, \dots, m_{n-1}]$ are the partial chargeability values of the even (m_e) and uneven (m_u) gate numbers. For each realization (m_e, m_u) the RMSD from m_a was evaluated and the mean value of the two RMSD value is being referred to as *3-model deviation*. The assumption is that for erratic decay curves the differences between the fitted model curves should be higher than for smoothly decaying curves when comparing curves fitted to different sampling.

In figure 5.10 e) and f) the pseudosections of the logarithmic 3-model deviations are presented. As can be seen there is no correlation with outliers and the overall pattern and magnitude of

values are similar to the case of the gof. This means that although the same model is fitted, different realizations (m_a, m_e, m_u) reveal variations in the calculated RMSD. Such variations are related to changes in the quality (i.e. the shape) of the decay curve due to presence of random error, which is typically higher for a low SNR. Due to the similarity to the goodness of fit (in both the distribution and magnitude of the values) the 3-model deviations could therefore also be used as an indicator of signal strength. However, given this similarity, the lower computational effort to calculate the gof (as the 3-model deviations require the fitting of 3 model curves) and the non-applicability to identify outliers, the 3-model deviations were not further investigated.

5.5 Definition of parameter thresholds

The selection of adequate values to define the range of valid measurements and outliers represents the second most important step, after the identification of outliers, in any filtering procedure and needs to be performed with uttermost care to prevent a filtering scheme from under- or overfiltering of the data set. Moreover threshold values should be defined automatically and require to be applicable to a wide range of possible data sets without the need of a manual readjustment of thresholds or an additional postprocessing (e.g. outliers still prevail in the data set after the filter).

Incorporated into a filtering scheme, subsequently three different approaches to select threshold values for the parameter k (the deviation in magnitude, as obtained from the reference curve approach) will be discussed and reviewed on their applicability. Please note that the approaches, however after some minor modifications, can be also applied to other parameters besides k (e.g. values for the goodness of fit or integral chargeability values).

5.5.1 Stepwise selection of threshold values

As the name implies this approach consists of a stepwise refinement of the threshold which is based on the standard deviation of k . As can be seen for example in figure 5.14 a) do outliers, associated to high integral chargeability values, still prevail in the prefiltered data sets. Such outliers are typically related to high values of k and thus would strongly influence the calculation of the standard deviation. Hence, a second prefilter (based on a histogram analysis) was applied to achieve a further removal of high integral chargeability and k values. The actual refinement process of the threshold is then based on a three step procedure. For each step the standard deviation σ is calculated and used to define two thresholds ($t_1 = \sigma$ and $t_2 = -\sigma$). Measurements for which k is lower respectively larger than the corresponding threshold are being removed. This is then followed by a histogram analysis of the integral chargeability values for a further removal of possible remaining outliers. The second and third step follow analogously. However for each new step the filtered data set from the preceding step is used for the calculation of the standard

deviation.

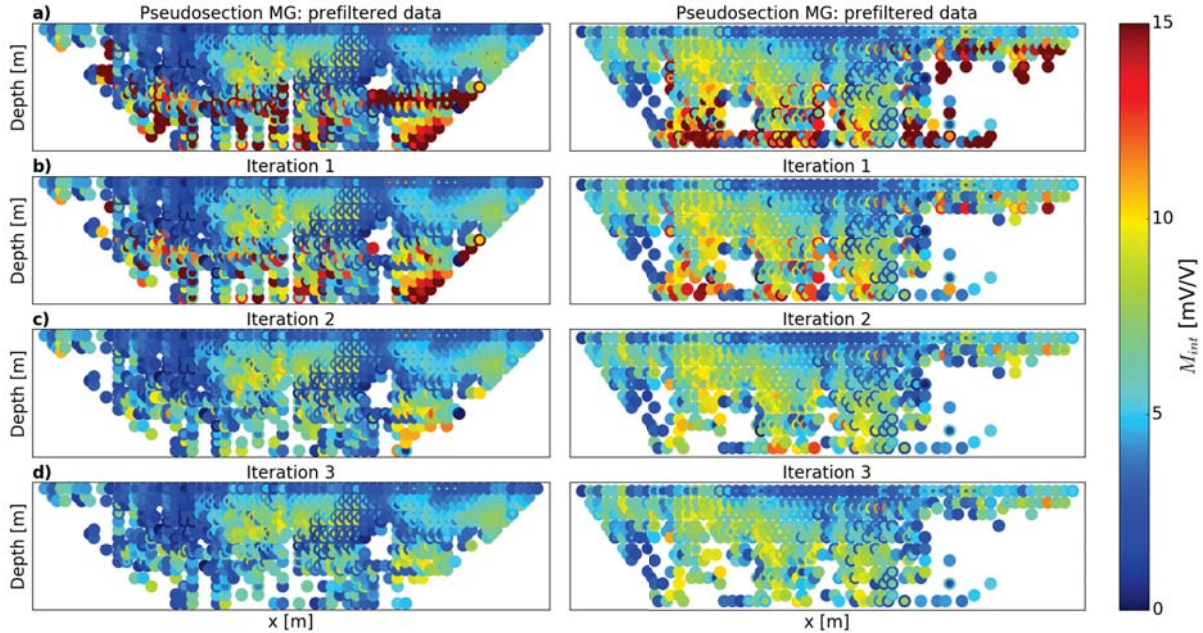


Figure 5.14: Pseudosections of the prefiltered data sets as well as the different iteration steps for a filtering scheme based on the stepwise definition of threshold values. Each column presents a particular data set collected with a MG configuration and the defined threshold consisted of two times the standard deviation of k .

Of course is the choice of three steps for the procedure an empirical one. However it was found that for the majority of the data sets three steps provide an acceptable trade-off between under- and overfiltering. Furthermore is the actual threshold not directly realized as the standard deviation of k rather than the standard deviation times a multiplication factor which is different for the used electrode configuration. For the MG configuration a multiplication factor of 2 was found to be well suited, whereas for DD configurations a factor of 3 is needed to provide similar results (which probably reflects the different SNR of the two configurations). Other statistical parameters, such as percentiles or the median absolute deviation as threshold values have been investigated but no robust criteria applicable to all data sets were found. For relatively clean data sets it might happen that the selected threshold would result in a removal of valid measurements. In order to account for such cases it could be advisable to introduce a stopping criterion. A possible criterion for example, could consist of the condition that thresholds may not be smaller than the median of the data set's integral chargeability values. Figures 5.14 and 5.15 present the pseudosections of the prefiltered data sets and individual filter steps (with the above mentioned stopping criterion implemented) for data collected with a DD and MG configuration. Analysis of the tested data revealed an adequate definition of outliers even for data sets characterized by

5.5 Definition of parameter thresholds

a significant amount of outliers, e.g. figure 5.14 a), as well as a clean data set, e.g. left panel of figure 5.15 a). The filter results of the DD data sets (see figure 5.15) are in agreement with results following the normal-reciprocal approach (Flores Orozco et al., 2012b) as presented in figure 5.16. This further demonstrates the applicability of this threshold definition approach.

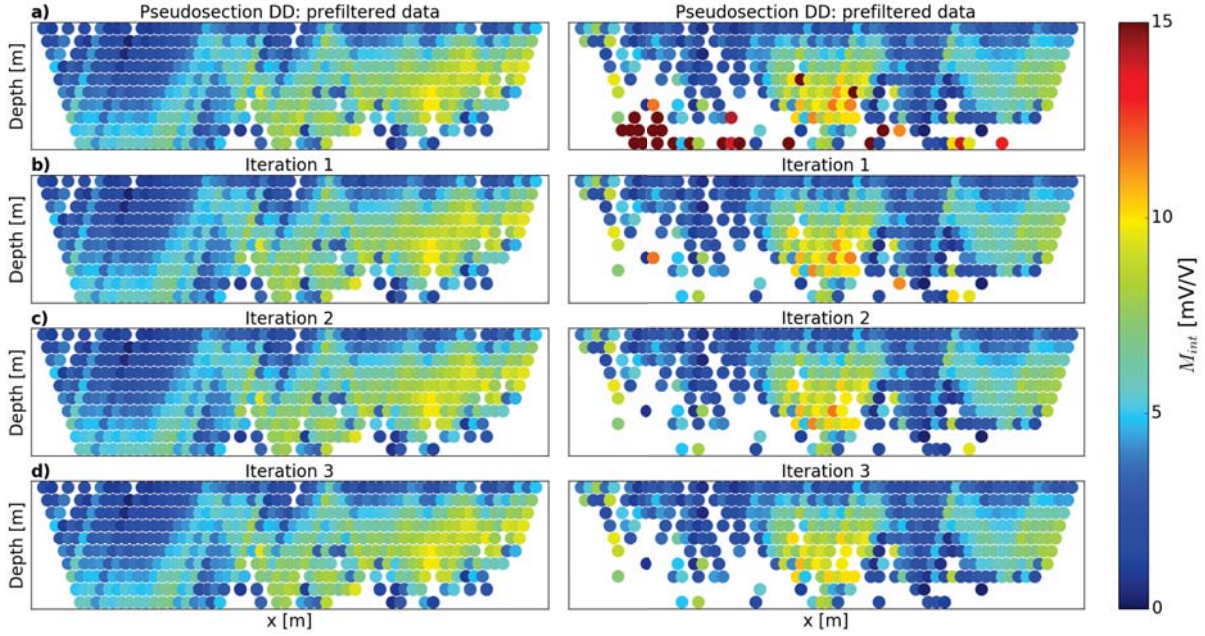


Figure 5.15: Pseudosections of the prefiltered data sets as well as the different iteration steps for a filtering scheme based on the stepwise definition of threshold values. Each column presents a particular data set collected with a DD configuration and the defined threshold consisted of three times the standard deviation of k .

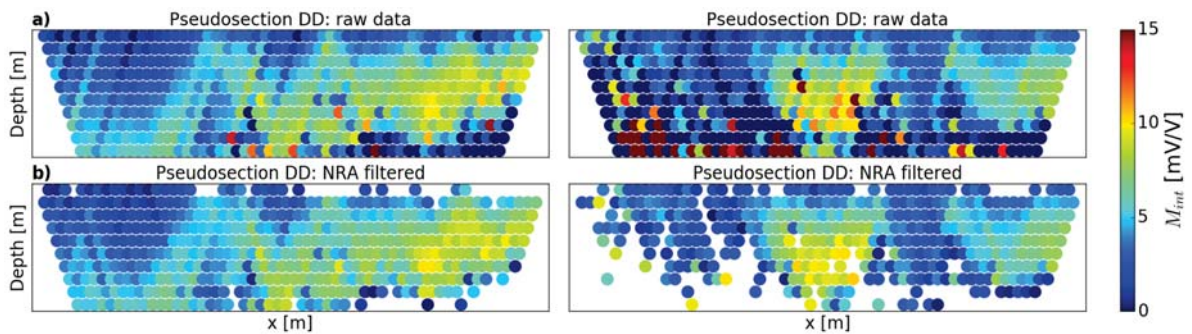


Figure 5.16: Pseudosections of the raw and filtered data sets for the removal of outliers following the normal-reciprocal approach. Measurements for which the associated normal-reciprocal misfit of the integral chargeability exceeds two times the corresponding standard deviation of the misfits of the entire data set were removed as outliers.

5.5.2 Thresholds defined by a histogram analysis of k

For this approach the definition of the threshold is solely based on a histogram analysis of k . The value for k corresponding to the last found gap in the analysis is the threshold being applied during the filtering. In order to take care of outliers associated to very small integral chargeability values, the histogram analysis is performed in forward direction (starting with the bin containing the smallest value for k) and additionally in reversed direction (starting with the bin containing the highest value for k). Thus two separate thresholds for values of k smaller and greater than 0 are being defined. Remaining outliers after this filter step subsequently were assessed by a histogram analysis of the integral chargeability values (consistently to the approach before).

Although this approach revealed promising results at first, no general applicability, particularly for data sets characterized by high amounts of erroneous measurements, was given. Here the key assumption of the histogram analysis that k values associated to outliers are separated from a main distribution was not fulfilled and thus the overall concept couldn't be applied. It was further found that there's a generally higher sensitivity to the number of bins n_b selected than for example using the histogram analysis for the integral chargeability values. Particularly for noisy data sets an adjustment of n_b based on the individual characteristics of the data set would be required. However no robust criteria was found. An alternative approach of solving this difficulty consisted of formulating additional criteria in the histogram analysis of k to prevent an under- respectively overestimation of the threshold. Although appealing, this approach also suffered from similar limitations as the formulation of n_b because no robust definitions applicable to a wide range of different data sets could be found.

5.5.3 Fixed thresholds with additional conditions

Instead of calculating the standard deviation of k directly, this approach relies on separating k into the corresponding "up-shift" and "down-shift" values k_u and k_d and a subsequent calculation of the associated standard deviations. Rows a) and b) of figure 5.17 present the pseudosections of the prefiltered data sets and after the removal of measurements associated to k_u and k_d values larger or smaller than the corresponding standard deviations. As can be seen and in agreement with the observations made in section 5.5.1 is the use of the same threshold definition (here the standard deviations of k_u and k_d) obviously not suited for the application to electrode configurations characterized by different signal strengths. It permits an adequate identification of outliers for the MG data set, however leads to a drastic removal of measurements for the DD data set, in particular of the high polarizable anomaly in the center of the pseudosection. An increase of the standard deviation to three times it's value, as presented in figure 5.17 c) can help to improve the filtering for DD data however results in few outliers removed for the MG data set. This general problem needs to be properly addressed in the filtering scheme, particularly during

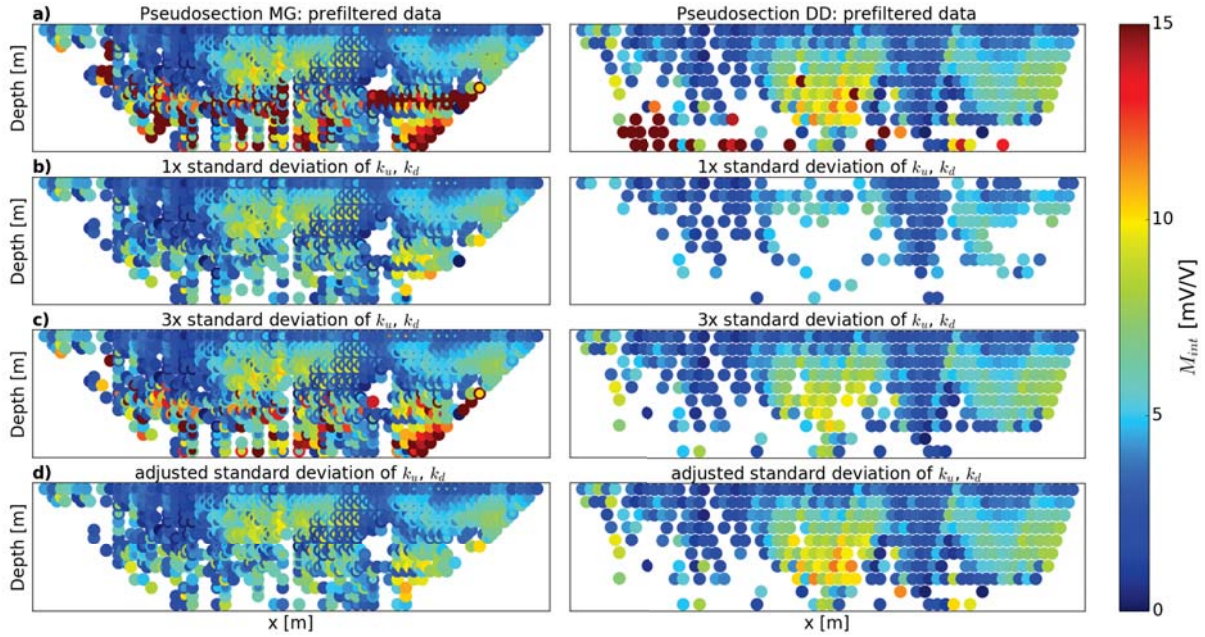


Figure 5.17: Pseudosections of the prefiltered and filtered data sets collected with a MG (left column) and DD (right column) configuration. Rows b) and c) represent the filter results for different multiplication factors of the standard deviation. d) shows the filtered pseudosections as obtained with the adjusted threshold values.

the definition of threshold values for k , k_u and k_d . Thus, the approach here consists of initially fixing the thresholds for k_u and k_d to three times their standard deviations and a subsequent optional adjustment depending on the individual characteristics of the data set. This procedure is then followed by a histogram analysis of the integral chargeability values to remove remaining outliers. The use of three times the standard deviation has shown to provide satisfying results for most of the data sets, however particularly for fairly clean (i) and "noisy" (ii) data sets the adjustment is absolutely needed. The rules for the identification of (i) and (ii) and the corresponding adjustments can be found in table 5.6. Figure 5.17 d) presents the pseudosections after the removal of outliers applying the adjusted threshold. In comparison with filter results from the stepwise selection of threshold values, as presented in figures 5.14 and 5.15, this approach retains more measurements with high integral chargeability values. Analysis of the tested DD data set further revealed a removal of outliers similar to the normal-reciprocal approach (c.f. right column of figure 5.16).

The question arises whether other statistical parameters for the selection of the threshold value apart from the standard deviation would be better suited and could eventually eliminate the need for an optional adjustment. Numerous other parameters (e.g. percentiles, median, weighted average and others) have been investigated but none revealed a deviating behavior

from the standard deviation in terms of the required additional adjustment of the threshold. Furthermore it was found that the empirical definitions and rules presented in table 5.6 are only applicable to the standard deviation and the mean of k_u and k_d . Apart from that, no robust criteria applicable to the majority of data sets could be found. From all other tested statistical parameters only the mean of k_u and k_d represents a possible candidate (i.e. threshold value) for the incorporation into a filtering scheme. However compared to the standard deviation the determined thresholds are smaller and thus will result in the removal of more measurements. Particularly for noisy data sets this could also be intentional.

Case	Definition	Threshold k_u	Threshold k_d
clean (i)	3 times standard deviation of k_u < median of integral chargeability values of data set	\Rightarrow 4 times standard deviation	\Rightarrow 4 times standard deviation
noisy (ii)	3 times standard deviation of k_u > 2 times median of integral chargeability values of data set	\Rightarrow 1.5 times standard deviation	\Rightarrow single standard deviation

Table 5.6: Automatable criteria for the definition of clean and noisy data sets and the adjustment of the corresponding thresholds for k_u and k_d .

Chapter 6

Error Modelling

The determination of error models describing the inherent random errors of the measurements in a data set and the application of such during the inversion is critical to solve for electrical images with high contrast and enhanced resolution. This needs to be addressed carefully, considering that an underestimation of data error is typically associated to the creation of artifacts in the images, whereas data error overestimation generally leads to the loss of resolution (LaBrecque et al., 1996). Thus the subsequent analyses aim at finding parameters describing the random error in measurements, the adjustment of error models to such and the application in an inversion scheme (Kemna, 2000). The results obtained here are also compared with parameters from the well-established normal-reciprocal approach (NRA) which depicts the reference approach.

6.1 Finding parameters describing the random error

This section will discuss different parameters derived within this thesis (denoted as DCA misfits) in regard to their applicability to describe the random error in measurements and investigate whether they are applicable in the same way as existing error models based on the normal-reciprocal approach (NRA). Therefore, such parameters describing outliers should be a function of resistance R and show a distribution similar to the NRA misfit presented in figure 6.1 - with high misfit values for small resistances and low values for high resistances and misfits being defined as the difference of measurements collected in the normal- and reciprocal configuration (refer to section 2.7). In particular should the parameters exhibit a normal distribution centered around zero to be gaussian error. Distributions departing from that indicate a correlated error, thus pointing to systematical errors needed to be removed. The adjustment of the error models to the misfit, i.e. the parameter describing the random error, will be performed following the concept of the so-called bin analysis, as it facilitates the comparison with the normal-reciprocal approach. The bin analysis consists of partitioning the misfits into several bins with respect to R and a subsequent adjustment of the error model to the standard deviations of each bin. For more details on the technique please refer to Koestel et al. (2008) and Flores Orozco et al. (2012b). In order to ensure a fair comparison of NRA and DCA misfits, the misfits for both

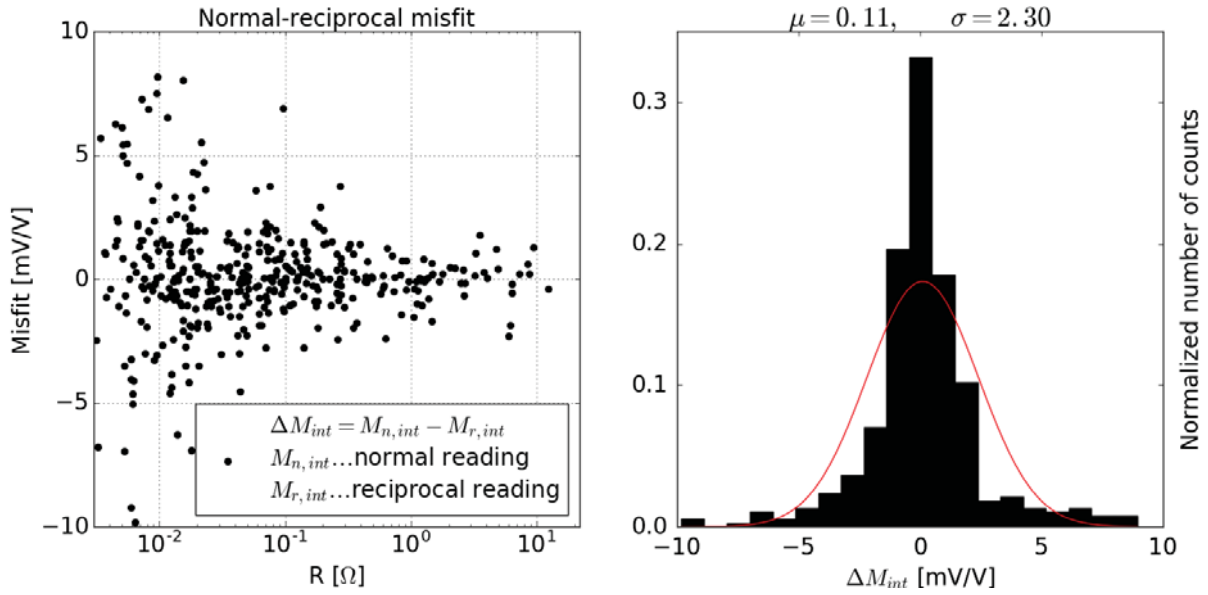


Figure 6.1: The left panel shows the normal-reciprocal misfit of the integral chargeability measurements ΔM_{int} as a function of the resistance R . The right panel presents the histogram of the misfit and the probability density function (red curve) justifying the assumption of a normal distribution.

approaches were derived for the measurements of a representative data set. Outliers were then removed following the criteria described in Flores Orozco et al. (2012b), namely those measurements with normal-reciprocal misfit of the integral chargeability larger than two times the standard deviation of the misfit of the entire data set. By this means the misfit values of both approaches can be compared for the same measurements (i.e. quadrupoles).

Figure 6.2 presents the values for the deviation in magnitude k (for different partitioning approaches) plotted as a function of R in comparison with the NRA misfit as well as the corresponding histograms of k in order to evaluate the assumption of a normal distribution. The red curves in the right column show the probability density functions. Please note that k was computed based on a comparison with the FDC. Plots of k for the MDC revealed similar patterns and are therefore not shown. Figure 6.2 a) presents the distribution of k following the focused partitioning approach revealing no dependence on the resistance and a uniform scattering of the values. The only variations from the NRA misfit can be observed for small resistances. A larger error for measurements associated to small resistance values would probably be underestimated, biasing the error estimates on the analysis of the k - R relationship. The homogeneous distribution is also reflected by the shape of the histogram. Figure 6.2 b) presents k as obtained for the computation with a single RC. The distribution does not follow the NRA pattern and seems more scattered with no dependence on R and is poorly represented by any model. Thus it was not further investigated. Figure 6.2 c) shows the distribution and corresponding histogram

6.1 Finding parameters describing the random error

of k for the current dipole partitioning. Here the computed mean value $\mu = -0.44$ indicates a non-gaussian error which is also confirmed by a visual analysis of the skewed distribution of k . It would of course be possible to center the distribution by subtracting a mean or median value but such procedure lacks the physical explanation and may result in a poor estimation of random error. Due to the lack of correlation with the NRA misfits it was concluded not to further investigate k (for any of the tested partitioning approaches) for the description of the random error.

Considering that deviations of the measured decay curve from a smooth fitted model curve or computed reference curve may be considered the result of random error in the chargeability readings further investigations aimed at the evaluation the potential of such misfits. The misfit, here denoted as Δm_i , is characterized as the difference of the partial chargeability values of the i -th gate of the two different decay curves, for instances of the FDC and MDC ($\Delta m_i = m_{m,i} - m_{f,i}$). The voltage decay of the available data sets was discretized using 20 gates, hence 20 different values of Δm_i , consisting of one for each gate, were computed. Figure 6.3 presents the distributions of Δm_i for the 1st, 10th and the 20th gate in comparison with the NRA misfit, both as a function of the corresponding resistance. The gate numbers were selected in order to evaluate the effect of a changing signal strength as associated to early and late times of the decay curve, on the distributions and magnitudes of Δm_i . As can be seen in figure 6.3 there is practically no difference between early and late gates and the distributions, the magnitudes as well as the corresponding histograms of Δm_i are consistent. The histograms, in accordance with the fitted probability density functions, also justify the assumption of a normal distribution and thus uncorrelated error. Furthermore are the observed patterns in agreement with the NRA misfits. However for resistances larger than $10^{-1} \Omega$, it appears that Δm_i is at least one order of magnitude smaller than the corresponding NRA misfit.

Instead of calculating Δm_i for the FDC, also realizations of the reference curves can be used ($\Delta m_i = m_{m,i} - m_{RC,i}$) for the comparison. In the following Δm_i computed for one single reference curve for the entire data set will be discussed. In comparison with Δm_i from the section above, are misfits computed with the single reference curve expected to be larger because the reference curve with it's fixed shape cannot approximate the MDC as well as the FDC, which is much more flexible. This is particularly interesting as error estimates based on Δm_i computed with the FDC might underestimate the actual data error due to the best possible approximation to the MDC. Figure 6.4 presents the distributions of Δm_i computed for the single RC and in comparison with the NRA misfits for the same gates ($i = 1, 10, 20$) as before. Such plots reveal that the distribution for the 1st gate (figure 6.4 a)) is significantly different from the one computed for the comparison with the single RC presented in figure 6.3 a). That can likely be explained by the fixed shape of the RC, which apparently cannot approximate the higher vari-

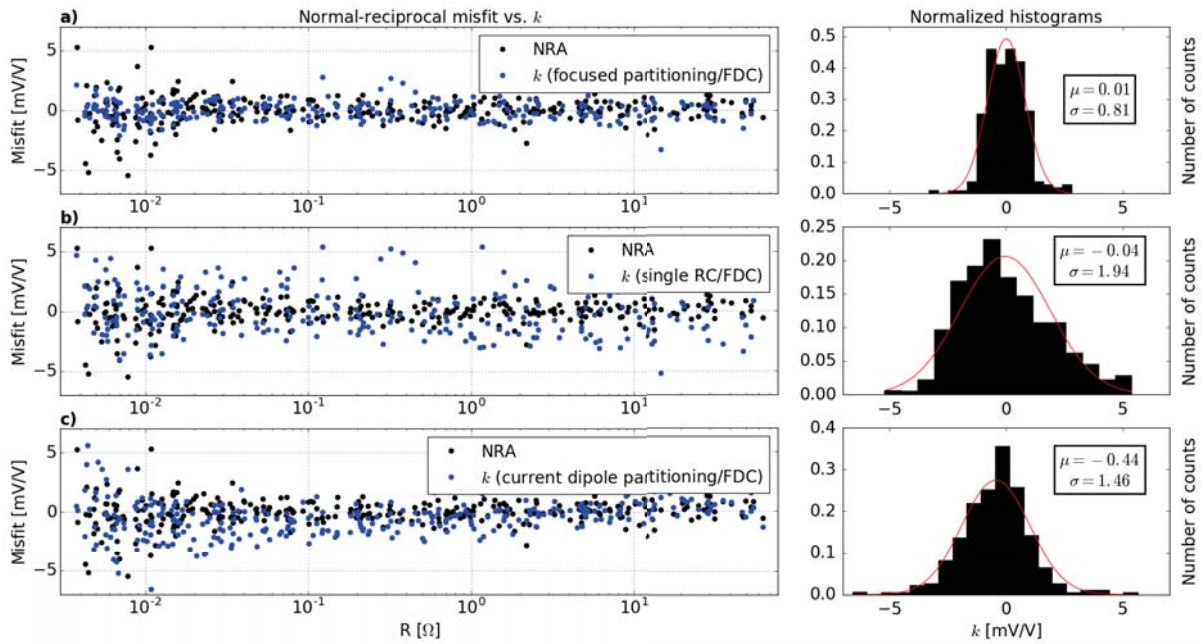


Figure 6.2: Values for the deviation in magnitude k , as obtained with different partitioning approaches, in comparison with the NRA misfit both as a function of resistance R . The histograms and probability density functions (red curves) in the right column are intended to evaluate the assumption of a normal distribution.

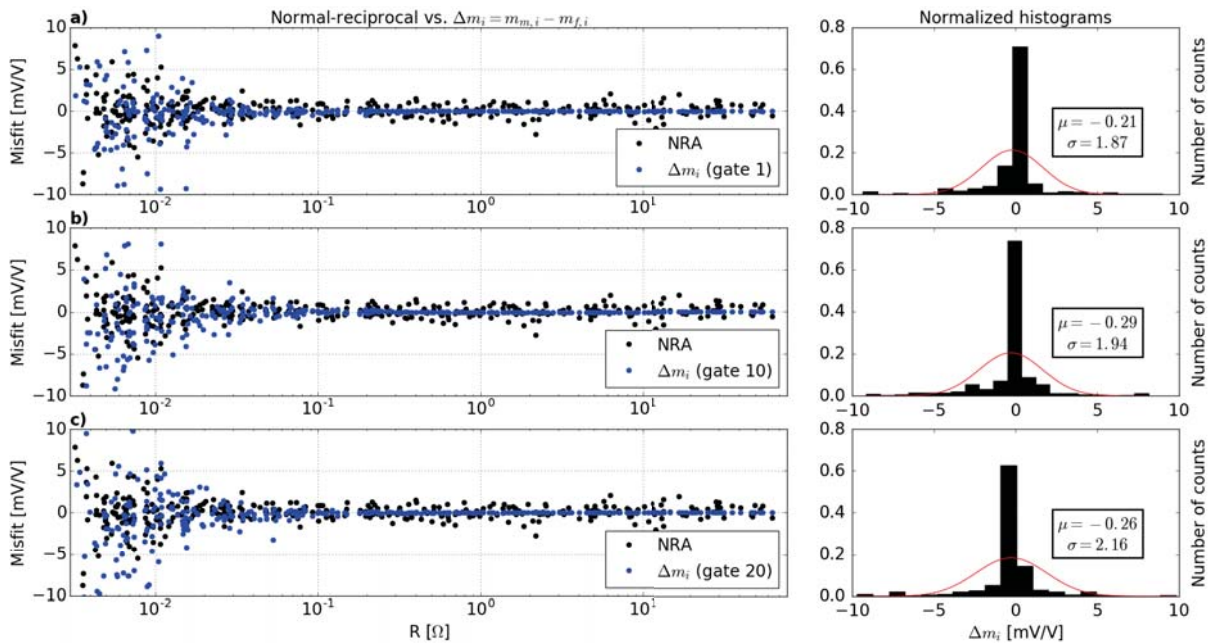


Figure 6.3: The distributions of Δm_i (for the comparison with the FDC) computed for different gates in comparison with the NRA misfit both as a function of resistance R . The histograms and probability density functions (red curves) in the right column are intended to evaluate the assumption of a normal distribution.

6.1 Finding parameters describing the random error

ability of the MDCs in the early times. Such an assumption is also confirmed by the distribution of Δm_i for the 10th gate, as presented in figure 6.4 b). Considering the concept of how the RC and MDC are being compared (please refer to section 5.3), the approximation using the RC for gates in the center of the decay curve should be the best possible and the distribution of Δm_i consistent to the one presented in figure 6.3 b). Finally figure 6.4 c) presents the distribution of Δm_i for the last gate (20). Contrary to the expectation, that the misfit would show a pattern consistent to figure 6.4 a), the magnitudes as well as the distribution are consistent to the NRA misfit without revealing a particular skewness similar to figure 6.4 a). This is also reflected by the histogram, which justifies the assumption of a normal distribution - in strong contrast to the histogram in figure 6.4 a), where $\mu = -0.77$.

Summarizing it can be concluded that both realizations of Δm_i (based on the comparison with the FDC and single RC) are likely suited to describe the random error. However, for Δm_i based on a comparison with the single RC, the distributions are varying depending on the selected gate (refer to figure 6.4). Furthermore, there are gates for which Δm_i does not meet the initially formulated requirements (normal distributed and pattern following the NRA misfit). Hence the choice of the best suited gate for Δm_i cannot be justified easily. A possible solution in order to overcome this limitation is the use of Δm_i for all gates in one combined analysis. Figure 6.5 presents the distributions of Δm_i computed for all gates of the decay curve as well as the corresponding histograms for the case of the comparison with the FDC (top panel) and single RC (bottom panel). As expected does the combined distribution of Δm_i in figure 6.5 a) not significantly differ from the distributions in figure 6.3 and the calculated standard deviations as well as the histograms are comparable. It can therefore be concluded that both approaches (single gate/combined gates) will provide similar parameters of the adjusted error models. However, the bin analysis will benefit of the larger number of points for a better estimation of the standard deviation in each bin, i.e. increasing the representativeness and robustness and thus it could be preferable to use the information of all gates together. The distribution presented in figure 6.5 b) (Δm_i for the single RC) reveals a similar pattern to the distribution in figure 6.5 a) (Δm_i for the FDC), however the misfits associated to resistances above $10^{-1} \Omega$ are at least one order of magnitude larger than the corresponding values in figure 6.5 a) and are closer to the NRA misfit. The deviating behavior of particular gates, as for example observed in figure 6.4 a), obviously is compensated by Δm_i associated to other gates and the histograms as well as the associated mean $\mu = -0.04$ clearly indicate a normal distribution. Hence, for this realization of Δm_i the adjustment of the error model should only be performed on the basis of the combined distribution in order to minimize the deviating effect of individual gates and to avoid the arbitrary choice of a best-suited gate for Δm_i . Furthermore are the observed pattern as well as the magnitudes of the misfit in good agreement with the NRA estimates.

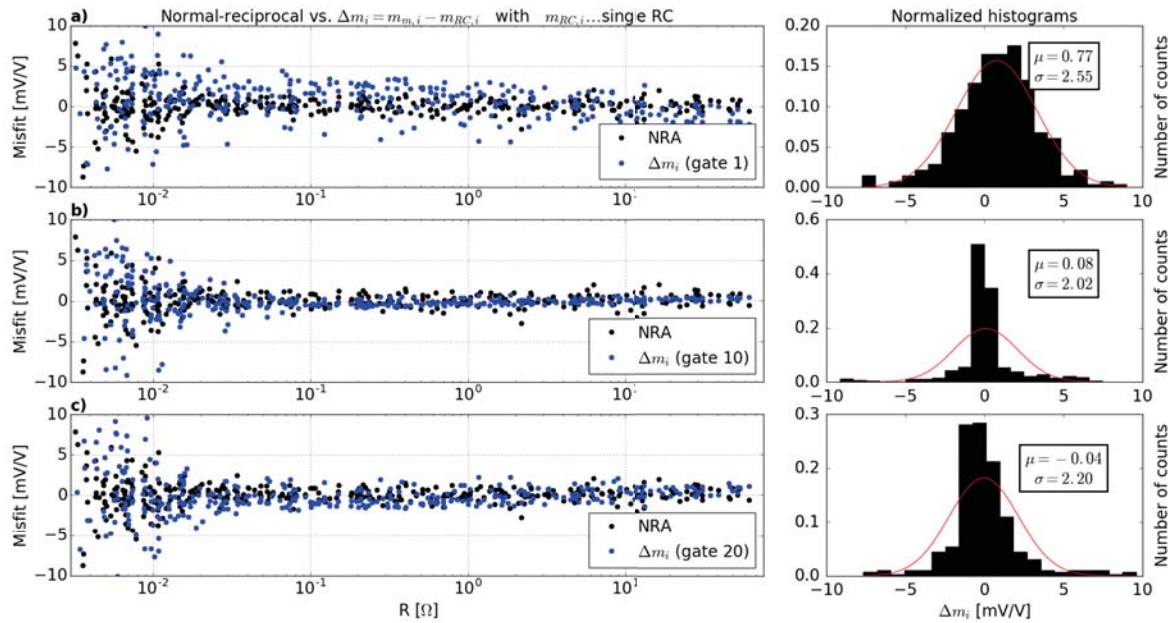


Figure 6.4: The distributions of Δm_i (for the comparison with the single RC) computed for different gates in comparison with the NRA misfit both as a function of resistance R . The histograms and probability density functions (red curves) in the right column are intended to evaluate the assumption of a normal distribution.

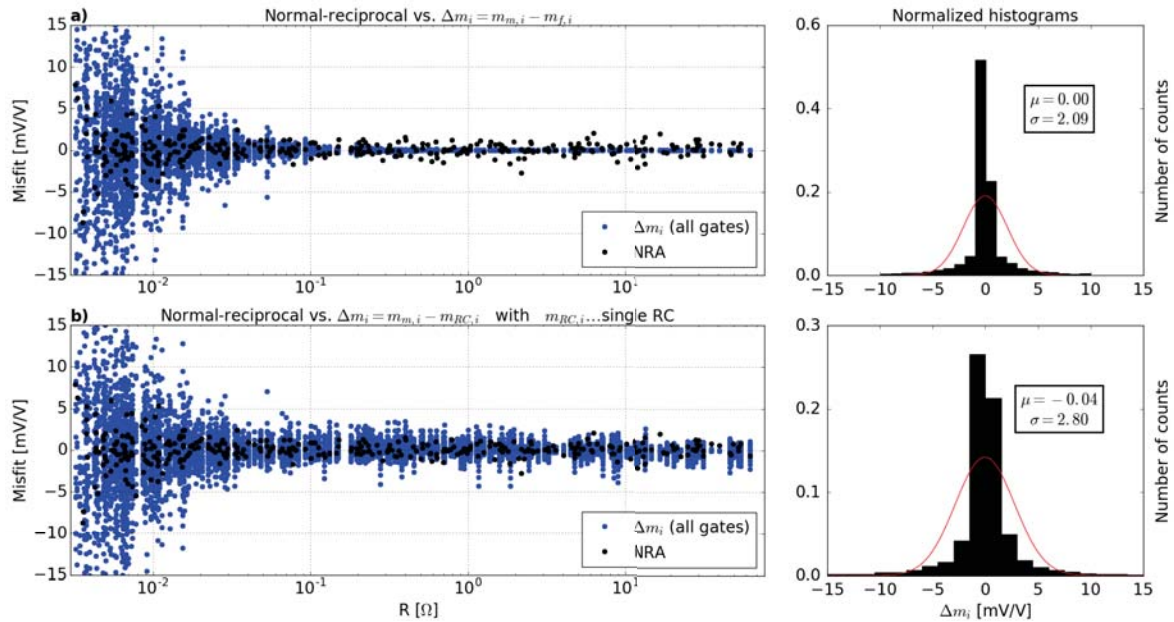


Figure 6.5: The distributions of Δm_i for all gates in comparison with the NRA misfit as a function of resistance R . The histograms and probability density functions (red curves) in the right column are intended to evaluate the assumption of a normal distribution. The upper panel presents Δm_i for the comparison with the FDC, whereas the distribution in the bottom panel shows Δm_i values computed for the comparison with a single RC.

6.2 Consistency between Δm_i of MG and DD data sets

For the general applicability of Δm_i in the scope of the error modelling it would be beneficial if the observed distributions are consistent for data sets collected with different electrode configurations. This is particularly important if data sets consisting of measurements collected with various electrode configurations are to be inverted as a joint data set. Commonly such data sets are being processed separately, however for subsurface conditions related to low IP responses, thus low SNR, the inversion of joint data sets of a MG and DD configuration can be useful to improve the contrast and quality of the electrical images. Hence, it is critical that (i) the random error can be described in a consistent manner and (ii) the adjusted error models are akin in order to avoid an over- or underestimation of data error for measurements of one particular electrode configuration. Otherwise it could happen that due to the wrong re-weighting of particular measurements contributed to the falsely applied error model, measurements from one configuration are "dominating" the inversion results and thus the beneficial character of the inversion of a joint data set is lost.

In order to assess the consistency of Δm_i in both the distribution and magnitude for two widely applied electrode configurations, the values for Δm_i were derived for a MG and DD data set associated to the same section of the subsurface (i.e. the same electrodes were used). For the DD data set outliers were removed consistently to the approach outlined before (using the normal-reciprocal methodology) and for the MG data set, outliers removal was performed by an analysis of the spatial consistency (please refer to chapter 5). Figure 6.6 presents the distributions of Δm_i (for all gates) as obtained for a comparison with the FDC (top panel) and with the single RC (bottom panel) for data sets collected with a MG (green) and DD (blue) configuration. The black dots represent the NRA misfit. As can be seen are the distributions as well as the magnitude of Δm_i consistent between the two configurations and no differences can be observed for the different realizations of the misfit (Δm_i for the FDC and single RC). Furthermore, figure 6.6 illustrates the higher signal strength typically related to MG configurations reflected by the smaller range of resistances as well as corresponding misfits. In conclusion, there are no indications of a deviating behavior in neither the distribution nor the magnitude of Δm_i for the used electrode configuration and thus the random error on basis of the combined distribution can be modelled in a consistent manner.

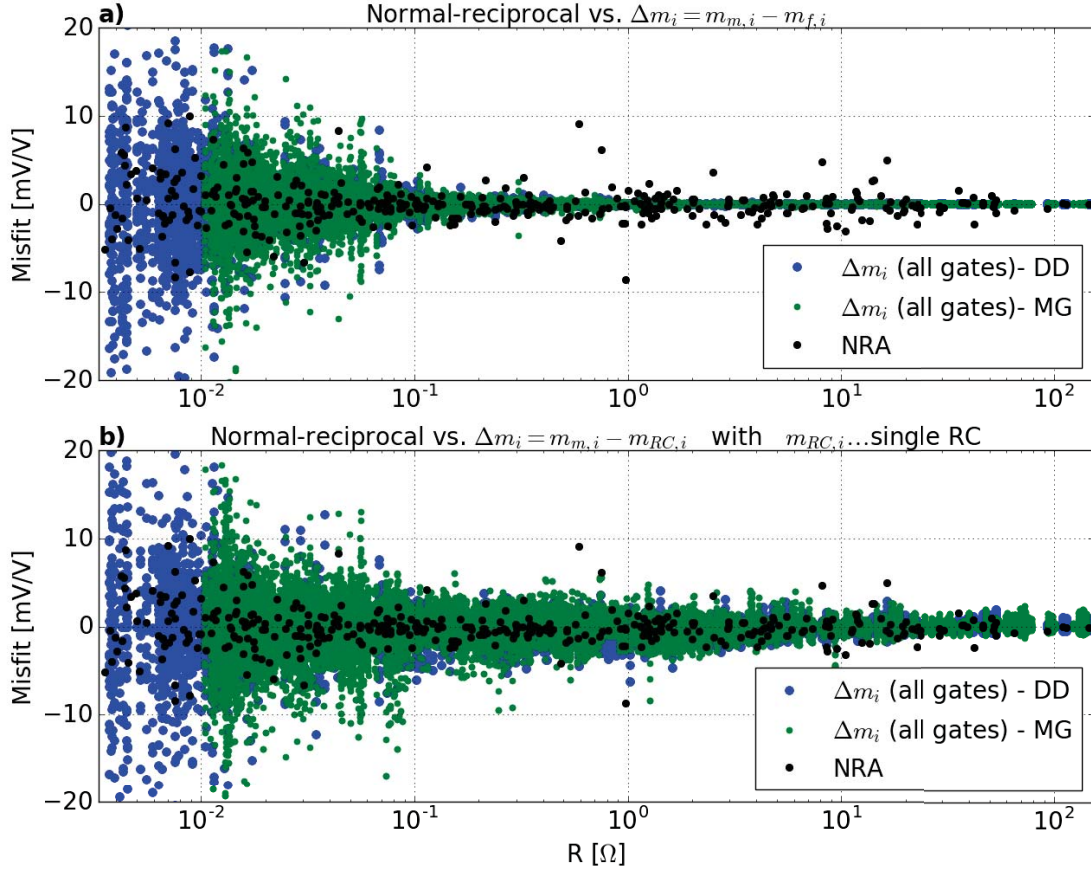


Figure 6.6: Distributions of Δm_i (for all gates) for MG and DD data collected on the same profile (i.e. with identical electrodes) for the case of a comparison with the FDC (upper panel) and single RC (bottom panel). The distributions as well as the magnitude of Δm_i are consistent for the MG and DD data set and thus the error can also be modelled on the basis of the combined distribution.

6.3 Determination of error parameters and the application in an inversion scheme

The final missing step is the adjustment of the error model and the application of the computed error parameters in an appropriate inversion scheme (e.g. CRTomo by Kemna, 2000). In its current form, the code only allows the application of error parameters for phase measurements based on an inverse power law model, as proposed by Flores Orozco et al. (2012b). Hence it is necessary that the found relationship between Δm_i and R can be approximated by an inverse power law model, (i) to ensure a fair comparison with the normal-reciprocal estimates and (ii) to evaluate the applicability without modifying the inversion code. Therefore the NRA chargeability misfits and Δm_i (for both the comparison with the FDC and single RC) were computed for the measurements of a DD data set. Outliers were then removed following the normal-reciprocal methodology as outlined by Flores Orozco et al. (2012b). For the bin analysis

6.3 Determination of error parameters and the application in an inversion scheme

the misfit distributions were divided into 10 bins, followed by an adjustment of the power law model $s(m) = aR^b$ (with $b < 0$) to the corresponding standard deviations of the misfits in each bin.

Figure 6.7 a) presents the adjusted error models as well as the corresponding standard deviations for the normal-reciprocal misfit (red circles), Δm_i for the FDC (black squares) and Δm_i for the single RC (blue triangles). The plot reveals that the standard deviations of Δm_i for the single RC cannot be approximated by the power law model (gof=0.5) and the adjusted error model is similar to the one obtained for Δm_i for the FDC, which approximates the corresponding standard deviations well with a gof value of only 0.04. Unexpected is the poor goodness of fit for the adjusted model of the normal-reciprocal estimates with a gof value of 0.43. Furthermore, differences can be observed for the general shape of the models. Whereas the model for Δm_i for the FDC reveals an almost constant error until $10^{-1} \Omega$ and a pronounced increase for $R < 10^{-1} \Omega$, the adjusted model for the normal-reciprocal estimates displays a gradual increase over the range of resistances. Yet, are the differences likely a result of the poor adjustment of model to the normal-reciprocal standard deviations, as a comparison with fitted rational models ($s(m) = cR^{-1} + d$) demonstrates (figure 6.7 b)). For the rational model the standard deviations of the NRA misfits as well as Δm_i are well approximated by the adjusted models (gof<0.14) and the differences between the models are mostly restricted to $R < 10^{-1} \Omega$.

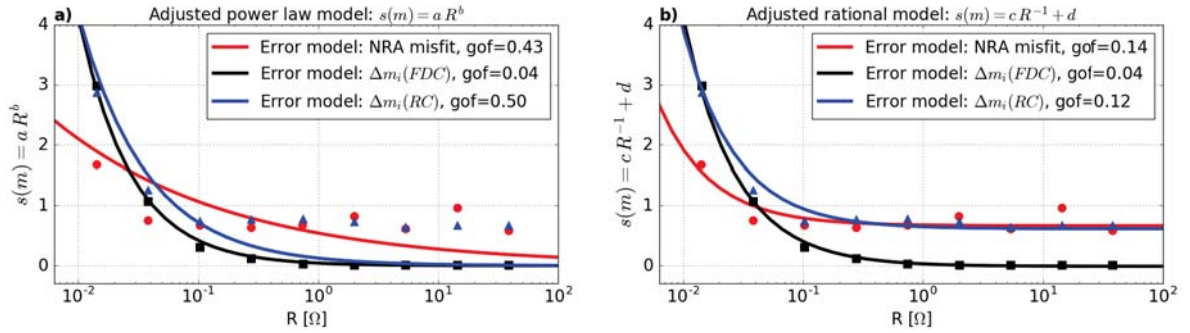


Figure 6.7: Bin standard deviations and adjusted error models for the NRA misfit (red circles), Δm_i for the FDC and Δm_i for the single RC using a) an inverse power law model and b) a rational model.

The influence of the different error models on the resulting images will be discussed for inversions performed on a joint data set, consisting of MG and DD data collected on the same profile. For the inversion with the normal-reciprocal error estimates the DD data set was filtered following the techniques outlined by Flores Orozco et al. (2012b). Outliers in the MG data set were defined by thresholds of the integral chargeability values. The inversions were performed with the chargeability error estimates of the DD data set (as no reciprocal readings for the MG data set were available). Outliers in the data sets used for the inversion with error estimates

for the Δm_i - R relationship were removed based on the analysis of the spatial consistency (i.e. chapter 5). The error model for the chargeability measurements was adjusted to the standard deviations obtained from the bin analysis of the combined distribution of Δm_i for all gates of the DD and MG data set. Considering the negligible differences between the adjusted error models for Δm_i for the FDC and the single RC, as presented in figure 6.7 a), only inversions performed with error estimates based on Δm_i for the FDC will be discussed (denoted as DCA inversions). For the inversion with CRTomo, the integral chargeability values were linearly converted to frequency domain phase values assuming a constant phase response (please refer to Kemna, 2000). Furthermore, for both inversions (NRA and DCA) the error parameters for the resistance measurements (refer to section 2.4) were fixed to the normal-reciprocal resistance estimates.

Figure 6.8 presents a comparison of the imaging results, as obtained for the filtering and error estimates following the NRA a) and DCA b), for the polarization effect expressed in terms of the phase φ of the complex electrical resistivity. Furthermore figure 6.8 c) presents the phase images as obtained for adjusted DCA error estimates, where the DCA error model was shifted to fit the magnitude of the corresponding NRA model ($s(m) = aR^b + c$), as illustrated in figure 6.9. Despite the different error parameterizations all images presented in figure 6.8 solve for the same features and only minor differences can be observed between the NRA (figure 6.8 a)) and DCA image (figure 6.8 b)). The bottom boundaries of the polarizable anomalies located at 20 and 90 m seem to be better resolved for the DCA inversion. No differences can be observed for the image presented in figure 6.8 b) and the image for the adjusted version of the DCA error model presented figure 6.8 c). The adjustment was either too small to influence the inversion behavior or the more important factor is the "shape" of the error model, which is obviously different for the NRA and DCA approach (see figure 6.7). Separate inversions of the MG and DD data sets, after filtering with the spatial consistency approach and a parameterization of the chargeability error based on the Δm_i - R relationship, consistently solved for phase images revealing the same anomalies (figure 6.10). This again demonstrates the applicability of the approach for different measurement configurations.

Unlike the normal-reciprocal methodology, which can directly provide error estimates for the resistance based on the misfit of the resistance readings, an analysis of the decay curve is limited to direct error estimates for the chargeability readings only. Thus further investigations aimed at an evaluation of Δm_i as a proxy for the random error in the resistance measurements. As presented in figure 6.11, for a given DD data set the comparison of the distributions of Δm_i plotted against R (figure 6.11 a)) and the normal-reciprocal resistance misfit ΔR plotted against $1/R$ (figure 6.11 b)) shows similar patterns. The magnitudes of the misfit values (Δm_i and ΔR) are however completely different. The rational model $s(m) = cR^{-1} + d$, as discussed before, is also suited to fit the bin standard deviations obtained from the bin-analysis of Δm_i . Hence, the

6.3 Determination of error parameters and the application in an inversion scheme

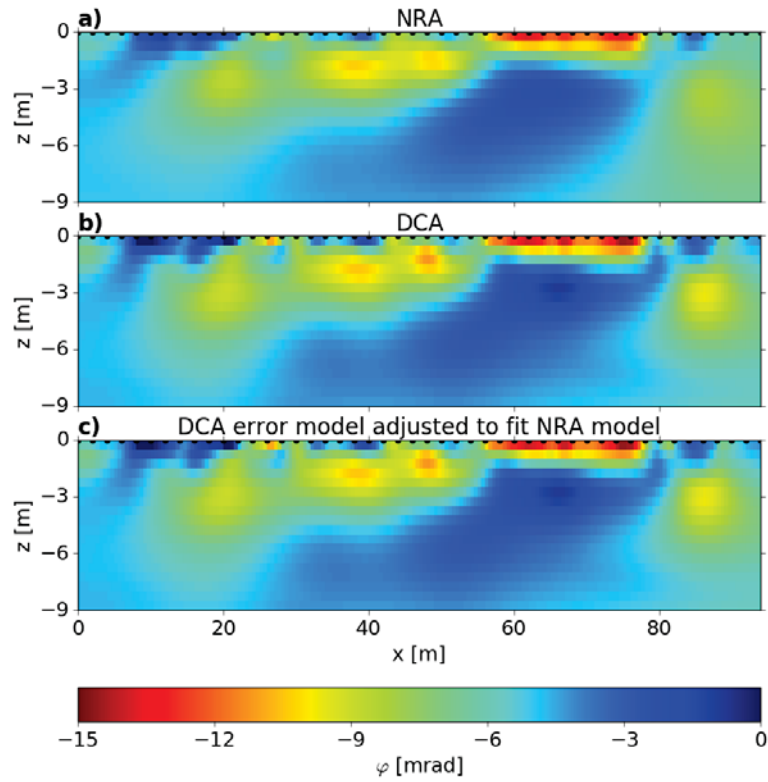


Figure 6.8: Imaging results for the polarization effect expressed in terms of the phase φ of the complex electrical resistivity for filtering and error estimates based on a) the NRA, b) the DCA and c) DCA with the error model adjusted to fit the magnitude of the NRA error model (see figure 6.9).

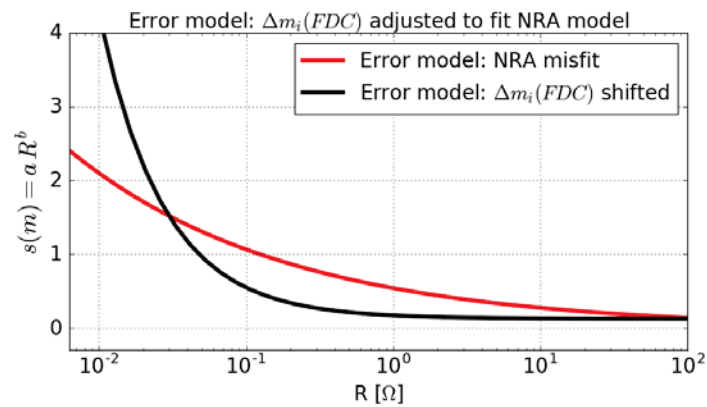


Figure 6.9: Adjusted version of the error model based on Δm_i where the model is shifted to fit the magnitude of the corresponding NRA model, e.g. a constant term is added to the power law model $s(m) = aR^b + c$.

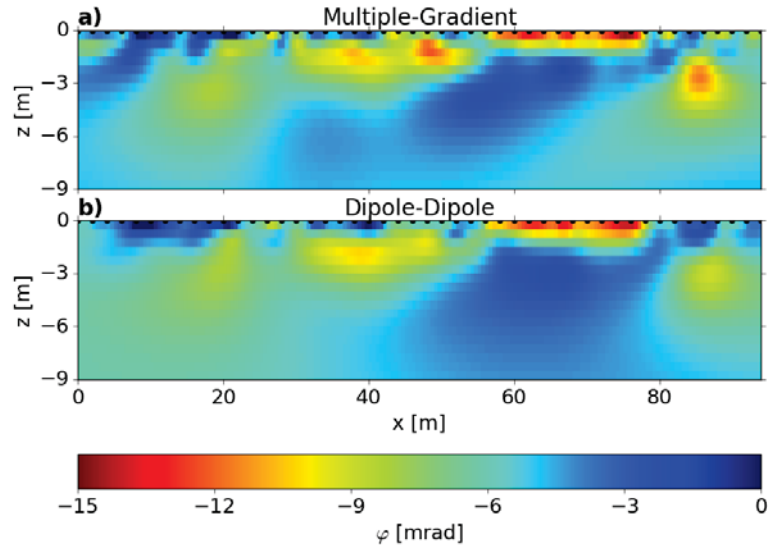


Figure 6.10: Imaging results for the polarization effect expressed in terms of the phase φ of the complex electrical resistivity for filtering and error estimates based on the DCA approach for a) MG and b) DD data set measured on the same profile revealing consistent images.

proposed approach to characterize the random error for the resistance measurements consists of fitting the rational model and the subsequent insertion of the model parameters c and d to the linear model $s(R) = c + Rd$ used by most authors (LaBrecque et al., 1996; Slater et al., 2000; Flores Orozco et al., 2012b). Alternatively, the linear model can directly be fitted to the bin standard deviations as obtained from the bin analysis of Δm_i plotted against $1/R$ providing consistent error parameters. Figure 6.11 c) presents the adjusted models for the NRA resistance misfit ΔR and the approach based on Δm_i revealing the possibility to solve for similar error parameters. Differences can be observed for $R > 10^1 \Omega$ where the DCA error model shows a stronger increase. Nevertheless inversions computed with both parameterizations of the resistance error consistently solved for the same resistivity images with a slightly higher contrast for the DCA resistivity image, as presented in figure 6.12. The inversions were performed for the same joint data sets of MG and DD data as mentioned before.

6.3 Determination of error parameters and the application in an inversion scheme

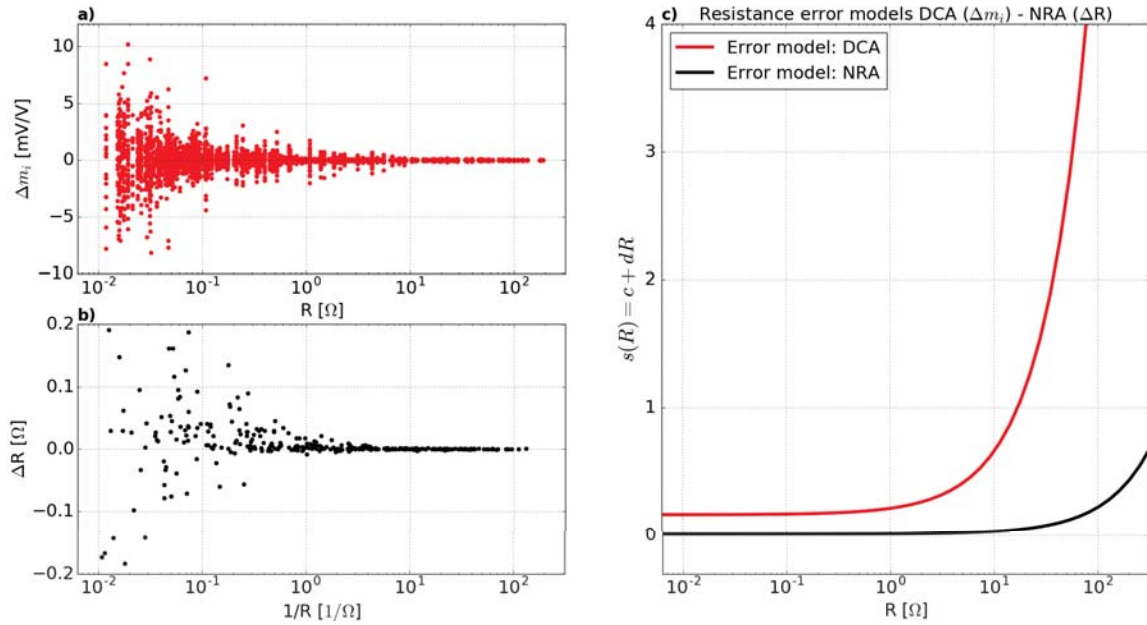


Figure 6.11: Distributions of a) Δm_i plotted against R and b) ΔR against $1/R$ reveal similar patterns. b) adjusted resistance error models for the DCA approach (based on Δm_i ; red line) and the NRA approach (based on ΔR ; black line).

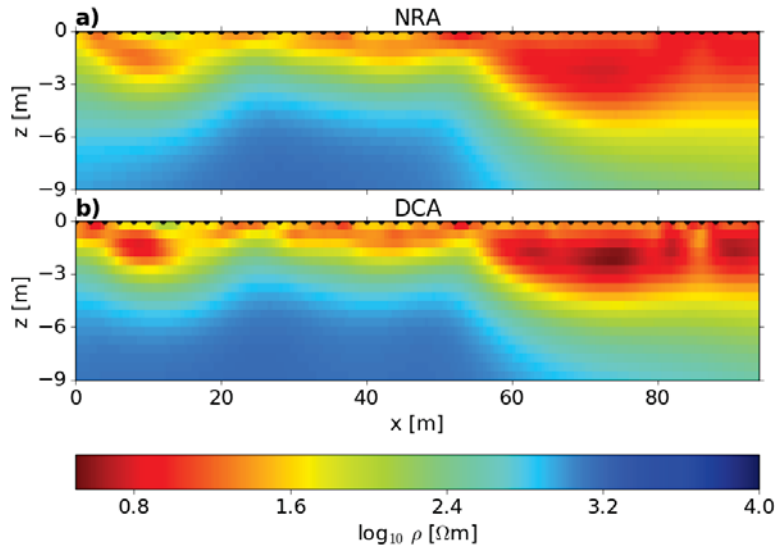


Figure 6.12: Resistivity images as obtained for inversions performed with resistance error parameterizations based on a) the NRA approach (ΔR) and b) the DCA approach (Δm_i) reveal the same features. For the DCA images the contrast is slightly higher.

Chapter 7

Decay Curve Analysis*

The so-called "Decay Curve Analysis" (DCA), as the main outcome of this thesis, comprises a novel data processing methodology for TDIP data based on the analysis of the voltage decay curve. Consisting of a four-step methodology it permits to remove outliers and furthermore is suited to quantify the random error in the resistance and chargeability measurements without the need of reciprocal readings. The upcoming sections will provide a step-by-step description of the proposed DCA and references to the corresponding detailed discussions within this thesis. In order to evaluate the accuracy of the proposed approach, filter and imaging results obtained from the DCA are in a final step compared with results from the well-established NRA.

7.1 Power law fit and first filter

In a first step the modified power law model (equation 3.1c), as discussed in section 3.2, is fitted to each measured decay curve of the data set and the goodness of fit is assessed by computing the RMSD (equation 3.4) between the MDC and FDC. Non-decaying curves are then being removed based on the model parameters of the FDC ($a < 0$ and $b < 0$ or $a > 0$ and $b > 0$). Figure 7.1 presents the pseudosection of MG integral chargeability data before (top panel) and after the removal of non-decaying curves (center panel). Furthermore the bottom panel of figure 7.1 presents the pseudosection of the associated logarithmic RMSD/goodness of fit values. As noticed earlier (section 5.4.6.1) are "deep" measurements typically related to a large RMSD, i.e. erratic decay curves. However, following the premise to preserve as many measurements as possible, chargeability readings associated to high RMSD values were not removed.

*This chapter is based on the submitted manuscript to Journal of Applied Geophysics: Adrián Flores Orozco, **Jakob Gallistl**, Matthias Bucker, Kenneth H. Williams, 'Decay-curve analysis for data-error quantification in time-domain induced polarization imaging'

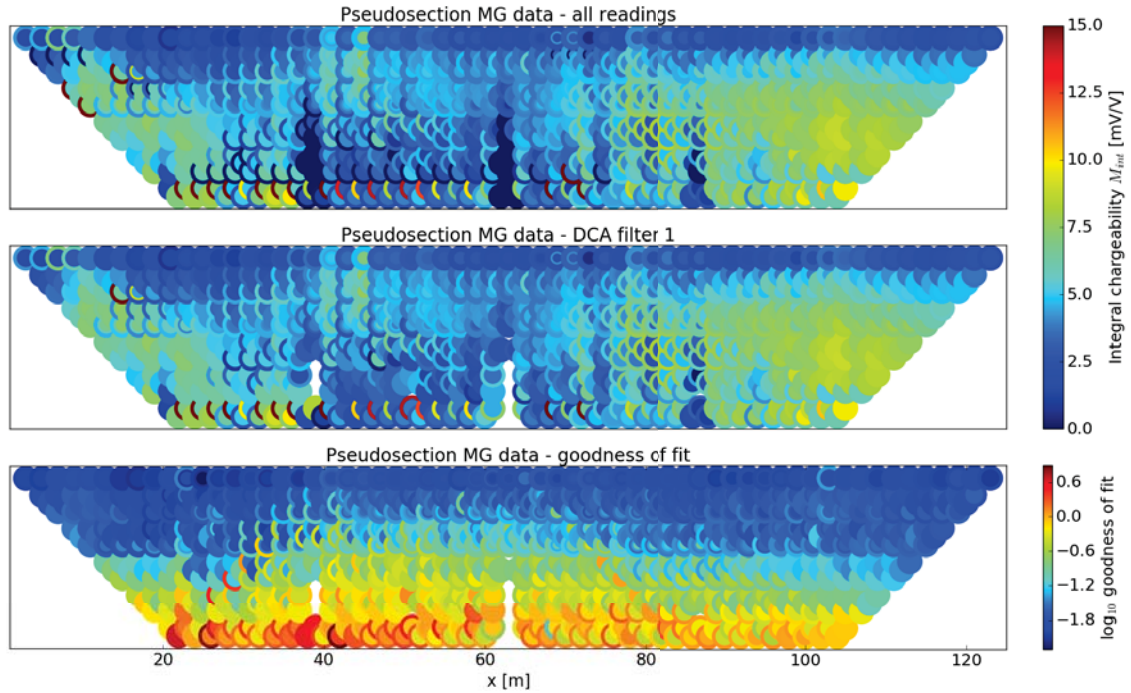


Figure 7.1: Pseudosections of the integral chargeability values for a MG data set for the unfiltered data set (top) and after the removal of measurements related to non-decaying curves (center). The bottom panel presents the pseudosection of the associated goodness of fit values.

7.2 Computation of the reference curve and second filter

As can be observed in figure 7.1, outliers for example related to anomalously high integral chargeability values still prevail after the first filter. Thus, in a second step of the DCA an analysis of the spatial consistency based on the reference curve approach is performed (see section 5.3). The data set after the first filter is therefore partitioned after the current dipole partitioning approach (section 5.2) and for each subset the reference curve is computed following the formulation in equation 5.1e. Based on the deviation in magnitude k , provided by the comparison with the reference curve, outliers are then identified using the methodology described in section 5.5.3. k is therefore separated into the corresponding values k_u , k_d and the associated standard deviations used as the threshold for filtering are then automatically refined based on the individual characteristics of the data set. Possible remaining outliers in the data set, which could not be identified by the reference curve approach, are then assessed by a histogram analysis of the integral chargeability values. Figure 7.2 presents the pseudosection of the MG data set after the removal of outliers following the second filter step.

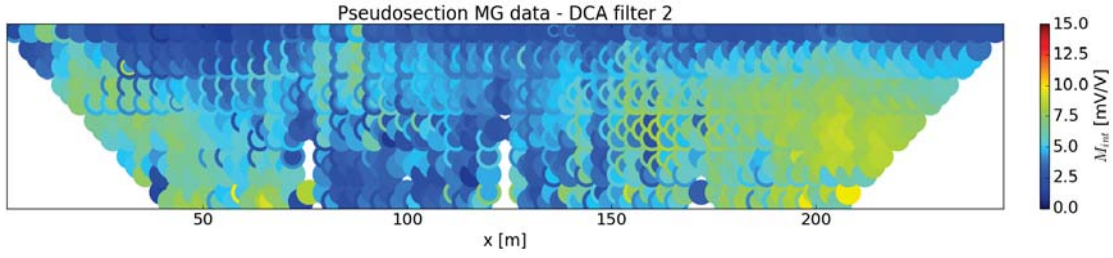


Figure 7.2: Pseudosection of the integral chargeability values of the MG data set after the removal of outliers following the second filter step. Outliers were identified based on an analysis of the spatial consistency.

7.3 Standard deviation estimate and bin analysis

The misfit of the partial chargeability values Δm_i between the MDC and FDC allows to quantify the temporal instability (i.e. erratic behavior) of the measured voltage decay and thus can be used for an estimation of the standard deviation of the chargeability measurement (refer to chapter 6). As discussed in section 6.3 and presented in figure 6.5 is the general dependence on the resistance consistent for Δm_i and the normal-reciprocal chargeability misfit and thus Δm_i can be modelled using the power law relationship (equation 2.9) proposed by Flores Orozco et al. (2012b). The values of Δm_i are therefore partitioned into 10 bins in respect to the resistance and the error model is fitted to the standard deviation of Δm_i in each bin.

7.4 Error model for resistance measurements

Δm_i has also shown to be suited as a proxy to describe the random error in the resistance measurements (section 6.3). The proposed approach consists of adjusting a rational model ($s(m) = cR^{-1} + d$) to the bin standard deviations from the step before and a subsequent insertion of the model parameters c and d into the linear model (equation 2.8) used by most authors (LaBrecque et al., 1996; Slater et al., 2000; Flores Orozco et al., 2012b) to describe the error of the resistance measurements. As presented in figure 6.11 c), following this strategy it is possible to solve for error parameters similar to the ones obtained from the normal-reciprocal approach.

7.5 Results

Figure 7.3 presents the pseudosection of DD integral chargeability data after the removal of outliers following the steps 1 and 2 of the DCA (top panel) and following the NRA (bottom panel). For the latter, outliers were defined as measurements with a normal-reciprocal misfit larger than 2 times the standard deviation of all normal-reciprocal misfits of the data set (Flores Orozco et al., 2012b). Figure 7.3 reveals pseudosections similar for both approaches and only minor

differences can be observed. The DCA however removes fewer measurements associated with high integral chargeability values and/or small separations between electrodes. This illustrates the main difference between the two approaches.

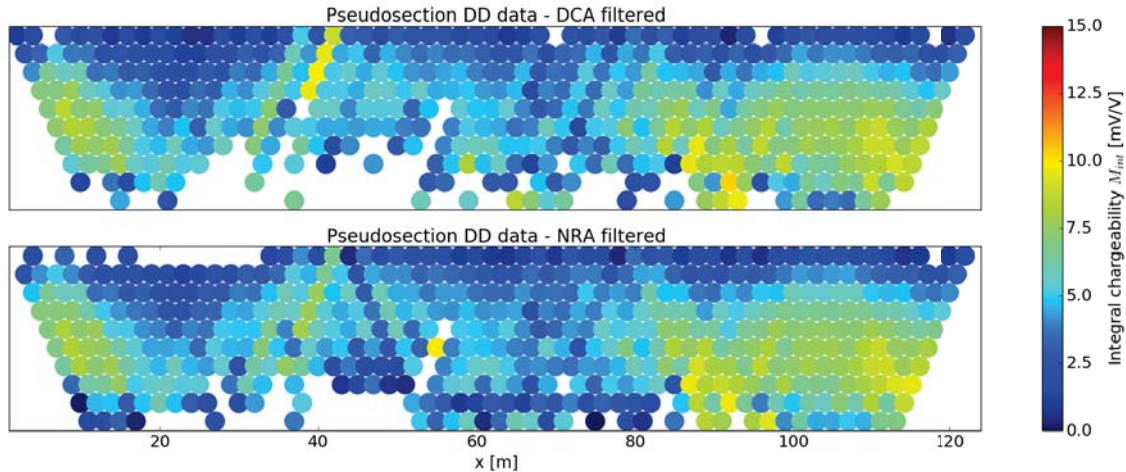


Figure 7.3: Pseudosections of DD integral chargeability data after the removal of outliers following the DCA (top) and NRA (bottom).

Regarding the differences in the electrical images, figure 7.4 presents the imaging results as obtained for the DCA (left column) and NRA (right column) expressed in terms of the resistivity/magnitude ρ (bottom panels) and phase φ (top panels) of the complex electrical resistivity. The inversions were performed for a joint data set of DD and MG measurements with the individual error parameterizations for the chargeability and resistance measurements of both approaches. For the inversion with CRTomo (Kemna, 2000) the integral chargeability values were linearly converted to frequency domain phase values assuming a constant phase response (Kemna, 2000). Plots of the inverted resistivity (bottom panels of figure 7.4) reveal consistent results for both approaches and demonstrate the applicability of Δm_i as a proxy for the quantification of the resistance error. The phase images presented in the top panels of figure 7.4 consistently solve the main geological units; the low phase values correspond to the unsaturated clay-rich top layer and the low permeable Mancos Shale at the bottom, whereas the intermediate to high phase values are associated with the sandy-gravel aquifer material (c.f. section 2.5). The imaging results presented in figure 7.4 clearly show that the DCA permits the inversion of quantitatively similar results as those obtained by the NRA. Furthermore, inversion results after the DCA exhibit a better contrast at depth, clearly indicating the contact between the aquifer materials and the Mancos formation (at ~ 6 m depth). Such contact is poorly solved in the phase image computed after the NRA.

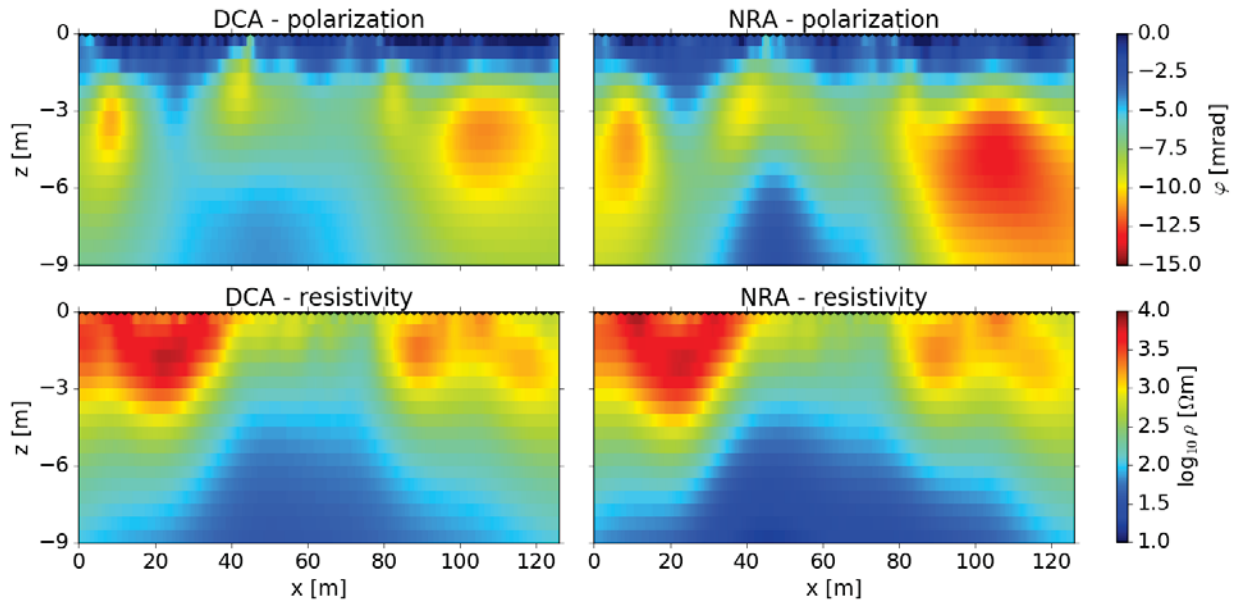


Figure 7.4: Imaging results as obtained for the DCA (left column) and NRA (right column) expressed in terms of the resistivity/magnitude ρ (bottom panels) and phase φ (top panels) of the complex electrical resistivity. The inversions were performed for joint data of DD and MG measurements with the individual error parameterizations for the chargeability and resistance measurements of both approaches.

Chapter 8

Discussion & Conclusion

The proposed DCA is based on the fitting of the measured decay curves by means of a simple power law model ($f(x) = ax^{-b} + c$), which represents the voltage decay after switching the current injection off. Therefore it is critical that the fitted model curves approximate the measured decays as well as possible, in order to prevent biasing of the estimates for the random error and possible distortions during the computation of the reference curves. From all evaluated model functions, the above stated power law model was found to be the best-suited, in terms of the computed goodness of fit as well as the robustness regarding starting values and convergence. In addition, numerical tests revealed only a weak dependence on the sampling of the voltage decay for the fitted model curves, further demonstrating its applicability. The fitting of models of the Cole-Cole family, which are dispersion models describing the frequency-dependence of the IP response (Pelton et al., 1978) revealed similar results when incorporated into the reference curve approach and used for the definition of outliers. However for erratic curves (e.g. noisy data sets), the goodness of fit strongly depends on adequate starting values defined for the fitting, thus compromising the application in an automatic processing scheme. Generally, contributed to the constrained character of the Cole-Cole models with bounded parameters, the computed goodness of fit values were found to be an order of magnitude larger than the one's for the proposed power law model, hence indicating a better approximation for the power law model. Considering these limitations, which will effect i) the estimates for the random error and ii) confine the use in an automatic processing scheme, it was concluded that the power law model is better suited. The advantages regarding the robustness and weak dependency on the starting values outweigh the possible lack of a theoretical justification.

The reference curve approach implemented in the DCA and used as a tool for the analysis of the spatial consistency represents a novel methodology for the identification of outliers in TDIP data. Based on the comparison of the measured decay curves with reference curves it is important that the number of subsets (and therefore the number of reference curves) and the decay curves within the subsets are selected with care. Different partitioning approaches were investigated and the definition of subsets based on the common current dipole seems to be

robust and clusters measurements of comparable signal strength. Also the electrical responses of these subsets stem from a limited volume of influence and thus are likely to be related to similar electrical properties. However in its current form the partitioning approach and thus analysis of the spatial consistency with the reference curve approach has two minor limitations. For electrode configurations like the Wenner configuration, where every potential measurement refers to a different injection dipole, the current concept to cluster the measurements is not applicable and other partitioning approaches are required (e.g. based on the integral chargeability values). Furthermore, for data sets where the first filter step of the DCA removes too many measurements associated to the common current dipole, it might happen that the computed reference curves are only a weak representation of the subset or worse that they might even be defined based on outliers. For such cases the computed deviation parameters are not representative and outliers might stay unidentified.

Yet, this limitation can be resolved by the application of a histogram analysis on the integral chargeability values. By this means possible remaining outliers, which were not assessed by the analysis of the spatial consistency, can be identified and removed. However in order to work properly the number of bins n_b for the histogram needs to be selected in such a way that no over- or underestimation of gaps (related to over- and underfiltering of the data set) occurs. The definition of n_b as a function of the number of measurements n in a data set ($n_b = 1 + 4.5 \cdot \log(n)$) proved to be robust in that regard and permits to identify outliers which fulfill the key premise of the methodology - being well-separated from valid measurements of the main distribution. Applied to integral chargeability values the histogram analysis is however not thought to be the ultimate stand-alone tool rather than an add on to another filter, considering that spatially inconsistent outliers with magnitudes in the range of valid measurements cannot be identified as they are not fulfilling the premise of the approach. In the course of this Master's thesis it was found that the best practice is to perform an analysis of the spatial consistency and the corresponding filtering first and then apply the histogram analysis as an additional refinement.

The quantification of random error for the chargeability and resistance measurements based on the misfit between the measured and the fitted decay curve in each gate (Δm_i) represents a novelty in the processing of TDIP data. The observed patterns for Δm_i as a function of the resistance R are in agreement with those observed for the chargeability misfits obtained from the normal-reciprocal approach revealing differences only for misfit values associated to larger resistances, where Δm_i is an order of magnitude smaller than the corresponding normal-reciprocal misfit. It was therefore concluded that the error can be modelled in consistent manner to the normal-reciprocal approach, using the power law relationship and techniques proposed by Flores Orozco et al. (2012b). It was further found that the combined use of Δm_i for all gates provides more robust estimates of the standard deviations during the bin analysis and

eliminates the arbitrary choice of one particular gate for Δm_i . Furthermore, analysis of Δm_i for DD and MG data sets revealed consistency in both the patterns and magnitudes of the values. For the quantification of random error in the resistance measurements it was assumed that Δm_i can be used as a proxy value and although the adjusted error models based on the DCA and NRA approach are slightly different the computed resistivity images reveal consistent results. The same applies for the computed phase images where the parameterization on Δm_i further provides images with enhanced contrast at depth.

This Master's thesis describes a novel methodology - the decay curve analysis (DCA) - for the processing of TDIP data solely based on an analysis of the measured decay curve. The obtained results demonstrate that the proposed approach is suited to identify outliers and permits to adequately quantify the random error of both the chargeability and resistance measurements. The performance was evaluated based on a comparison with the well-established normal-reciprocal analysis (NRA) and revealed consistent results in terms of the removal of outliers, the quantification of random error and the computed electrical images. Furthermore, DCA processed images exhibit an enhanced contrast at depth, permitting to solve for the contact between the aquifer and the Mancos formation. In contrast to the NRA, the DCA does not require the collection of reciprocal measurements, which i) reduces the acquisition times by 50% and improves the efficiency of field surveys and ii) permits the use of different electrode configurations apart from the DD configuration. Considering these findings, the DCA represents a general improvement of the quality of TDIP imaging.

Bibliography

- Binley, Andrew, Abelardo Ramirez and William Daily (1995). 'Regularised image reconstruction of noisy electrical resistance tomography data'. In: *Process Tomography—1995, Proceedings of the 4th Workshop of the European Concerted Action on Process Tomography, Bergen*, pp. 6–8.
- Binley, Andrew, Lee D. Slater, Melanie Fukes and Giorgio Cassiani (2005). 'Relationship between spectral induced polarization and hydraulic properties of saturated and unsaturated sandstone'. In: *Water Resources Research* 41.12.
- Chelidze, T. L., Y. Gueguen and C. Ruffet (1999). 'Electrical spectroscopy of porous rocks: a review—II. Experimental results and interpretation'. In: *Geophysical Journal International* 137.1, pp. 16–34.
- Cole, Kenneth S. and Robert H. Cole (1942). 'Dispersion and absorption in dielectrics II. Direct current characteristics'. In: *The Journal of Chemical Physics* 10.2, pp. 98–105.
- Dafflon, B., Y. Wu, S. S. Hubbard, J. T. Birkholzer, T. M. Daley, J. D. Pugh, J. E. Peterson and R. C. Trautz (2012). 'Monitoring CO₂ intrusion and associated geochemical transformations in a shallow groundwater system using complex electrical methods'. In: *Environmental science and technology* 47.1, pp. 314–321.
- Dahlin, Torleif and Bing Zhou (2006). 'Multiple-gradient array measurements for multichannel 2D resistivity imaging'. In: *Near Surface Geophysics* 4.2, pp. 113–123.
- Doetsch, Joseph, Gianluca Fiandaca, Esben Auken, Anders Vest Christiansen, Aaron Graham Cahill and Rasmus Jakobsen (2015a). 'Field-scale time-domain spectral induced polarization monitoring of geochemical changes induced by injected CO₂ in a shallow aquifer'. In: *Geophysics* 80.2, WA113–WA126.
- Doetsch, Joseph, Thomas Ingeman-Nielsen, Anders Vest Christiansen, Gianluca Fiandaca, Esben Auken and Bo Elberling (2015b). 'Direct current (DC) resistivity and induced polarization (IP) monitoring of active layer dynamics at high temporal resolution'. In: *Cold Regions Science and Technology* 119, pp. 16–28.
- Du, Pan, Warren A. Kibbe and Simon M. Lin (2006). 'Improved peak detection in mass spectrum by incorporating continuous wavelet transform-based pattern matching'. In: *Bioinformatics* 22.17, pp. 2059–2065.
- Flores Orozco, Adrián, Andreas Kemna, Christoph Oberdörster, Ludwig Zschornack, Carsten Leven, Peter Dietrich and Holger Weiss (2012a). 'Delineation of subsurface hydrocarbon

Bibliography

- contamination at a former hydrogenation plant using spectral induced polarization imaging’. In: *Journal of contaminant hydrology* 136, pp. 131–144.
- Flores Orozco, Adrián, Andreas Kemna and Egon Zimmermann (2012b). ‘Data error quantification in spectral induced polarization imaging’. In: *Geophysics* 77.3, E227–E237.
- Flores Orozco, Adrián, Milica Velimirovic, Tiziana Tosco, Andreas Kemna, Hans Sapon, Norbert Klaas, Rajandrea Sethi and Leen Bastiaens (2015). ‘Monitoring the injection of microscale zerovalent iron particles for groundwater remediation by means of complex electrical conductivity imaging’. In: *Environmental science & technology* 49.9, pp. 5593–5600.
- Flores Orozco, Adrián, Kenneth H. Williams and Andreas Kemna (2013). ‘Time-lapse spectral induced polarization imaging of stimulated uranium bioremediation’. In: *Near Surface Geophysics* 11.5, pp. 531–544.
- Flores Orozco, Adrián, Kenneth H. Williams, Philip E. Long, Susan S. Hubbard and Andreas Kemna (2011). ‘Using complex resistivity imaging to infer biogeochemical processes associated with bioremediation of an uranium-contaminated aquifer’. In: *Journal of Geophysical Research: Biogeosciences* 116.G3, n/a.
- Gazoty, Aurélie, Gianluca Fiandaca, J. Pedersen, Esben Auken and Anders Vest Christiansen (2012a). ‘Mapping of landfills using time-domain spectral induced polarization data: the Eskelund case study’. In: *Near Surface Geophysics* 10.6, pp. 575–586.
- Gazoty, Aurélie, Gianluca Fiandaca, J. Pedersen, Esben Auken, Anders Vest Christiansen and J. K. Pedersen (2012b). ‘Application of time domain induced polarization to the mapping of lithotypes in a landfill site’. In: *Hydrology and Earth System Sciences* 16.6, pp. 1793–1804.
- Ghorbani, Ahmad, Christian Camerlynck, Nicolas Florsch, Philippe Cosenza and André Revil (2007). ‘Bayesian inference of the Cole–Cole parameters from time-and frequency-domain induced polarization’. In: *Geophysical prospecting* 55.4, pp. 589–605.
- Gill, Philip E. and Walter Murray (1978). ‘Algorithms for the solution of the nonlinear least-squares problem’. In: *SIAM Journal on Numerical Analysis* 15.5, pp. 977–992.
- Guptasarma, D. (1982). ‘Computation of the time-domain response of a polarizable ground’. In: *Geophysics* 47.11, pp. 1574–1576.
- Jones, Eric, Travis Oliphant, Pearu Peterson et al. (2001–). *SciPy: Open source scientific tools for Python*. [Online; accessed <today>]. URL: <http://www.scipy.org/>.
- Kemna, A., A. Binley, G. Cassiani, E. Niederleithinger, A. Revil, L. Slater, K. H. Williams, A. Flores Orozco, F. H. Haegel, A. Hördt, S. Kruschwitz, V. Leroux, K. Titov and E. Zimmermann (2012). ‘An overview of the spectral induced polarization method for near-surface applications’. In: *Near Surface Geophysics*.
- Kemna, Andreas (2000). ‘Tomographic inversion of complex resistivity - Theory and application’. PhD thesis. Ruhr University of Bochum.

- Koch, K., A. Kemna, J. Irving and K. Holliger (2011). ‘Impact of changes in grain size and pore space on the hydraulic conductivity and spectral induced polarization response of sand’. In: *Hydrology and Earth System Sciences* 15.6, pp. 1785–1794.
- Koestel, Johannes, Andreas Kemna, Mathieu Javaux, Andrew Binley and Harry Vereecken (2008). ‘Quantitative imaging of solute transport in an unsaturated and undisturbed soil monolith with 3-D ERT and TDR’. In: *Water Resources Research* 44.12.
- Krautblatter, Michael, Sarah Verleysdonk, Adrián Flores-Orozco and Andreas Kemna (2010). ‘Temperature-calibrated imaging of seasonal changes in permafrost rock walls by quantitative electrical resistivity tomography (Zugspitze, German/Austrian Alps)’. In: *Journal of Geophysical Research: Earth Surface* 115.F2.
- LaBrecque, Douglas J., Michela Miletto, William Daily, Aberlardo Ramirez and Earle Owen (1996). ‘The effects of noise on Occam’s inversion of resistivity tomography data’. In: *Geophysics* 61.2, pp. 538–548.
- LaBrecque, Douglas and William Daily (2008). ‘Assessment of measurement errors for galvanic-resistivity electrodes of different composition’. In: *Geophysics* 73.2, F55–F64.
- Marescot, Laurent, Régis Monnet and Dominique Chapellier (2008). ‘Resistivity and induced polarization surveys for slope instability studies in the Swiss Alps’. In: *Engineering Geology* 98.1–2, pp. 1–28.
- Moré, Jorge J. (1978). ‘The Levenberg-Marquardt algorithm: implementation and theory’. In: *Numerical analysis*. Springer, pp. 105–116.
- Nelder, John A. and Roger Mead (1965). ‘A simplex method for function minimization’. In: *The computer journal* 7.4, pp. 308–313.
- Newville, Matthew, Till Stensitzki, Daniel B. Allen and Antonino Ingargiola (2014). *LMFIT: Non-Linear Least-Square Minimization and Curve-Fitting for Python*. DOI: 10.5281/zenodo.11813. URL: <https://doi.org/10.5281/zenodo.11813>.
- Nordsiek, S. and A. Weller (2008). ‘A new approach to fitting induced-polarization spectra’. In: *Geophysics* 73, F235–F245.
- Okay, G., P. Cosenza, A. Ghorbani, C. Camerlynck, J. Cabrera, N. Florsch and A. Revil (2013). ‘Localization and characterization of cracks in clay-rocks using frequency and time-domain induced polarization’. In: *Geophysical Prospecting* 61.1, pp. 134–152.
- Pelton, W. H., S. H. Ward, P. G. Hallof, W. R. Sill and P. H. Nelson (1978). ‘Mineral discrimination and removal of inductive coupling with multifrequency IP’. In: *Geophysics* 43.3, pp. 588–609.
- Ramirez, Abelardo, William Daily, Andrew Binley and Douglas LaBrecque (1999). ‘Electrical impedance tomography of known targets’. In: *Journal of Environmental and Engineering Geophysics* 4.1, pp. 11–26.
- Revil, A., N. Florsch and C. Camerlynck (2014). ‘Spectral induced polarization porosimetry’. In: *Geophysical Journal International* 198.2, pp. 1016–1033.

Bibliography

- Shao, Zhenlu, André Revil, Deqiang Mao and Deming Wang (2017). ‘Induced polarization signature of coal seam fires’. In: *Geophysical Journal International* 208.3, p. 1313.
- Slater, Lee and Andrew Binley (2006). ‘Synthetic and field-based electrical imaging of a zerovalent iron barrier: Implications for monitoring long-term barrier performance’. In: *Geophysics* 71.5, B129–B137.
- Slater, Lee, Andrew Binley, William Daily and Richard Johnson (2000). ‘Cross-hole electrical imaging of a controlled saline tracer injection’. In: *Journal of applied geophysics* 44.2, pp. 85–102.
- Slater, Lee, Dimitrios Ntarlagiannis, Yves R. Personna and Susan Hubbard (2007). ‘Pore-scale spectral induced polarization signatures associated with FeS biomineral transformations’. In: *Geophysical Research Letters* 34.21.
- Sogade, John A., Francesca Scira-Scappuzzo, Yervant Vichabian, Weiqun Shi, William Rodi, David P. Lesmes and Frank Dale Morgan (2006). ‘Induced-polarization detection and mapping of contaminant plumes’. In: *Geophysics* 71.3, B75–B84.
- Sumner, J. S. (1976). *Principles of induced polarization for geophysical prospecting*, NY.
- Telford, William Murray, Lloyd P. Geldart and Robert E. Sheriff (1990). *Applied geophysics*. Vol. 1. Cambridge university press.
- Tikhonov, A. N. and V. Y. Arsenin (1977). *Solutions of ill-posed problems*. Vol. 14. Winston Washington, DC.
- Ustra, Andréa Teixeira, Vagner Roberto Elis, Giulliana Mondelli, Lázaro Valentin Zuquette and Heraldo Luiz Giacheti (2012). ‘Case study: a 3D resistivity and induced polarization imaging from downstream a waste disposal site in Brazil’. In: *Environmental Earth Sciences* 66.3, pp. 763–772.
- Wainwright, Haruko M., Adrián Flores Orozco, Matthias Bucker, Baptiste Dafflon, Jinsong Chen, Susan S. Hubbard and Kenneth H. Williams (2015). ‘Hierarchical Bayesian method for mapping biogeochemical hot spots using induced polarization imaging’. In: *Water Resources Research*.
- Ward, Stanley H. (1990). ‘Resistivity and induced polarization methods’. In: *Geotechnical and environmental geophysics* 1, pp. 147–189.
- Yang, Xianjin, Xiao Chen, Charles R. Carrigan and Abelardo L. Ramirez (2014). ‘Uncertainty quantification of CO₂ saturation estimated from electrical resistance tomography data at the Cranfield site’. In: *International Journal of Greenhouse Gas Control* 27, pp. 59–68.